Democratic and Popular Republic of Algeria
Ministry of Higher Education and Scientific Research
University Mohamed Khider of Biskra

Faculty of Exact Sciences and Science of Nature and Life
Department of Matter Sciences

Ref: ……...

Thesis Presented to obtain the degree of

Doctorate in chemistry

Option: materials chemistry

Entitled:

Synthesis and physicochemical properties of oxides based on lanthanum and transitions metals

Presented by:
Mr. HADJI Fawzi

Publicly defended on: 05/12/ 2023

In front of the Jury committee composed of:

Mr. Barkat Djamel	Professor	University of Biskra	President
Mr. Omari Mahmoud	Professor	University of Biskra	Supervisor
Mr. Mebarki Mourad	Research director	CRTSE	Co-Supervisor
Mr. Meghezzi Ahmed	Professor	University of Biskra	Examiner
Mr. Gabouze Noureddine	Research director	CRTSE	Examiner

Acknowledgements

First and foremost, I thank ALLAH, almighty, for giving me the strength, courage, and ability to move forward and successfully accomplish this study as intended.

The work presented in this thesis was conducted at the Laboratory of Molecular Chemistry and Environment (LCME) at the University of Biskra in collaboration with the Research Center in Semiconductor Technology for Energetic (CRTSE), under the supervision of **Mr. Omari Mahmoud** and co-supervision of Mr. **Mebarki Mourad**.

It is said that the smooth progress of a thesis is closely linked to the supervisors, and I must say that I have been extremely fortunate in this regard. First and foremost, I would like to thank my thesis supervisors, Mr. **Omari Mahmoud** and Mr. **Mebarki Mourad**, for giving me the opportunity to work on this subject and for accompanying me throughout these years. I am grateful for their moral support, the extensive research discussions, their kindness, and not to mention their unwavering optimism... in short, for all the help and support they have provided me during these years! *You are doing an amazing job*.

I would also like to extend my sincere appreciation to Mr. **Boukherroub Rabah** for graciously accommodating me in his laboratory during my internship at Lille University, France.

I would like to express my deepest gratitude to Professor **Barkat Djamel** for agreeing to preside over my jury.

I would like to warmly thank Mr. **Gabouze Noureddine**, a research director at CRTSE and Mr. **Meghezzi Ahmed**, a professor at the university of Biskra, for their keen interest in my work and for accepting to be part of the thesis defense committee for my doctoral dissertation.

I would also like to thank my gratitude to my doctoral colleagues as well as Lab engineers: Boudfar Fatima, Ben Makhlouf Aymen, Lallali Hayet and Darkaoui Khaled.

I would like to thank myself for my hard work, dedication, and perseverance. I appreciate the effort I have put into achieving my goals and overcoming challenges along the way. I acknowledge the self-discipline and motivation that have driven me to reach this point. I also would like to thank myself for believing in my abilities and never giving up. I am proud of the progress I have made and excited for the future accomplishments that lie ahead.

Lastly, I would like to express my gratitude to the members of my family, especially my parents, who have always supported me in pursuing my studies and completing my doctoral journey. So, "thank you all" for your unwavering encouragement and belief in me.

Dedications

I dedicate this modest work;

To my dear parents, no words can express my respect, eternal love, and gratitude for your sacrifices for my education and well-being. I thank you for all the support and love you have shown me since my childhood, and I hope always to have your blessings by my side.

To my dear brothers Ahlem, Saleh Eddine, and Yahia.

To my close friends; Maar Salah and Belguidoum Abderrahime.

To my colleagues,

Thank you for encouraging and supporting me in completing this thesis.

To all those who love me and eagerly await my success. I hope to always live up to your expectations and hopes.

Abstract

Developing economical and highly efficient electrode material is crucial for water electrolysis and supercapacitors associated with energy conversion and storage. For this purpose, we successfully elaborated a new series of $LaCo_{1-x}Zn_xO_3$ oxides (x = 0, 0.03, 0.05, 0.1, 0.2, 0.3 and 0.4) via a facile sol-gel route. We investigated, for the first time, their structural, morphological and electrochemical properties for possible use as electrode material toward oxygen evolution reaction and supercapacitor in a basic solution. Among the developed materials, the $LaCo_{0.9}Zn_{0.1}O_3$ electrocatalyst displays a remarkable performance; an overpotential of merely 327 mV is needed to generate a specified current density of 10 $mA.cm^{-2}_{geo}$; a current density of around 73.41 $mA.cm^{-2}$ at 450 mV, almost twice as high compared to the pristine electrocatalyst; a faster reaction kinetic with a lower Tafel slope of ~92 $mV.dec^{-1}$ and an activity loss of less than 4 % after 24 hours of utilization. On the other hand, the $LaCo_{0.95}Zn_{0.05}O_3$ electrode provides the best specific capacitance (300.47 F/g); this is almost four times higher compared to the undoped electrode (75.36 F/g). The electrode material also shows excellent capacitance retention of 85.73% after 5000 cycles at 5 A/g. In addition, a hybrid supercapacitor with high energy density was constructed by combining $LaCo_{0.95}Zn_{0.05}O_3$ with activated carbon. The $LaCo_{0.95}Zn_{0.05}O_3$//activated carbon hybrid device offers a high energy density of 36.12 $Wh.kg^{-1}$ at a power density of 390.35 $W.kg^{-1}$. The device is characterized by outstanding retention of the capacitance of 81% after being subjected to 5000 successive charge-discharge cycles.

Résumé

Le développement de matériaux d'électrode économiques et hautement efficaces est crucial pour l'électrolyse de l'eau et les supercondensateurs associés à la conversion et au stockage de l'énergie. Dans ce but, nous avons réussi à élaborer une nouvelle série d'oxydes $LaCo_{1-x}Zn_xO_3$ (x = 0, 0.03, 0.05, 0.1, 0.2, 0.3 et 0.4) par une méthode sol-gel facile. Nous avons étudié, pour la première fois, leurs propriétés structurales, morphologiques et électrochimiques en vue d'une utilisation possible en tant que matériau d'électrode pour la réaction d'évolution de l'oxygène et les supercondensateurs dans une solution basique. Parmi les matériaux développés, l'électrocatalyseur $LaCo_{0.9}Zn_{0.1}O_3$ présente des performances remarquables : une sur-potentiel de seulement 327 mV est nécessaire pour générer une densité de courant spécifiée de 10 $mA.cm^{-2}_{geo}$; une densité de courant d'environ 73,41 $mA.cm^{-2}$ à 450 mV, soit presque deux fois plus élevée que celle de l'électrocatalyseur non modifié ; une cinétique de réaction plus rapide avec une pente de Tafel inférieure à ~92 $mV.dec^{-1}$ et une perte d'activité de moins de 4 % après 24 heures d'utilisation. D'autre part, l'électrode $LaCo_{0.95}Zn_{0.05}O_3$ offre la meilleure capacité spécifique (300,47 F/g) ; c'est presque quatre fois plus élevé que celui de l'électrode non dopée (75,36 F/g). Le matériau d'électrode présente également une excellente rétention de la capacitance de 85,73 % après 5000 cycles à 5 A/g. De plus, un supercondensateur hybride à haute densité d'énergie a été construit en combinant $LaCo_{0.95}Zn_{0.05}O_3$ avec du charbon activé. Le dispositif hybride $LaCo_{0.95}Zn_{0.05}O_3$//charbon activé offre une densité d'énergie élevée de 36,12 $Wh.kg^{-1}$ à une densité de puissance de 390,35 $W.kg^{-1}$. Le dispositif se caractérise par une rétention exceptionnelle de la capacitance de 81 % après avoir été soumis à 5000 cycles de charge-décharge successifs.

ملخص

تطوير مواد الكترود اقتصادية وعالية الكفاءة ضروري لتحليل الماء والمكثف الفائق المرتبطة بتحويل الطاقة وتخزينها. لهذا الغرض، تم وبنجاح عن طريق طريقة سهلة سول-جل توليف سلسلة جديدة من أكاسيد بيروفسكايت اللانثانوم الكوبالتيت المخدر بتراكيز مختلفة من الزنك حيث ($LaCo_{1-x}Zn_xO_3$ .x= 0, 0.03, 0.05, 0.1, 0.2, 0.3 et 0.4)

قمنا بدراسة الخصائص الهيكلية والمورفولوجية والكهروكيميائية لأغراض استخدامها المحتملة كمواد كهربائية لتفاعل تطور الأكسجين والمكثف الفائق في محلول قاعدي. من بين المواد المطورة، يظهر المحفز أداءً ملحوظًا؛ يتطلب فقط 327 ملي فولت جهد زائد لتوليد كثافة تيار محددة تبلغ 10 ملي أمبير/ سم²؛ كثافة تيار تبلغ حوالي 73.41 ملي أمبير/سم² عند 450 ملي فولت، تقريبًا ضعف الكثافة مقارنة بالمحفز الأصلي؛ وحركة تفاعلية أسرع مع ميل تافل أقل بقيمة حوالي 92 ملي فولت/عقد وفقدان نشاط أقل من 4٪ بعد 24 ساعة من الاستخدام. من ناحية أخرى، يوفر الكترود (300.47 فراد/غ) أفضل سعة محددة (300.47 فراد/غ)؛ وهذا يعادل تقريبًا أربع مرات الكترود الاصلي (75.36 فراد/غ). يظهر مادة الكترود الكهربائية أيضًا احتفاظا ممتازًا للسعة بنسبة 85.73٪ بعد 5000 دورة من الشحن والتفريغ عند 5 أمبير/غ. بالإضافة إلى ذلك، يوفر الجهاز الهجين كثافة طاقة عالية تبلغ 36.12 واط. ساعي/كجم عند كثافة قدرها 390.35 واط/كجم. يتميز الجهاز أيضًا بالاحتفاظ المتميز بالسعة بنسبة 81٪ بعد تعرضه لـ 5000 دورة متتالية من الشحن والتفريغ

Summary

General Introduction

Chapter I: Literature Review

Chapter II: Synthesis and Characterization Techniques

Chapter IV: Synthesis and electrochemical properties of zinc doping lanthanum cobaltite perovskite as an electrode material for hybrid supercapacitors.

General Conclusion

List of figures

List of tables

General Introduction

1. Introduction

1.1. Hypothesis/Problem Statement

The number of people on Earth increased from 6.1 to 7.9 billion between 2000 and 2021 and could reach 10 billion by 2050. This sharp increase combined with the rapid development of emerging countries is expected to lead to an increase in global energy consumption by 2050. Currently, fossil fuels (oil, coal, natural gas) represent more than 80% of total energy production in the world. However, these resources are limited, non-renewable and their exploitation generates significant emissions of gas with the greenhouse effect which contributes to climatic warming. These non-renewable resources will continue to be in demand in the coming years as technology improves to make them more accessible. Despite all this, fossil fuel reserves are becoming scarcer (about 50 years for oil) while global energy demand is expected to be 40% higher than in 2007 by the 2030s, according to the International Energy Agency (IEA).

In this context, the development of "renewable" and "alternative" energies for the production of electricity (which remains the most easily transportable and distributable energy) appears essential for the planet's energy future. Some countries, such as Germany, Canada, Japan, the United States, France and China, have clearly stated their desire to reduce their consumption of nuclear energy and coal by relying more on renewable energy, including solar and wind energies. Technological innovations now make it possible to reduce the production costs of these two sources, which can thus be brought into line with other energy sources (renewable or non-renewable) such as nuclear, hydraulics, geothermal, etc.

Besides production, another equal preponderance is the storage of this energy. Thus, the field of research and development of energy storage devices is undeniably a hot topic. The great challenge for future storage devices will be to provide both high energy and power densities. The energy stored is in thermal form (thermodynamic solar farms), mechanical form and chemical or electrochemical form (**green hydrogen**, **supercapacitors**, etc.).

One of the environmentally friendly energy sources is hydrogen, which can be generated sustainably by utilizing water electrolysis (a resource that is abundant on our planet given that 71% of its surface is covered with it). However, the efficiency of water electrolysis is currently hindered by a significant overpotential of the anode side, which is attributed to the oxygen evolution reaction (OER) **[1]**. The rate of a reaction is linked to the activation energy barrier through a linear free energy relationship, and the presence of a catalyst can lower this barrier **[2]**. The utilization of IrO_2 and RuO_2 in industries aims to decrease the overpotential on the anode. Nevertheless, their expensive cost and limited availability have hindered the widespread adoption of water electrolyzers **[3]**.

The first question that arises after this brief summary is the following:

How to develop cheap and high-performance catalyst ("low overpotential" and "stable") to hasten the reaction and overcome this stalemate?

The second category of energy storage systems is supercapacitors. They possess a lengthy lifetime (up to several million cycles) and the ability to provide high power output in a very short time. Moreover, they can discharge rapidly (in mere seconds) with an efficiency exceeding 90%. However, their most significant drawback is their low energy density compared with batteries **[4]**. In addition, the performance of supercapacitors is greatly

influenced by the electrode materials employed. Researchers have dedicated extensive efforts to investigate effective electrode materials that demonstrate high specific capacitance and long-term cycling stability **[5]**.

After this brief overview, a critical inquiry arises:

How can the energy density of supercapacitors be raised while maintaining their beneficial features, such as extended lifespan and high power density? Stated differently, which devices can be utilized to merge the benefits of batteries and supercapacitors?

Perovskite oxides (ABO_3, where A denotes the alkaline and/or the rare earth metals and B the transition metal) are viewed as potential materials for OER electrocatalysts and supercapacitor electrodes because of their exceptional electronic structures, outstanding ionic conductivities, excellent thermal stability **[6]**, high catalytic activity and stability **[7]**, in addition to low cost **[8]**. In general, ions located at the A site are catalytically inactive, unlike those at site B, although their properties do affect the stability of the perovskite material. The existence of oxygen vacancies plays an essential role in improving the specific capacitance of electrode materials and enhancing the OER catalytic activity **[9, 10]**. An effective strategy to improve the oxygen vacancies is either to dope the A and/or B sites which produces a change in the transition metal oxidation states, or to generate oxygen vacancies to compensate for the charge **[11]**. $LaCoO_3$ has been known as an active and durable OER electrocatalyst **[12]** and efficient material for supercapacitor electrodes because of multiple oxidation states of cobalt atoms (Co^{2+}, Co^{3+}, and Co^{4+}), which supply excellent electrochemical redox properties **[13, 14]**. The impact of substituting cations A and B on the physicochemical properties (optical, electrical, electronic, magnetic, catalytic, etc.) of perovskite materials has been widely

researched in literature. Their electrochemical properties, particularly in OER and supercapacitors, continue to be relevant due to the significance of these catalysts in the industrial sector **[15]**.

1.2. Objectives and Scope

The aim of this thesis is to investigate the performance of perovskite-type materials, particularly Co-based transition metal oxides, as both OER electrocatalysts and supercapacitor electrodes in alkaline electrolytes. Initially, our goal is to investigate how the structure of $LaCoO_3$ perovskite materials is affected by the introduction of zinc doping. Additionally, we aim to assess the effect of zinc doping on the OER activity of these materials. Finally, we intend to study how zinc doping influences the specific capacitance and the energy density of these materials.

1.3. Dissertation Overview

The thesis is divided into four chapters:

- The first chapter is devoted to a bibliographical overview covering, on the one hand, the background of mixed oxides of perovskite-type and, on the other hand, the electrochemical properties, in particular for the application to energy conversion in the form of water splitting and energy storage in the form of supercapacitors.
- The second chapter is dedicated to the description of the synthesis methods of the studied materials as well as the characterization techniques used, with a theoretical presentation and then a description of the conditions utilized during the analysis.
- The third chapter focused on the structural, morphological, textural and electro-catalytic characterization of $LaCo_{1-x}Zn_xO_3$ samples with high zinc doping concentrations (x= 0, 0.1,

0.2, 0.3 and 0.4) synthesized using the sol-gel method. The characterizations were conducted by thermal analysis (DTA-TG); structural analysis by X-ray diffraction (XRD), Fourier transform infrared spectroscopy (FT-IR) and X-ray photoelectron spectroscopy (XPS); morphological and textural analysis by means of scanning electron microscopy (SEM), laser particle size and N_2 physisorption. Lastly, we will report the electrochemical analysis of the catalysts toward the OER using different techniques such as linear sweep voltammetry (LSV), anodic Tafel polarization, electrochemical impedance spectroscopy (EIS), and electrochemical stability by using chronopotentiometry (CP).

- The fourth chapter is devoted to the structural, morphological, textural and electrochemical characterization of $LaCo_{1-x}Zn_xO_3$ samples with low contents of Zn doping (x= 0, 0.03, 0.05 and 0.1) synthesized using the sol-gel method. The characterizations were carried out by means of XRD, FT-IR, XPS, SEM and N_2 adsorption desorption isotherms. The electrochemical investigations of the synthesized material as an electrode material for hybrid supercapacitors will be studied using different techniques such as cyclic voltammetry (CV), galvanostatic charge-discharge (GCD) and EIS.

Finally, as a general conclusion, we have reviewed the results obtained during this study and have also proposed perspectives for an effective and efficient continuation of the work begun in this thesis.

References

[1] Z.W. Seh, J. Kibsgaard, C.F. Dickens, I. Chorkendorff, J.K. Norskov, T.F. Jaramillo, Combining theory and experiment in electrocatalysis: Insights into materials design, Science 355 (2017).

[2] W. T. Hong, M. Risch, K. A. Stoerzinger, A. Grimaud, J. Suntivich, Y. Shao-Horn, Toward the Rational Design of Non-Precious Transition Metal Oxides for Oxygen Electrocatalysis. Energy Environ. Sci. 2015, 8 (5), 1404–1427.

[3] Y. Lee, J. Suntivich, K.J. May, E.E. Perry, Y. Shao-Horn, Synthesis and Activities of Rutile IrO_2 and RuO_2 Nanoparticles for Oxygen Evolution in Acid and Alkaline Solutions, J. Phys. Chem. Lett. 3 (2012) 399-404.

[4] H. Ren, L. Zhang, J. Zhang, T. Miao, R. Yuan, W. Chen, Z. Wang, J. Yang, B. Zhao, Na^+ pre-intercalated $Na_{0.11}MnO_2$ on three-dimensional graphene as cathode for aqueous zinc ion hybrid supercapacitor with high energy density, Carbon 198 (2022) 46-56.

[5] J. Wu, Y. Guo, W. Raza, H. Gul, G. Luo, Y. Ding, Y. Li, Y. Lv, J. Yu, L.N.U. Rehman, Fast assembling MnO_2-network electrode materials to achieve high performance asymmetric aqueous supercapacitors, J Alloys Compd. 931 (2023) 167568.

[6] H. Mo, H. Nan, X. Lang, S. Liu, L. Qiao, X. Hu, H. Tian, Influence of calcium doping on performance of $LaMnO_3$ supercapacitors, Ceram Int. 44 (2018) 9733-9741.

[7] R.-h. Yuan, Y. He, W. He, M. Ni, M.K.H. Leung, Bifunctional electrocatalytic activity of $La_{0.8}Sr_{0.2}MnO_3$-based perovskite with the A-site deficiency for oxygen reduction and evolution reactions in alkaline media, Appl. Energy. 251 (2019) 113406.

[8] K. Zhu, H. Liu, X. Li, Q. Li, J. Wang, X. Zhu, W. Yang, Oxygen evolution reaction over

Fe site of $BaZr_xFe_{1-x}O_{3-\delta}$ perovskite oxides, Electrochim. Acta 241 (2017) 433-439.

[9] E. Omari, M. Omari, Cu-doped GdFeO3 perovskites as electrocatalysts for the oxygen evolution reaction in alkaline media, Int. J. Hydrog. Energy 44 (2019) 28769-28779.

[10] M. Rafique, S. Hajra, M.Z. Iqbal, G. Nabi, S.S.A. Gillani, M. Bilal Tahir, Fabrication of novel perovskite oxide $Ba_xMn_{1-x}O_3$ electrode for supercapacitors, International Journal of Energy Research 45 (2021) 4145-4154.

[11] G. Guo, K. Ouyang, J. Yu, Y. Liu, S. Feng, M. Wei, Facile synthesis of $LaCoO_3$ with a high oxygen vacancy concentration by the plasma etching technique for high-performance oxygen ion intercalation pseudocapacitors, ACS Applied Energy Materials 3 (2019) 300-308.

[12] W.T. Hong, M. Risch, K.A. Stoerzinger, A. Grimaud, J. Suntivich, Y. Shao-Horn, Toward the rational design of non-precious transition metal oxides for oxygen electrocatalysis, Energy Environ. Sci. 8 (2015) 1404-1427.

[13] Y. Cao, J. Liang, X. Li, L. Yue, Q. Liu, S. Lu, A.M. Asiri, J. Hu, Y. Luo, X. Sun, Recent advances of perovskite oxides as electrode materials for supercapacitor, Chem Commun 57 (2021) 2343-2355.

[14] B. Zhang, C. Yu, Z. Li, Enhancing the Electrochemical Properties of $LaCoO_3$ by Sr-Doping, rGO-Compounding with Rational Design for Energy Storage Device, Nanoscale Research Letters 15 (2020) 1-13.

[15] E. Omari, Doctoral thesis, University of Mohamed Khider Biskra (2021).

Chapter I:

Literature Review

Literature review

I.1. Generalities on mixed oxides

Mixed oxides are homogeneous solid phases comprising several types of metal cations of different oxidation states. These metal cations bond with oxide ions (O^{-2}) to create crystallographic structures with defined characteristics. They are classified into three families, **Perovskites (ABX_3)**, Spinels (AB_2O_4), Pyrochlores ($A_2B_2O_7$). The preparation methods, chemical composition, and nature of the cations are essential factors to consider. The physical properties of mixed oxides, including crystallographic structure, morphology, and specific surface area, are influenced by the cations present, leading to notable changes in the materials' electrochemical behavior.

I.2. Perovskite structure

Around 1830, Gustave Rose, a geologist, first described perovskite, a precious mineral composed of calcium titanate ($CaTiO_3$) with a simple cubic structure. The name "perovskite" is derived from *Lev Aleksevich von Perovski*, a Russian mineralogist. Nowadays, the term perovskite refers to a group of compounds that share the same atomic arrangement ABX_3. Here, A denotes the alkaline and/or the rare earth metals, B the transition metal and X the anion, which may include an oxide, fluoride, and, in some cases, chloride, bromide, iodide, sulfide, or hydride). The interest in the perovskite oxides for many years has resulted from the ease of changing the nature of the A and B cations present in the structure. Changes in these elements lead to a change in the intrinsic properties of the material, leaving the door open to all sorts of physical properties depending on the chemical and electronic nature of the A and B atoms **[1]**.

I.2.1 The crystal structure

The perovskite structure, which is akin to the $CatiO_3$ type structure, is the most commonly found crystal structure among compounds with the formula ABO_3. The ideal perovskite structure is cubic in shape, possessing a space group of Pm3m, and can be visualized as a series of uniform octahedra with oxygen ions situated at the apex. The center of these octahedra contains the B cations, while the A cations occupy the centers of cuboctahedral cavities (refer to Fig. I. 1). One reason why perovskite oxides can have structures different from the ideal cubic structure is the presence of cations with varying ionic radii, ionic charges, and electronegativity at the A and B sites.

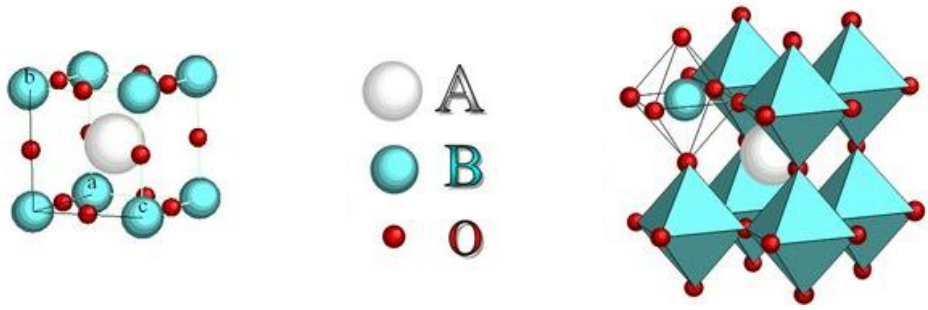

Fig. I. 1. Schematic representation of a lattice of the ideal perovskite structure.

I.2.2. Valence of A and B cations

The ABO_3 structure maintains a neutral overall charge. To achieve this, the sum of the valence of cations A and B must equal (+6), in order to compensate for the three oxygen atoms (-6). The valence state of cations A and B may differ among perovskites, resulting in various configurations such as $A^{1+}B^{5+}O_3^{2-}$, $A^{2+}B^{4+}O_3^{2-}$, and $A^{3+}B^{3+}O_3^{2-}$. It is worth noting that this representation of 6 electrons located on the oxygen atoms and 6 holes on the cations is very simplistic, in fact, the charges are rather distributed throughout the entire structure and redistributed in the system.

I.2.3. Stability of the structure

To intuitively determine the existence and stability of a structure for a variety of ionic radii, steric factors come into play. For example, the size of the B element must be large enough to create octahedra with the oxygen and define the structure. The size of the A element then becomes an important factor as its distortions within the oxygen framework may result in a change in the structure's space group. Since the bonds between the oxygen and the atoms A and B are iono-covalent, V.M. Goldschmidt formulated a stability condition, the so-called tolerance factor t, which enables the radii of the cations A and B and of the anion O to be related by the following relation **[2]**:

$$t = \frac{r(A). \quad r(O)}{\sqrt{2}(r(B) - r(O))} \qquad \textbf{(I.1)}$$

Where r(A), r(B) and r(O) are the radii of the A, B and O ions respectively.

The ideal cubic perovskite structure is difficult to achieve since the conditions are very demanding. Specifically, the radius of site A must be similar to that of oxygen, which is approximately **1.40 Å**. Additionally, the ionic radius of site B must be **(√2-1). r(O)**.

The factor in question reflects the degree of symmetry deviation in the perovskite structure, which arises from the inequality between the lengths of the A-O and B-O bonds. As shown in Table. I. 1, a **t** value of 1 corresponds to a cubic symmetry, whereas slight deviations from 1 can give rise to a rhombohedral distortion R3c, which involves a rotation of the BO_6 octahedra around a specific direction **[3, 4]**. If **t** deviates further from 1 ($0.86 < t < 0.9$), the polyhedron around the A ion becomes deformed, causing the B-O-B angles to decrease below 180°, resulting in the symmetry becoming orthorhombic (Pbnm). If **t** is less than 0.86, the octahedral structure is replaced by pyramidal geometry, and the transition metal cation B

adopts square planar coordination, which leads to the formation of fluorite-like layers. Conversely, a hexagonal structure is obtained for t values greater than 1.

Table. I. 1. Different symmetries adopted by the perovskite structure as a function of the tolerance factor t.

t value	Observed symmetry
t <0.85	Switching from perovskite to fluorite
0.85< t <0.9	orthorhombic
0.9< t <1	rhombohedral
t =1	cubic
1< t <1.06	hexagonal

It's important to note that the stability of the perovskite structure also relies on the iconicity of the bonds, i.e. the structure is as stable as the bonds involved have a strong ionic character **[5]**. This iconicity is proportional to the difference in electronegativity between the cations and anions, which can be determined by calculating the average electronegativity:

$$\ddot{X} = \frac{X_{A-O}+X_{B-O}}{2} \qquad \textbf{(I.2)}$$

where $X_{A\text{-}O}$ and $X_{B\text{-}O}$ are the differences in electronegativity between the cations at sites A and B and the associated oxygen.

Numerous materials with a perovskite structure demonstrate multiple polymorphic modifications. For instance, the $BaTiO_3$ oxide undergoes various transformations as the temperature rises:

Rhombohedral ↔ orthorhombic ↔ tetragonal ↔ cubic.

I.2.4. Defects in the crystals

Any deviation from the periodicity of the lattice or structure in a crystal is considered a defect **[6].** In fact, solids always contain defects. This can be attributed to either the laws of thermodynamics (presence of thermal agitation at temperatures above absolute zero) or the different treatments (quenching, irradiation, etc.) that they undergo to improve their properties (such as electrical conductivity, strength, etc.) **[7]**. The goal is to control the nature and quantity of defects as much as possible. In the context of our thesis, we will focus on point defects as they are the most prevalent types of defects found in oxides. We can identify various defects types in the case of a simple ordered AB crystal, as shown in Fig. I. 2.

Interstitial defect: when an atom of the lattice is located between other atoms in the same lattice, it is referred to as a lattice atom. On the other hand, the presence of a foreign atom among lattice atoms is also known as an interstitial solid solution.

Vacancy defect: a vacancy in a crystal occurs when an atom is missing. If the vacancy is cationic, it results in a negative charge within the crystal.

Substitution defect: when a foreign atom is present in the place of a lattice atom, it is also known as a substitutional solid solution.

Anti-site defect: in the case of an ordered crystal composed of multiple types of atoms with strict chemical alternation, there can be anti-site defects, which occur when atoms are located at lattice nodes but break the chemical regularity.

Electrical charge defect: crystal sites may exhibit a more negative charge (free electron) or a more positive charge (electron hole) than other sites of the same type.

Schottky defect: represents an association of anionic and cationic vacancy in ionic crystals.

Frenkel defect: an atom leaves its normal position and takes an interstitial position. In the case of an ionic crystal, only cations can do this because they are smaller than anions **[8]**.

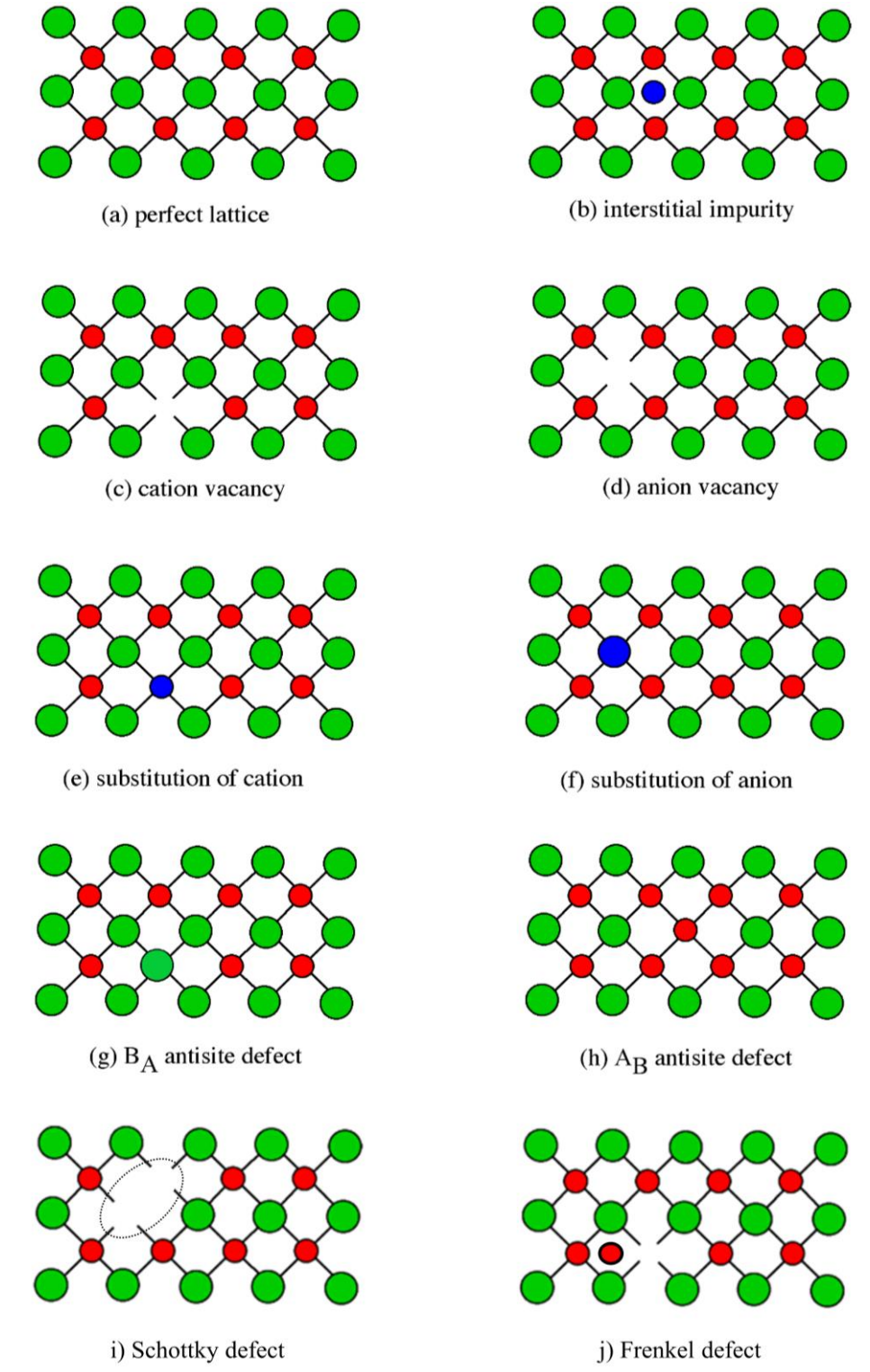

Fig. I. 2. Examples of different types of defects that could occur.

I.2.5. Mechanism of defect diffusion

Vacancy mechanism: this is the most frequent mechanism of diffusion. In fact, vacancy-type point defects are prevalent in many types of solids, including oxides and sulfides. As presented in Fig. I. 3, it involves the movement of a specific atom, located near a vacant site, to occupy that site. As a result, vacancy is transferred to the site that was previously occupied by the migrated atom. This migration process preserves the total vacancies number **[9]**.

Interstitial mechanism: an interstitial atom moves from one interstitial site to another, it is considered a point defect where the successive jumps are uncorrelated. This is known as the direct interstitial mechanism and is common for atoms that are normally found in interstitial solutions. However, if the identified atom can be located in both substitutional and interstitial positions, an indirect interstitial mechanism is also possible **[8, 10]**.

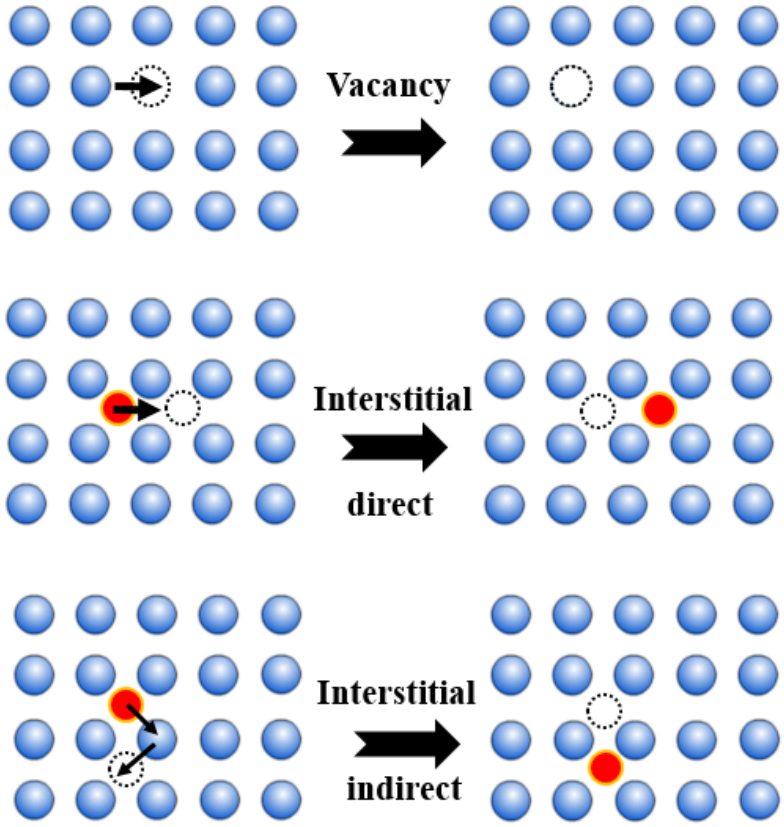

Fig. I. 3. The vacancy and interstitial mechanisms.

I.2.6. Properties of perovskite-type material

Due to their properties, the perovskite materials are of considerable technological importance covering a very broad range of practical applications. Notable is the discovery in the 1940s of the ferroelectric properties of barium titanate ($BaTiO_3$) used in electronics for capacitors and transducers. In the mid-1980s, the first high-temperature superconductor was discovered, lanthanum barium copper oxide and, in 1987 Nobel Prize in physics, was awarded for this discovery.

As of 2012, perovskites have been identified as possible inexpensive base materials for high-efficiency commercial photovoltaics, and perovskites also have optoelectronic properties such as strong light absorption and facilitated charge transport. Some of perovskites' typical properties are ferromagnetism, piezoelectricity, electrical conductivity, superconductivity, ion conductivity, magnetism, catalytic properties, supercapacitor electrode materials, and optical properties **[11]**.

I.3. Applications

The literature provides numerous examples of cationic substitutions made at the A and/or B sites of the perovskite structure, with the idea of improving the initial structural, catalytic and electrochemical properties of the material, both in the general framework of solid-state chemistry than that, more specific, of the search for new materials for **water electrolysis** and **electrochemical supercapacitor applications** which are the objectives of this thesis.

I.3.1. Water electrolysis

I.3.1.1. Brief historical overview

Water electrolysis, the process of using electricity to split water molecules into hydrogen and oxygen gases, has a fascinating historical evolution. The discovery of water electrolysis is often attributed to the work of two scientists, William Nicholson and Anthony Carlisle, in the late 18th century. In 1800, they independently observed that passing an electric current through water resulted in the production of hydrogen and oxygen gases.

Throughout the 19th century, scientists and inventors made significant contributions to the field of electrolysis. Michael Faraday's research on electrolysis laid the foundation for our understanding of the quantitative relationship between the amount of substance liberated during electrolysis and the electric current passed through the electrolyte. Faraday's laws of electrolysis, established in the 1830s, became fundamental principles in electrochemistry.

The industrial applications of water electrolysis began to emerge in the mid-19th century. Electrolysis cells were used to produce various chemicals and metals on a large scale. Notably, the development of the mercury cell, also known as the Castner-Kellner cell, allowed for the production of chlorine and sodium hydroxide through the electrolysis of saltwater. This became a vital industrial process, especially in the production of bleach and other chlorine-related compounds.

In the 21st century, water electrolysis has experienced a resurgence of interest due to the growing focus on renewable energy and the potential of hydrogen as a clean and sustainable fuel source. Electrolysis powered by renewable electricity, known as "green hydrogen," has gained significant attention as a means of storing and utilizing excess

renewable energy. Governments, industries, and researchers worldwide are investing in the development and deployment of advanced electrolysis technologies to support the emerging hydrogen economy.

At last, ongoing research and development aim to further improve the efficiency, affordability, and scalability of electrolysis technologies, paving the way for a future powered by clean and renewable energy sources **[12]**.

I.3.1.2. Fundamental principles

An electrolysis cell consists of two electrodes, namely the anode and cathode, which are connected to a direct current (DC) power supply. These electrodes are separated by an electrolyte, which acts as an ionic conductive medium (Fig. I. 4).

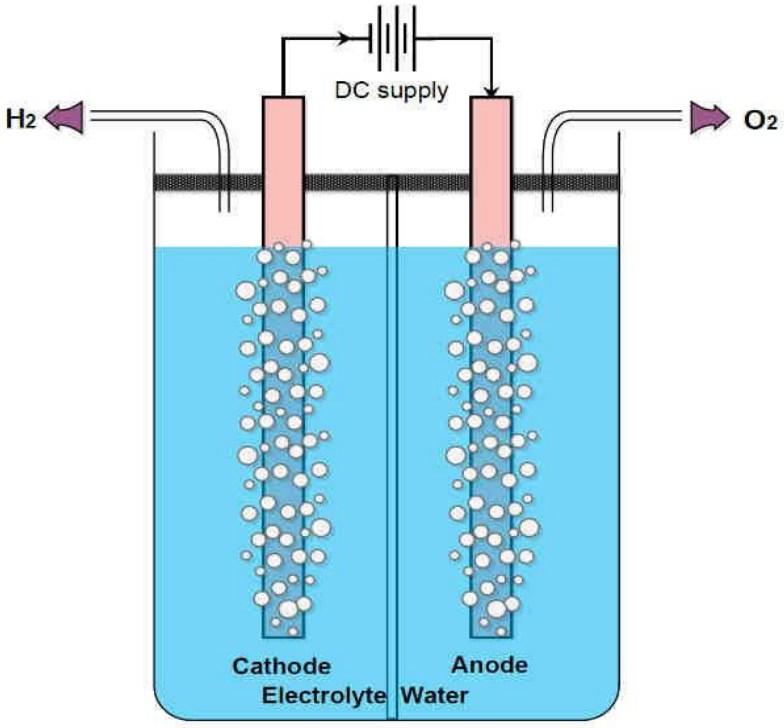

Fig. I. 4. Schematic representation of an electrolyzer cell

Two crucial factors influence the type of electrolysis technology used: temperature and pH. These technologies are categorized based on temperature into three groups: low-temperature processes (below 150 °C), medium-temperature processes (between 200 °C and 600 °C), and high-temperature processes (above 600 °C) **[13]**. We will focus on the one that will be studied in this thesis: low-temperature processes.

I.3.1.3. Low-temperature electrolysis

Low-temperature processes employ two different mediums: acidic medium (with a pH of approximately 0) and alkaline medium (with a pH of approximately 14) **[13]**. we will concentrate on the one that will be studied in this thesis: **alkaline electrolysis**.

I.3.1.3.1. Acidic electrolysis

In the late 1960s, the development and commercialization of this technology began. It utilizes a solid polymer electrolyte membrane that can exchange protons (PEM), with Nafion® being a well-known example. As presented in Fig. I. 5**,** the solid electrolyte is sandwiched between two electrodes, which consist of a catalytic layer. The stack is then immersed in pure water. Noble metals such as platinum on the cathode side and ruthenium and/or iridium oxide on the anode side serve as catalysts for the hydrogen and oxygen evolution reactions, respectively. This technology enables achieving current densities of 1 to 2 $A.cm^{-2}$ with a cell voltage below 1.8 V and has a lifespan exceeding 25,000 hours. However, the use of noble metals makes it costly, and their limited availability hampers large-scale implementation **[13, 14].**

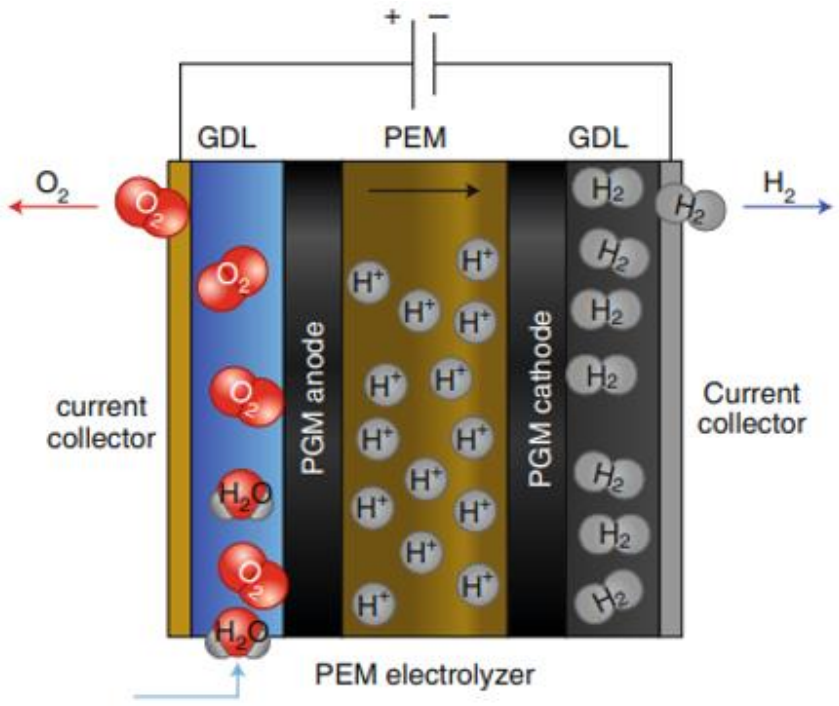

Fig. I. 5. Schematic representation of PEM electrolyzer

I.3.1.3.2. Alkaline electrolysis

Since its discovery in 1789, alkaline electrolysis has evolved into a well-established process extensively utilized by various industries **[15]**. In this process, the electrodes are submerged in an aqueous solution containing potassium hydroxide, and the concentration varies based on temperature (typically ranging from 25% by mass at 80 °C to 40% at 160 °C). A diaphragm is employed to separate the gases generated by the electrolysis (Fig. I. 6). However, since the diaphragm is not entirely impermeable to gases, the resulting gas mixture can create potentially hazardous conditions in terms of flammability as well as explosiveness **[16]**. The current densities achievable in this setup are limited, typically ranging from 0.2 to 0.4 A cm^{-2}, due to the Ohmic drop across the diaphragm and the liquid electrolyte **[17]**.

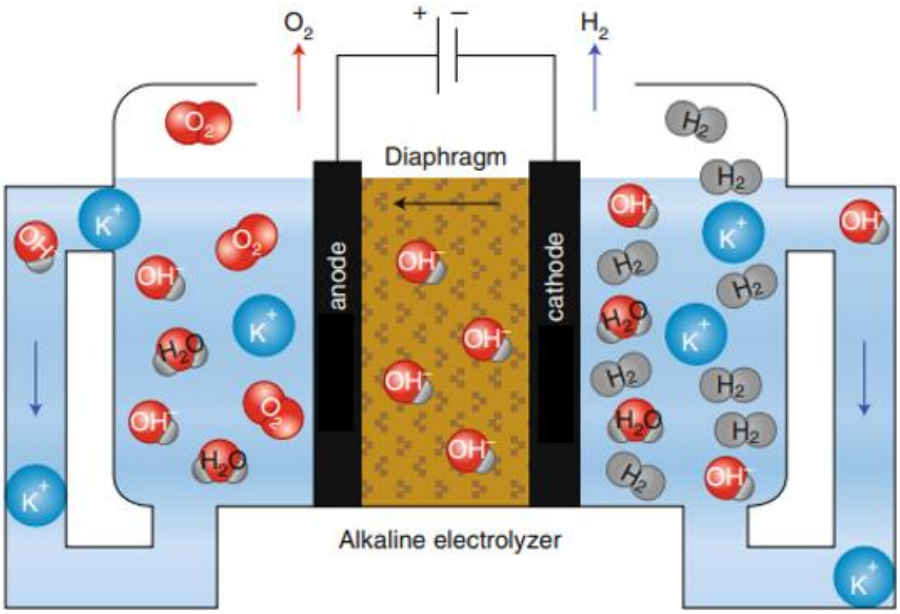

Fig. I. 6. Schematic representation of an alkaline electrolyzer

In recent years, the advancement of anion exchange membranes has led to the development of a novel system known as the anion exchange membrane electrolyzer (AEM) **[13, 18]** (refer to Fig. I. 7). This innovative system opens up the potential to achieve current densities surpassing 1 $A.cm^{-2}$ while maintaining a cell voltage below 2 V, making it a strong contender in performance compared to proton exchange membrane electrolyzers. Moreover, unlike proton exchange membrane (PEM) technology, the alkaline system allows for the utilization of thermodynamically stable transition metal-based catalysts that are well-suited for the operational conditions.

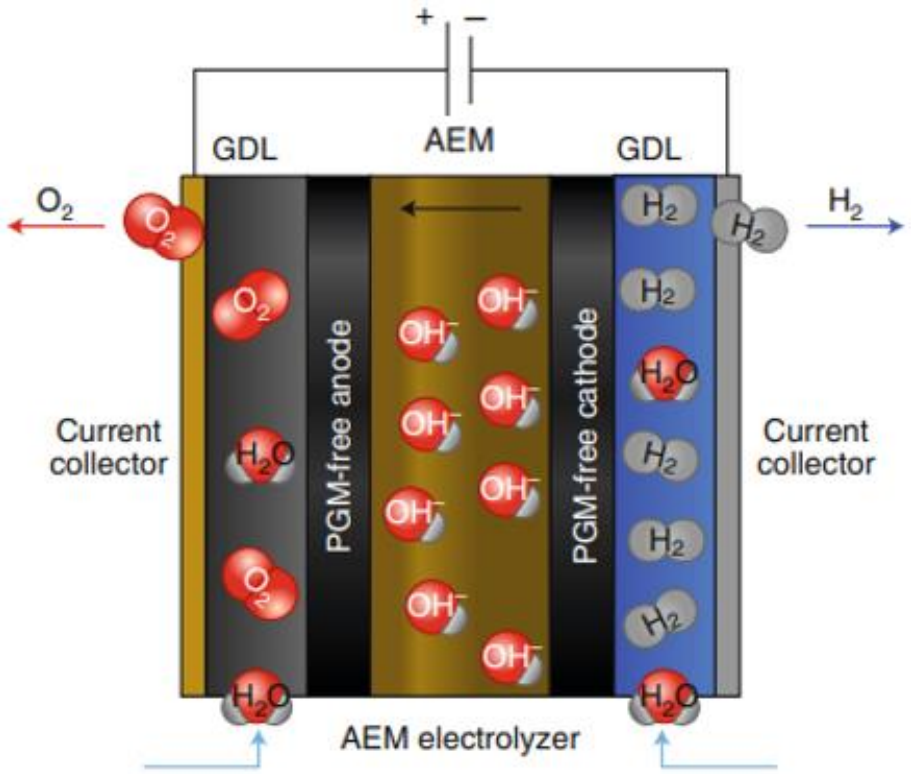

Fig. I. 7. Schematic representation of an AEM electrolyzer.

I.3.1.4. Electrochemical reactions in water electrolysis

During the process of water electrolysis, two reactions occur: the hydrogen evolution reaction (HER) and the oxygen evolution reaction (OER). Electrocatalysis results from the combined effect of electrode potential and catalytic properties of the material, enabling a reduction in the activation energy of electrochemical reactions. The first aim of this thesis is to explore the development of perovskite-based materials for catalyzing the reactions involved in this system. The subsequent section of this literature review will provide a comprehensive analysis of the reaction mechanisms and the underlying factors contributing to the kinetic limitations of the electrochemical reactions. These kinetic limitations are observed as electrode overpotentials, as depicted in Fig. I. 8 and Equation **I.3 [19]**.

$$\eta = E - E_{eq} \quad \text{..... (I.3)}$$

where η (V) is the overpotential, E is the electrode potential (V vs. ERH (reversible hydrogen electrode) and E_{eq} is the equilibrium potential of the O_2/OH- redox couple (1.23V vs. ERH).

The overpotentials are most pronounced for the OER compared to the HER (refer to Fig. I. 8-red curve), which in turn restricts the electrical performance of existing electrolyzers.

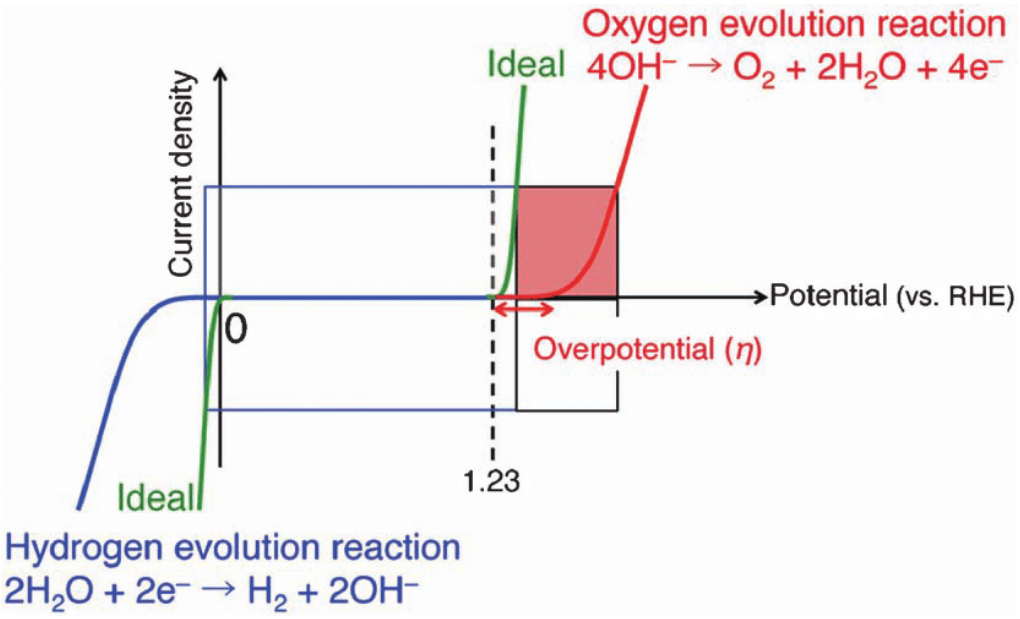

Fig. I. 8. Polarization curves of the hydrogen evolution reaction (in blue) and the oxygen evolution reaction (in red) in an alkaline environment.

This reaction, which involves multiple steps with coupled proton-electron transfers, is highly complex. The utilization of catalysts significantly lowers the activation energy of the reaction. Nevertheless, the overpotentials related to the OER process remain elevated. In the case of an ideal catalyst, the overpotentials would be zero **[20]**, indicating that the material would be capable of activating the OER near the equilibrium potential of the O_2/OH^- couple

(1.23 V vs. RHE). To develop such a catalyst, it is imperative to comprehend the theoretical origin of the observed overpotentials during the oxygen evolution reaction. J.K. Norskov's research team conducted theoretical calculations, postulating the involvement of three oxygen-containing reaction intermediates (-OH, -O, and -OOH) in the OER process (refer to Fig. I. 9), in order to investigate the source of the overpotentials at the surface of catalytic materials **[21, 22]**.

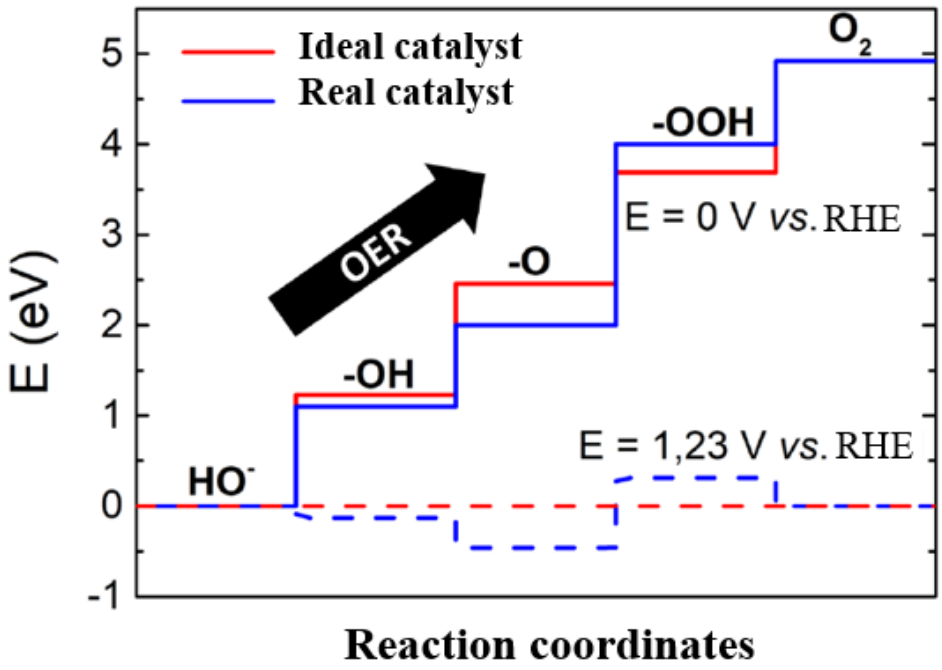

Fig. I. 9. Free energy diagram at zero potential (solid lines) and at 1.23 V vs. RHE (dashed lines) for the "ideal" catalyst (in red) and a real catalyst (in blue).

When the electrode potential is at 0 V vs. RHE, the transition between different intermediates necessitates a 1.23 eV change in free energy in the case of an ideal catalyst (refer to Fig. I. 9-red curve). Hence, a 1.23 eV energy gap is required to shift from one intermediate to another. As a result, applying an electrode potential of 1.23 V vs. RHE enables a spontaneous reaction (characterized by a flat energy profile).

In the case of a real catalyst (refer to Fig. I. 9-blue curve), the energy difference for transitioning between intermediates differs from the ideal value of 1.23 eV. Consequently, to achieve a flat energy profile, it is necessary to apply an electrode potential that deviates from the redox potential value of the O_2/H_2O couple. This disparity is the fundamental reason behind the observed overpotentials during the OER. According to studies conducted by Rossmeisl et al. **[23, 24]**, the energies of bonding between different oxygen-containing intermediates are interconnected and influenced by the adsorption energy of atomic oxygen on the catalyst's surface. These adsorbates are all connected through an oxygen atom bound to the catalyst's surface. Any changes in the bonding energy of one intermediate consequently affect the bonding energies of other reactive intermediates. Calculations carried out by M.T.M. Koper **[25]** have demonstrated that the energy difference between the bonding energies of the -OH and -OOH intermediates exceeds the ideal value of 1.23 eV. As a result, significant overpotentials occur at the surface of catalytic materials when following the reaction mechanism proposed by Norskov et al. **[21, 22]** for the OER.

In the study conducted by Norskov and colleagues **[21, 22]**, they propose a limited number of three reactive intermediates. However, several articles have indicated the involvement of additional reactive intermediates, particularly those of the -OO type, suggesting that the scaling relations described by Norskov et al. are only partially accurate.

Fig. I. 10 represents the multi-step mechanism of the OER in both acidic and alkaline environments, in the presence of an active site (S). While there are similarities in the proposed mechanisms found in the literature, there are also divergences, primarily concerning the formation of molecular oxygen **[26]**.

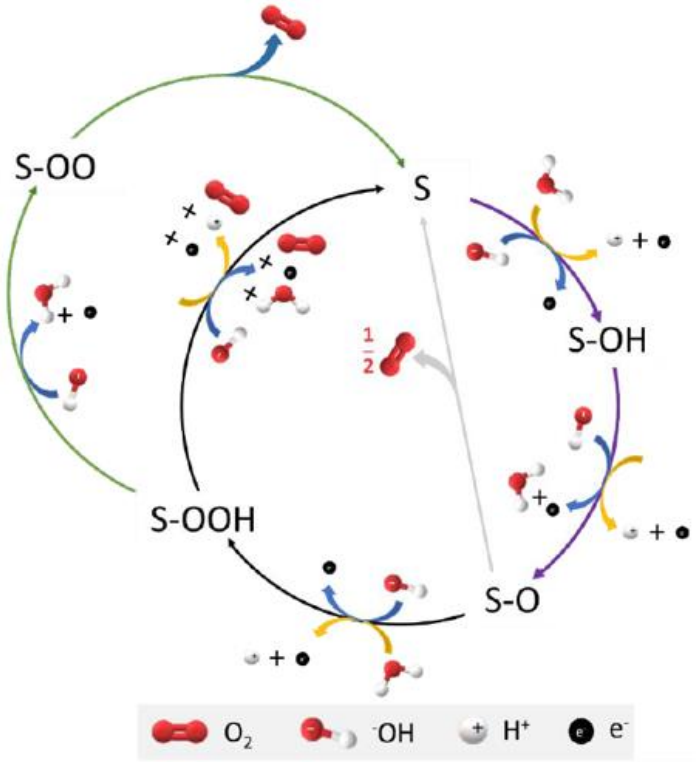

Fig. I. 10. Reaction mechanisms of OER in an acidic environment (yellow arrows) and in an alkaline environment (blue arrows). The gray arrows correspond to an associative mechanism, and the purple arrows represent a dissociative mechanism **[26, 27]**.

By altering the inherent properties of catalytic materials, it becomes possible to decrease overpotentials and enhance the kinetics of the OER. Until now, the majority of studies on catalysts for the OER have been conducted in alkaline environments due to the lower stability of non-noble metals, which are the constituent materials, in acidic conditions. Numerous materials have been developed, including oxides **[28]**, hydroxides **[29]**, layered double hydroxides (LDH) **[30]**, metal-organic frameworks (MOFs) **[31]**, and heteroatom-doped compounds **[32]**. Furthermore, Perovskite-type oxides (ABO_3) are anticipated to be one of the most promising alternate catalysts for the OER. A brief background about using this type of catalyst is provided in chapter three.

I.3.1.5. Applications of green hydrogen

The development and utilization of green hydrogen are attracting growing interest from a widening range of developers and manufacturers. With continuous improvements in performance, hydrogen is finding increasing applications across sectors (Fig. I. 11):

- **Energy Storage**: hydrogen can be used as a means of energy storage, helping to balance the intermittent nature of renewable energy sources. Excess renewable energy can be used to produce hydrogen, which can be stored and converted back to electricity when needed.
- **Fuel for Transportation**: hydrogen can be used as a clean fuel for various modes of transportation (cars, buses, trains, and ships), providing zero-emission transportation.
- **Industrial Processes**: Green hydrogen can be utilized as a feedstock or fuel in various industrial processes, such as ammonia production, methanol production, refineries, and steel manufacturing. It can replace fossil fuels, reducing greenhouse gas emissions.

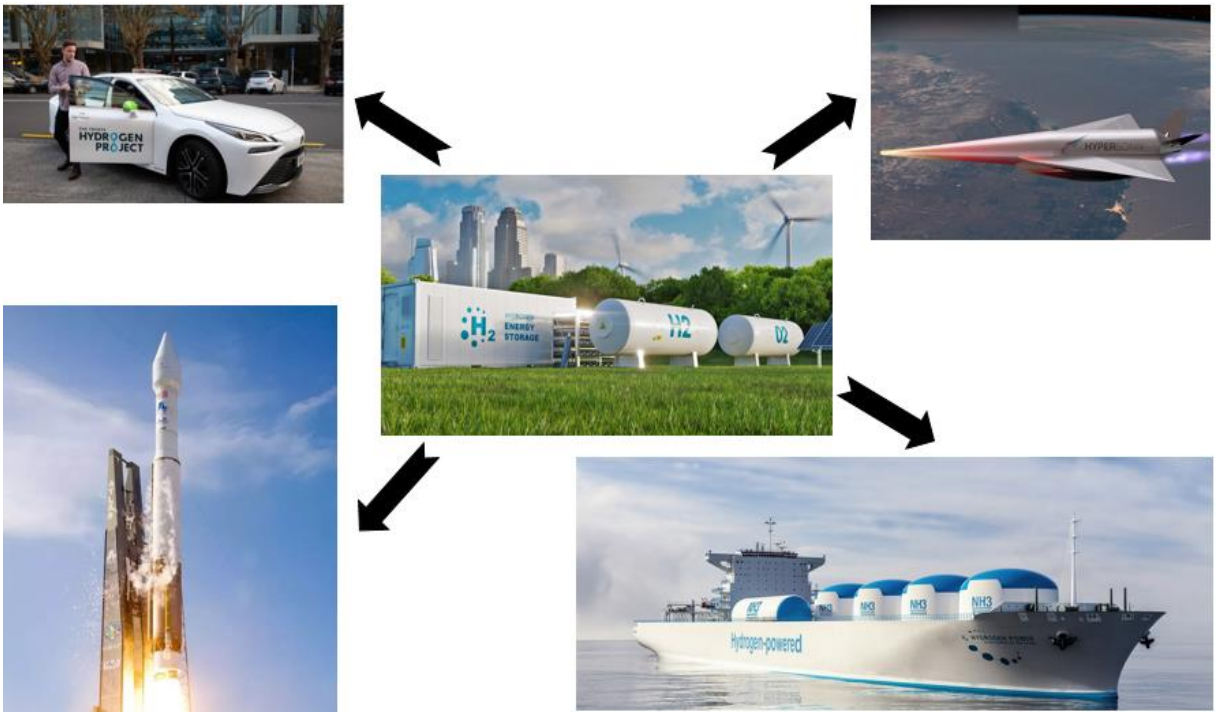

Fig. I. 11. Some applications of green hydrogen.

I.3.2. Electrochemical supercapacitor (ESC)

I.3.2.1. Brief historical overview

The technology of capacitors originated with the invention of the Leyden jar (1745-1746), which comprised glass containers containing a metal foil (Fig. I. 12) **[33]**. The metal foil acted as an electrode, while the jar functioned as a dielectric. In the charging process of the device mentioned above, one electrode accumulated positive charge (+), while the other electrode accumulated negative charge (-). Connecting these charges using metal wires initiates a discharge process.

Fig. I. 12. the Leyden jar.

However, the understanding of static electricity storage did not emerge until the introduction of the electric double layer model, which was initially proposed by the German physicist Helmholtz in the 19th century (Fig. I. 13). Helmholtz emphasized that the presence of static electricity at the interface between the electrode and the electrolyte leads to the formation of two closely charged layers, each carrying equal but opposite charges, with a

distance approximately equal to the diameter of an atom. Subsequently, Gouy, Chapman, and Stern further developed the Gouy-Chapman and Stern models based on Helmholtz's original model.

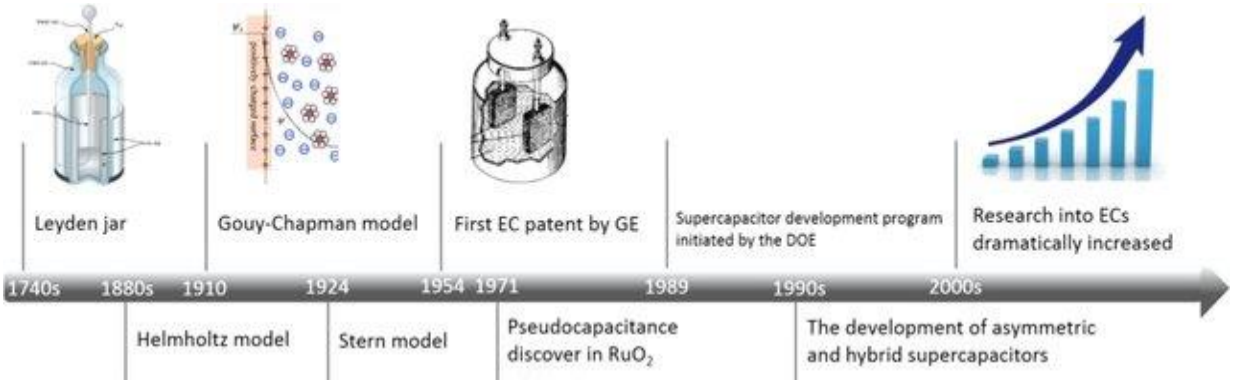

Fig. I. 13. Historical chronology of the development of supercapacitors.

In 1957, Becker was granted a patent for the first supercapacitor (EDLC) that utilized activated carbon as an electrode plate **[34]**. The EDLC operates with static charge storage (non-faradaic), meaning there is no transfer of charge between the electrode and the electrolyte. This characteristic contributes to its high reversibility and stability. Following Becker's work, the company Sohio, located in Cleveland, Ohio, also employed a carbon material with a large surface area for double-layer capacitors. These capacitors utilized a non-aqueous solvent electrolyte that contained dissolved Tetramethylammonium salt. By using this setup, they were able to achieve a higher operating voltage (3.4~4.0 V) compared to aqueous electrolytes, thanks to the higher decomposition voltage of the non-aqueous electrolyte. Consequently, these capacitors could accommodate higher charge densities and provide greater specific energy storage. This is because the energy that can be stored increases with the square of the attainable charging voltage.

In order to enhance the specific capacitance of SCs (Supercapacitors), Trasatti et al. made a significant finding in 1971. They developed a novel electrochemical capacitor utilizing a RuO_2 film that operates through the Faraday process, referred to as a pseudo-capacitor **[35]**. This discovery introduced a fresh approach to improve the charge storage capacity of electrochemical capacitors. Subsequently, from 1975 to 1980, B. E. Conway conducted thorough research on pseudo-capacitors using RuO_2.

In 1989, the US Department of Energy (DOE) initiated long-term research with the goal of developing high-energy-density supercapacitors specifically for electric propulsion systems. This research was part of the DOE's program for electric and hybrid vehicles. Subsequently, Maxwell Technologies, a prominent manufacturer in the supercapacitor industry, entered into a contract with the DOE to develop high-performance supercapacitors. These advanced supercapacitors were intended to complement batteries or fuel cells in electric or hybrid vehicles, enabling them to capture regenerative braking energy and release electric energy for acceleration. Since then, supercapacitor companies worldwide, such as Nesscap (Korea), ELTON (Russia), Nippon Chemicon (Japan), and CAP-XX (Australia), have made significant progress in the development and delivery of various types of supercapacitors, including EDLCs, pseudo-capacitors, and asymmetric supercapacitors, for a wide range of applications.

Starting from the year 2000, there has been a notable rise in research concerning supercapacitors due to the growing need for high-power, reliable, and safe energy storage solutions. Alongside this, the rapid progress in nanoscience and advanced characterization technologies has played a crucial role in the development of Electric Double-Layer Capacitors (EDLCs) and pseudo-capacitors. These advancements have paved the way for extensive

research focused on the charge storage mechanism to further enhance their capabilities.

I.3.2.2. Fundamental principles

Typically, an ESC storage device comprises a pair of electrodes (collectors with active materials), an electrolyte, and a separator (Fig. I. 14). The two electrodes are impregnated with the electrolyte and electrically insulated by the separator which is designed to enable ion mobility.

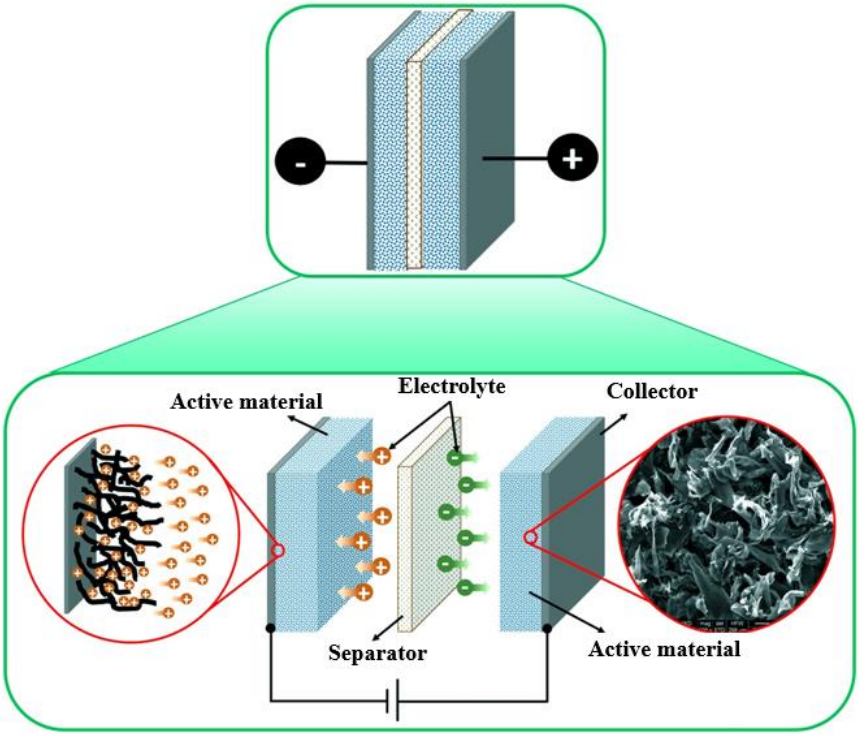

Fig. I. 14. Schematic representation of a supercapacitor cell.

I.3.2.2.1. Current collectors

Current collectors play a crucial role in facilitating the flow of electrons between the electrode material and the external circuit. Notably, the resistance at the interface between the current collector and the electrode material may substantially contribute to the internal resistance **[36]**. In order to reduce the internal resistance of the device, it is essential to choose

a material that is an exceptional electronic conductor, exhibits chemical and electrochemical stability towards the electrolyte, and has the lowest possible volumetric mass. Moreover, the current collector may act as a framework to support the electrode material, necessitating excellent mechanical stability and maximum flexibility. Hence, ensuring an intimate contact between the electrode material and the collector is critical.

Aluminum is commonly used as the material of choice, particularly for non-aqueous devices, due to its lightweight nature, stable surface condition owing to a thin, alumina passivation layer, and its high conductivity ($37{,}7.10^6$ S/cm), which makes it an excellent candidate for current collectors. In situations where aluminum is not compatible with the device or its operating conditions (due to the issues such as corrosion, alloying, etc.), it can be substituted with metallic nickel or copper, or stainless steel alloys **[37]**.

I.3.2.2.2. Separator

The separator typically is a membrane that can be distinguished by its level of porosity, tortuosity, and wettability with regard to the electrolyte. The wetting behavior of the membrane is also a crucial factor in mitigating resistance at the interface between the electrolyte and separator **[38]**. The supercapacitor's internal resistance is mostly caused by the [porous membrane + electrolyte] system, accounting for more than 30% of the overall resistance **[39]**. To enhance the [porous membrane + electrolyte] system's conductivity, the separator's porosity and chemical composition must be adjusted to match the electrolyte. The tortuosity of the separator should be minimized while preserving its mechanical strength. Celgard® separators are currently the most prevalent membranes used in supercapacitors. These separators are made up of either a single layer of polypropylene (PP), polyethylene

(PE), or triple layers of PP/PE/PP. However, other types of membranes are also employed, such as:

- Cellulosic papers are highly hydrophilic and are therefore favored for use in aqueous systems **[40]**.
- Membranes made of polyvinylidene fluoride and its copolymer derivatives are preferred for high-temperature applications or for use with electrolytes that have particularly aggressive (corrosive) physicochemical properties **[41]**.

Research is ongoing in the area of current separator and collector technologies, the two main areas of research are focused on electrolytes and electrode materials, which are responsible for the electrochemical storage properties of the system.

I.3.2.2.3. Electrolyte

The electrolyte is primarily a conducting medium, and this conduction is ensured by the mobility of ions within it. Its main characteristic is therefore ionic conductivity, which is linked to ion diffusion, in other words, their mobility within the matrix. Several electrolytes can be distinguished according to their state, nature, and range of temperature of use:

- **Gel electrolyte**

The idea of using gelled electrolytes to prevent electrolyte leakage is not new. In 1957, Otto Jache and Heinz Schroeder patented and popularized the modern (and industrial-scale) formulation of gelled electrolytes, which led to the commercialization of the first VRLA battery (by the German company Accumulatorfabrik Sonnenschein).

In recent times, there has been an increase in the development of various methods to create high-performance gel electrolytes. These methods involve the encapsulation of ionic

salts, liquid electrolytes (such as polyvinyl alcohol PVA and H_2SO_4 **[42]**), and more recently, ionic liquids (such as polyvinylidene difluoride PVdF and butylmethylimidazolium-tetrafluoroborate $C_1C_4ImBF_4$ **[43]**), within polymer matrices or porous silica **[44]**. However, it is important to note that the ionic conductivity of these systems, which is in the range of a few thousandths of S/cm, still remains lower compared to that of liquid electrolytes.

- **Liquid electrolyte**

The primary benefit of liquid electrolytes, in contrast to gels, ionogels, and conductive glasses, is their exceptional transport properties. Unlike in gels or glasses, the viscosity in a liquid is considerably lower, allowing for unhindered diffusion of species. Liquid electrolytes can be classified into three separate categories depending on their chemical composition: aqueous electrolytes, organic electrolytes, and ionic liquids. However, regardless of the category, it is crucial to consider the electrode material when selecting an electrolyte to ensure maximum compatibility between the electrode and electrolyte, as well as to optimize the electrode-electrolyte interface. This consideration is essential for the development of a dependable and commercially viable device.

I.3.2.2.4. Electrode material

Electrode materials commonly consist of three distinct components, each serving specific functions.

- **The active material**

This component of the electrode material (generally is in powder form mixed with a binder and black carbon) enables electron exchange and the accumulation of charges (negative or positive) on the surface, resulting in the polarization of the electrode/electrolyte

interface. In the case of pseudo-capacitive or faradaic materials, the active material is where the electrode's redox processes occur.

- **The electronic conductor**

The active material often has inherent low electronic conductivity. As a result, its distribution within the material can impede electronic conduction in the electrode by increasing the length of electron diffusion paths from the active site to the current collector. These electronic transfer resistances between the active site and current collector can be minimized through charge percolation. To achieve this, an additive of highly electron-conductive material can be utilized in combination with the active material. Black Carbon (BC) powder is commonly employed for this purpose. It exhibits intrinsic electronic conductivity on the order of 0.2 S/cm at 25 kPa pressure **[45]**. One advantage of BC is its minimal contribution to the capacitive component, estimated to be around 12 F/g during cycling in an aqueous environment **[46]**.

- **The binder**

Typically, active materials and electronic conductors (percolates) are in the form of powders. To ensure the cohesion of particles and the adherence of the electrode material to the current collector, a polymer binder is necessary. This polymer binder plays a crucial role in preserving the mechanical stability of the electrode material.

Polymers offer a high degree of versatility and can be easily functionalized, enabling the development of various fluorinated polymers suitable for [electrode/electrolyte] systems. Polyvinylidene fluoride (PVDF) is commonly used to produce inks by mixing it with the solvent N-methyl-pyrrolidone (NMP) **[47]**. Similarly, polytetrafluoroethylene (PTFE) finds

application in composite pastes **[48]**. Additional polymers, such as poly (vinyl alcohol) (PVA) and poly (vinyl alcohol-co-vinyl acetate) (PVA-co-PVAc) copolymers, can also be employed. Carboxy-methyl cellulose (CMC) serves as an interesting binder for the design of electrode inks in aqueous environments **[49]**. In industrial settings, electrodes are commonly prepared by applying ink onto a current collector strip, resulting in a rolled configuration. The formulation of the inks plays a crucial role in obtaining electrodes with satisfactory mechanical quality. As a result, it undergoes optimization through a combination of experimental methods and numerical simulations **[50]**.

The selection of electrode materials and their fabrication are vital factors in improving the capacitive performance of ESC **[51]**. ESC electrodes must possess characteristics such as thermal stability, specific surface area (SSA), corrosion resistance, high electrical conductivity, suitable chemical stability, and favorable surface wettability. Additionally, they should be cost-effective and environmentally friendly. Furthermore, their ability to transfer faradic charge plays a significant role in enhancing capacitance performance **[52,53]**. Numerous materials have been developed, including carbon-based materials **[54]**, transition metal oxides **[55]**, layered double hydroxides (LDH) **[56]**, and metal-organic frameworks (MOFs) **[57]**. Furthermore, Perovskite-type oxides (ABO_3) are anticipated to be one of the most promising materials for supercapacitor electrodes. A brief background about using this type of materials is provided in the introduction of chapter four.

I.3.2.3. Energy storage mechanism

Depending on the charge storage mechanism, SCs can be divided into three categories:

I.3.2.3.1. Electrochemical double layer capacity (EDLC)

The behavior of electrode materials in EDLC devices in ESC systems is connected to the gathering of electrostatic charges at the interface, which is contingent upon the potential of the electrode. The generation mechanism of surface electrode charge includes surface dissociation and the adsorption of ions from both the electrolyte and defects in the crystal lattice. These processes exclusively operate through the electrostatic accumulation of surface charge. As depicted in Fig. I. 15, the electrical capacitance of the double layer originates from the electrode material particles situated at the interface between the carbon particles and the electrolyte. A surplus or deficiency of electric charges accumulates on the electrode's surface, leading to the buildup of electrolyte ions with compensating charges on the electrolyte side to maintain electro-neutrality. During the charging process, electrons transfer from the negative electrode to the positive electrode via an external circuit. In the electrolyte, cations move towards the negative electrode, while anions move towards the positive electrode. The reverse processes occur during discharge. Therefore, the electrical energy of a supercapacitor like this is anticipated to be stored at the double-layer interface through a reversible process of ion adsorption, which also contributes to the accumulation of surface charges through electrostatic means. The performance of an EDLC is linked to the accumulation of electrostatic charges on the electrode's surface or within its pores.

In this particular energy storage system, there is no transfer of charges across the electrode/electrolyte interface, and there are net exchanges of ions between the electrode and

the electrolyte. Consequently, the concentration of the electrolyte remains constant throughout the charging and discharging processes. Moreover, the performance of EDLC electrode materials is distinguished by nearly rectangular cyclic voltammetry (CV) curves and triangular galvanostatic charge-discharge (GCD) curves (Fig. I. 15).

The thickness of the double layer (d) is determined by the concentration of the electrolyte and the size of ions. For concentrated electrolytes **[58]**, this value typically falls within the range of 5 to 10 Å. In order to boost the capacity of the EDLC, it is important to focus on increasing the specific surface area. Consequently, electrode materials that possess a high SSA are indispensable for the development of supercapacitors with exceptional performance.

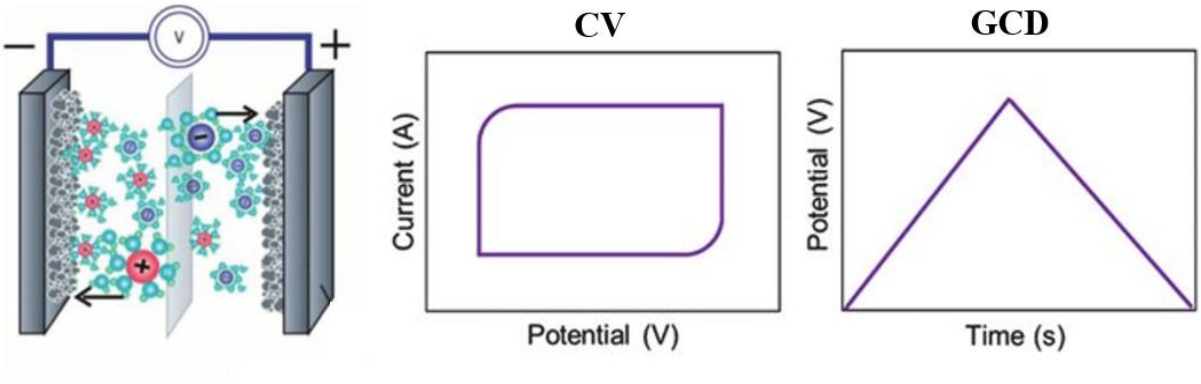

Fig. I. 15. Schematic illustration of electrical double layer capacitance (EDLC) and a summary of characteristic measurements such as CV, GCD.

I.3.2.3.2. Pseudo-capacity

"Pseudocapacitance" refers to the characteristics of electrode materials such as RuO_2 and MnO_2 that demonstrate behavior similar to capacitors in their electrochemical signature. When an electric potential is applied to these electrodes, a fast and reversible faradaic reaction

takes place on the electrode material surface, allowing charges to move through the double layer. Unlike carbon-based materials that exhibit the electrochemical signature of a capacitive electrode, this type of electrode material stores charge through various reaction mechanisms, including surface redox reactions and intercalation mechanisms (see Fig. I. 16) **[59]**.

In the case of the surface redox pseudocapacitance process, charges are typically stored through the adsorption-desorption of cations and anions from the electrolyte onto the surface of the electrode material. Faradaic redox reactions occur during this process. Materials that are primarily influenced by surface redox pseudocapacitance behave similarly to EDLC-based materials, showing nearly rectangular CV curves (Fig. I. 16). Electrode materials that exhibit pseudocapacitive behavior consist mainly of metallic oxide/sulfide and conductive polymer.

The energy storage process in intercalation pseudocapacitance involves the reversible intercalation/deintercalation of cations (such as H^+, Li^+, Na^+, K^+, etc.) from the electrolyte into the crystalline structure of the electrode materials (refer to Fig. I. 16). It is worth noting that the intercalation pseudocapacitance process does not cause any phase changes in the material. Moreover, materials exhibiting dominant intercalation pseudocapacitive behavior can be identified by the presence of broad redox peaks observed in the CV curves.

Pseudocapacitive behavior enables pseudocapacitors to attain a much higher charge storage capacity in comparison to EDLCs. The capacity value is 10 to 100 times higher than that of typical EDLCs **[58]**. Nevertheless, electrode materials demonstrating pseudocapacitive behavior are more susceptible to expansion and contraction during the charge/discharge process, leading to compromised mechanical stability and reduced cycle stability.

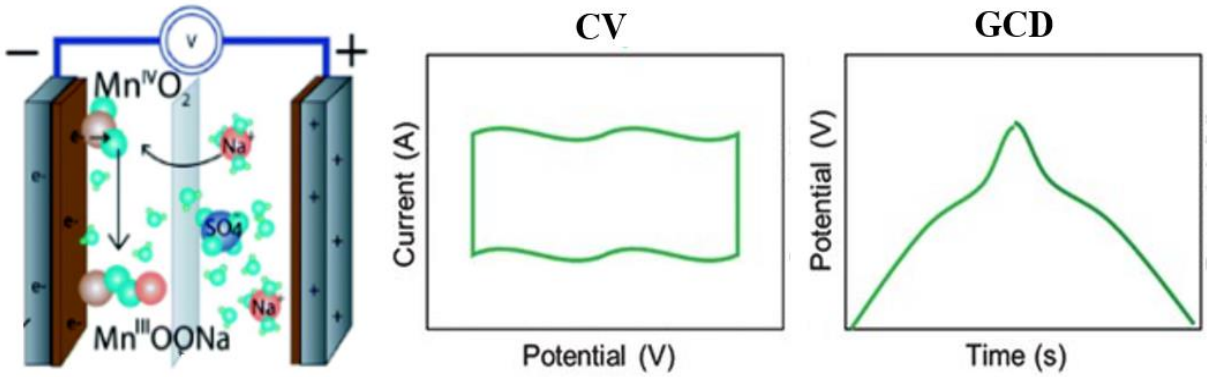

Fig. I. 16. Schematic illustration of pseudocapacitive behavior and a summary of characteristic measurements such as CV, GCD.

I.3.2.3.3. Battery-like behavior

Despite the established definition of pseudocapacitance, numerous electrode materials that experience a phase change during the charge/discharge process have been historically misclassified as pseudocapacitive materials. Recently, the electrochemical community has successfully discerned the disparity between electrode materials demonstrating battery-like behavior and those displaying traditional pseudocapacitive behavior.

In comparison to pseudocapacitive electrode materials, the electrochemical reactions of battery-type materials are influenced by the ionic diffusion of the electrolyte. They typically involve ion intercalation and/or phase transformation alloy reactions (Fig. I. 17), which can be observed in cyclic voltammetry (CV) curves through distinct redox peaks. In galvanostatic charge-discharge (GCD) curves, the charging process leads to the oxidation of low-valence transition metals to a higher valence state for electron release, followed by their reduction back to the original state during discharge. Consequently, low-valence compounds experience at least one phase change in each charge and discharge cycle, resulting in the emergence of a

potential plateau in the GCD curves **[60]**. According to this revised definition, electrode materials that demonstrate a potential plateau during the electrochemical charge/discharge process alongside clear redox peaks should be classified as "battery-type" electrode materials (Fig. I. 17).

When assessing charge storage capacity, battery-type electrode materials, like batteries, typically exhibit a high charge storage capability. Furthermore, battery-type electrode materials that incorporate specifically engineered nanostructures are anticipated to possess a large specific surface area, facilitating an abundance of active sites for redox reactions and shorter ion diffusion pathways within the electrolyte. Nevertheless, subpar performance and inadequate cycling stability may arise during the charge/discharge process due to the sluggish kinetics associated with the material's gradual phase transformation.

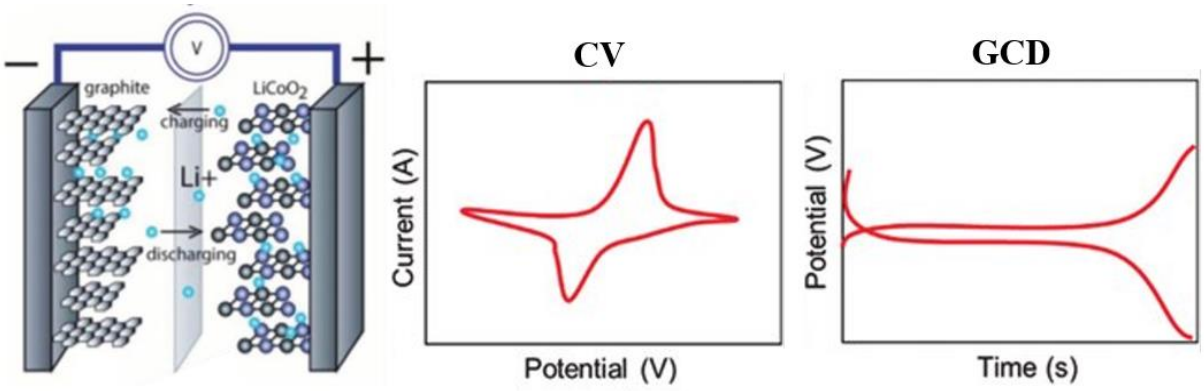

Fig. I. 17. Schematic illustration of battery-like behavior and a summary of characteristic measurements such as CV, GCD.

In contrast to the behavior of electric double-layer capacitors (EDLC) and pseudocapacitance, the concept of "capacitance (F)" is not applicable to battery-type behavior. Previous studies have defined capacitance as the ability of a body to store electrical charge,

with a constant value within a specific potential range. This value can be used to calculate the stored charge using equation (**I.4**). However, the "capacity" of a battery-type electrode is not constant across the entire available potential range. Instead, it represents an "average" value calculated within a limited potential range, and choosing a wider or narrower potential range will result in a different calculated specific capacity **[61]**. In this context, "capacity" (mAh or coulomb C) is the most suitable and meaningful measure to use. The capacity of battery-type electrodes is determined by taking the derivative of charge acceptance (Δq) with respect to the change in potential (ΔV) **[62, 63]**:

$$C\left(\frac{mA.h}{g}\right) = \frac{Q}{m} = \frac{I.\Delta t}{3600.m} \quad \text{(I.4)}$$

Where C (mAh/g) is the specific capacity, Q is the amount of charge, m (g) is the mass of the active material, I (mA) is the constant discharge current, and Δt (s) is the discharge time.

$$C\left(\frac{C}{g}\right) = \frac{Q}{m} = \frac{I.\Delta t}{m} \quad \text{(I.5)}$$

Where C (C/g) is the specific capacity, Q is the amount of charge, m (g) is the mass of the active material, I (A) is the constant discharge current, and Δt (s) is the discharge time.

I.3.2.4. Classifications of ESC

Classifications based on the chemical reactions and device architecture divide supercapacitors into three types: i) symmetrical supercapacitors (SCs), ii) asymmetrical supercapacitors (ASCs), and iii) hybrid supercapacitors (HSCs) **[64]**.

Typically, SCs consist of two similar electrodes, with the same charge storage mechanisms (Fig. I. 18.a), that have equal weight, thickness, material, etc. However, it is crucial to acknowledge that SCs may not always be the optimal choice when designing

supercapacitors. On the contrary, ASCs consist of two dissimilar electrodes with the same charge storage mechanisms (Fig. I. 18.b). To achieve optimal performance, ASCs can be optimized by ensuring a balance of charge through matching the mass of the positive and negative electrodes (as described in equations **I.6** and **I.7**). This electrode configuration enhances their suitability for applications in energy storage systems **[65].**

$$Q = C.\Delta V.m \quad \ldots\ldots\ldots\ldots\ldots\ldots\ldots\ldots\ldots\ldots \textbf{(I.6)}$$

$$\frac{m^+}{m^-} = \frac{C^+.\Delta V^+}{C^-.\Delta V^-} \quad \ldots\ldots\ldots\ldots\ldots\ldots\ldots\ldots\ldots\ldots \textbf{(I.7)}$$

where C (F/g) is the specific capacitances, m (g) is the active material mass and ΔV (V) is the potential window; the (-) and (+) signs refer to negative and positive electrodes respectively.

In recent years, a distinct type of ESCs called hybrid supercapacitors (HSCs) has emerged. These hybrid supercapacitors combine two dissimilar with different storage mechanisms to form the energy storage system (Fig. I. 18.c), resulting in expected improved performance compared to SCs and ASCs. For instance, one electrode demonstrates EDLC behavior, while the other exhibits battery-like faradaic behavior, serving as the negative and positive electrodes respectively. This configuration allows one-half of the hybrid supercapacitor to function as an EDLC, while the other-half behaves like a faradaic battery. As a result, HSCs offer high energy storage capabilities akin to batteries, along with high power and long lifespan similar to SCs **[66]**. Moreover, in HSCs design, optimizing the supercapacitor involves achieving a balance in charge by matching the mass of the positive and negative electrodes (as shown in equations **I.6** and **I.7**).

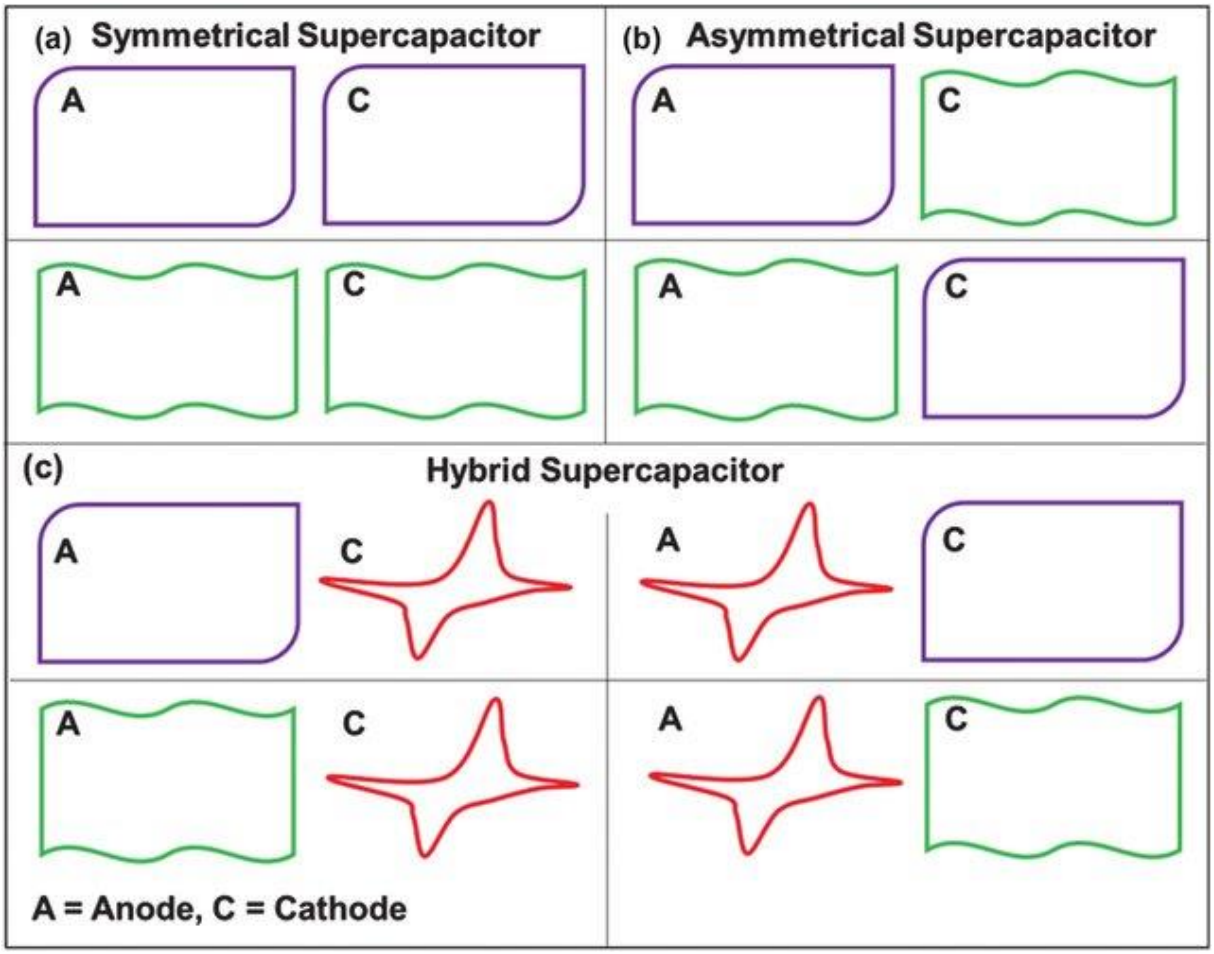

Fig. I. 18. Classifications of ESC; a) symmetrical supercapacitors, b) asymmetrical supercapacitors, and c) hybrid supercapacitors.

I.3.2.5. Applications of ESC

A growing number of developers and manufacturers are becoming increasingly interested in the development and utilization of ESC. As their performance continues to improve, ESC are finding more applications in various sectors such as public transportation, automobile, defense and military, and industrial applications (Fig. I. 19). Let's consider the example of their applications in electric vehicles. While the process of commercialization has been relatively slow, a few applications have been successfully implemented. These include hybrid-electric transit buses in the United States and China, electric braking systems in

passenger cars, and more recently, stop-go hybrid vehicles **[67]**. Notably, Aowei Technology Co., Ltd (Shanghai, China) has launched fast-charging electric buses that can be fully charged in just 90 seconds and travel a distance of 7.9 km. These buses have an average speed of 22 km/h and a maximum speed of 44.8 km/h **[58]**. Additionally, CSR Co. Ltd. (China) has developed a tram operating on an EDLC configuration, with a charging time of 30 seconds and a distance range of 3 to 5 km **[68]**.

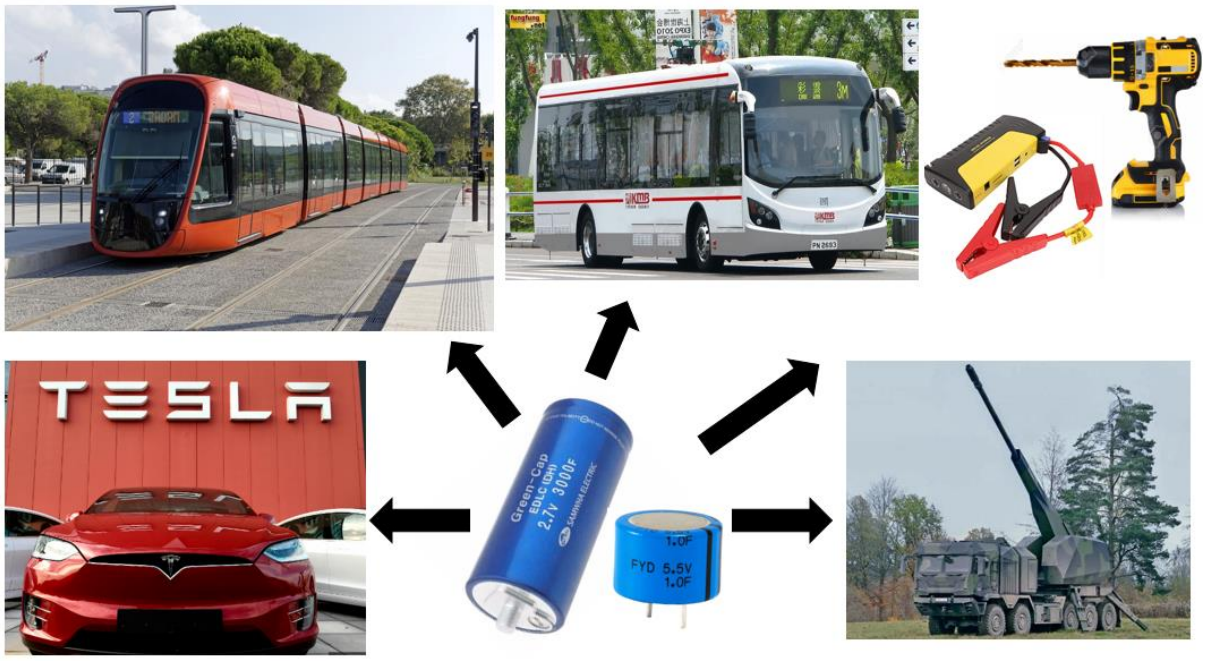

Fig. I. 19. Some applications of electrochemical supercapacitor.

References

[1] E. Omari, Doctoral thesis, University of Mohamed Khider Biskra (2021).

[2] V.M. Goldschmidt, Skr. Nor. Videnk. Akad., Kl.1: Mat. Narurvidensk. Kl.8 (1926).

[3] N. Tsuda, K. Nasu, A. Fujimori, and K. Siratori. Electronic conduction un oxides. Springer-Verlag, Berlin, (2000).

[4] Kour, R.; Arya, S.; Verma, S.; Gupta, J.; Bandhoria, P.; Bharti, V.; Datt, R.; Gupta, V. Potential Substitutes for Replacement of Lead in Perovskite Solar Cells: A Review. Global Challenges 2019, 3 (11), 1900050.

[5] H. Lidjici, Doctoral thesis, University of Toulouse (2011).

[6] Kittel, Charles. Introduction to Solid State Physics, 8th edition, John Wiley & Sons, Inc., 2005, pp. 268-270.

[7] J. Philibert, A. Vignes, Y. Bréchet, P. Combrade, Métallurgie Du minerai au matériau, 2nd edition, Dunod (2002).

[8] S. Makhloufi, Doctoral thesis, University of Mohamed Khider Biskra (2016).

[9] O. Mdller, R. Roy, the Major Ternary Structural Families, Springer, New York, (1974).

[10] R. Benakcha, Doctoral thesis, University of Mohamed Khider Biskra (2017).

[11] Dragan, M., Enache, S., Varlam, M., & Petrov, K. (2020). Perovskite-Based Materials for Energy Applications. IntechOpen. doi: 10.5772/intechopen.91271

[12] T. Smolinka, H. Bergmann, J. Garche, M. Kusnezoff, The history of water electrolysis from its beginnings to the present. In: Electrochemical Power Sources: Fundamentals, Systems, and Applications. Elsevier, 2022. p. 83-164.

[13] P. Millet and S. Grigoriev, “Water Electrolysis Technologies,” Renew. Hydrog. Technol.

Prod. Purification, Storage, Appl. Saf., 2013. p. 19–41.

[14] A. Godula-Jopek, Hydrogen Production. 2015.

[15] Ursua, A. Hydrogen Production from Water Electrolysis: Current Status and Future Trends. Proc. IEEE 100, 410–426 (2012).

[16] Schroder, V., Emonts, B., Janssen, H. & Schulze, H. P. Explosion limits of hydrogen/oxygen mixtures at initial pressures up to 200 bars. Chem. Eng. Technol. 27, 847–851 (2004).

[17] Smolinka, T., Günther, T. & Garche, J., NOW-Studie, Overview on water electrolysis for hydrogen production and storage. Tech. report, Fraunhofer ISE (2011).

[18] M. David, C. Ocampo-Martínez, and R. Sánchez-Peña, "Advances in alkaline water electrolyzers: A review," J. Energy Storage, vol. 23, no. March 2019, pp. 392–403

[19] L. LOUPIAS, Doctoral thesis, University of Poitiers (2016).

[20] S. Giménez and J. Bisquert, Photo-electrochemical solar fuel production: From basic principles to advanced devices. 2016.

[21] J. K. Nørskov et al., "Origin of the overpotential for oxygen reduction at a fuel-cell cathode," J. Phys. Chem. B, vol. 108, no. 46, pp. 17886–17892, 2004.

[22] V. Viswanathan, H. A. Hansen, J. Rossmeisl, and J. K. Nørskov, "Universality in oxygen reduction electrocatalysis on metal surfaces," ACS Catal., vol. 2, no. 8, pp. 1654–1660, 2012.

[23] J. Rossmeisl, Z. W. Qu, H. Zhu, G. J. Kroes, and J. K. Nørskov, "Electrolysis of water on oxide surfaces," J. Electroanal. Chem., vol. 607, no. 1–2, pp. 83–89, 2007.

[24] I. C. Man et al., "Universality in Oxygen Evolution Electrocatalysis on Oxide Surfaces," ChemCatChem, vol. 3, no. 7, pp. 1159–1165, 2011.

[25] M. T. M. Koper, "Thermodynamic theory of multi-electron transfer reactions: Implications for electrocatalysis," J. Electroanal. Chem., vol. 660, no. 2, pp. 254–260, 2011.

[26] A. Habrioux, C. Morais, T. W. Napporn, and B. Kokoh, "Recent trends in hydrogen and oxygen electrocatalysis for anion exchange membrane technologies," Curr. Opin. Electrochem., no. February, 2020.

[27] H. Jin et al., "Emerging Two-Dimensional Nanomaterials for Electrocatalysis," Chem. Rev., vol. 118, no. 13, pp. 6337–6408, 2018.

[28] Y. Lu, D. Fan, Z. Chen, W. Xiao, C. Cao, and X. Yang, "Anchoring Co_3O_4 nanoparticles on MXene for efficient electrocatalytic oxygen evolution," Sci. Bull., vol. 65, no. 6, pp. 460–466, Mar. 2020.

[29] K. Zhao, X. Ma, S. Lin, Z. Xu, and L. Li, "Ambient Growth of Hierarchical FeOOH/MXene as Enhanced Electrocatalyst for Oxygen Evolution Reaction," ChemistrySelect, vol. 5, no. 6, pp. 1890–1895, 2020.

[30] M. Yu, S. Zhou, Z. Wang, J. Zhao, and J. Qiu, "Boosting electrocatalytic oxygen evolution by synergistically coupling layered double hydroxide with MXene," Nano Energy, vol. 44, pp. 181–190, 2018.

[31] L. Zhao et al., "Inter diffusion Reaction-Assisted Hybridization of Two-Dimensional Metal-Organic Frameworks and $Ti_3C_2T_x$ Nanosheets for Electrocatalytic Oxygen Evolution," ACS Nano, vol. 11, no. 6, pp. 5800–5807, 2017.

[32] T. Y. Ma, J. L. Cao, M. Jaroniec, and S. Z. Qiao, "Interacting carbon nitride and titanium carbide nanosheets for high-performance oxygen evolution," Angew. Chemie - Int. Ed., vol. 55, no. 3, pp. 1138–1142, 2016.

[33] D.A.J. Rand, A journey on the electrochemical road to sustainability, Journal of Solid-State Electrochemistry, 15 (2011) 1579-1622.

[34] I. Jiya, N. Gurusinghe, R. Gouws, Electrical Circuit Modelling of Double Layer Capacitors for Power Electronics and Energy Storage Applications: A Review, Electronics, 7 (2018) 268.

[35] K. Kuratani, H. Tanaka, T. Takeuchi, N. Takeichi, T. Kiyobayashi, N. Kuriyama, Binderless fabrication of amorphous RuO_2 electrode for electrochemical capacitor using spark plasma sintering technique, Journal of Power Sources, 191 (2009) 684-687.

[36] M. Abdelkader, Doctoral thesis, University of Science and Technology HOUARI BOUMEDIENE (2021).

[37] Kühnel R.-S., Lübke M., Winter M., Passerini S. and Balducci A., Suppression of aluminum current collector corrosion in ionic liquid containing electrolytes, Journal of Power Sources 214 (2012) 178-184.

[38] Daux V., Elaboration et modification de séparateurs macroporeux innovants pour générateurs électrochimiques, Thèse, Université Jean Monnet - Saint-Etienne, 2011.

[39] Perricone E., Mise au point d'électrolytes innovants et performants pour supercondensateurs, Thèse, Université de Grenoble, 2011.

[40] Tonurist K., Janes A., Thomberg T., Kurig H. and Lust E., Influence of Mesoporous Separator Properties on the Parameters of Electrical Double-Layer Capacitor Single Cells, J. Electrochem. Soc. 156 (2009) 334-342.

[41] Karabelli D., Lepretre J. C., Alloin F. and Sanchez J. Y., Poly (vinylidene fluoride)-based macroporous separators for supercapacitors, Electrochim. Acta, 57 (2011) 98-103.

[42] Meng C., Liu C. and Fan S., Flexible carbon nanotube/polyaniline paper-like films and their enhanced electrochemical properties, Electrochem. Commun., 11 (2009) 186-189.

[43] Ho C. C., Steingart D. A., Evans J. W. and Wright P. K., Tailoring electrochemical capacitor energy storage using direct write dispenser printing, ECS Trans., 16 (2008) 35-47.

[44] Kang Y. J., Chung H., Han C.-H. and Kim W., All-solid-state flexible supercapacitors based on papers coated with carbon nanotubes and ionic-liquid based gel electrolytes, Nanotechnology, 23 (2012) 1-6.

[45] Sánchez-González J., Macías-García A., Alexandre-Franco M. F. and Gómez-Serrano V., Electrical conductivity of carbon blacks under compression, Carbon, 43 (2005) 741-747.

[46] Brousse T., Taberna P.-L., Crosnier O., Dugas R., Guillemet P., Scudeller Y., Zhou Y., Favier F., Bélanger D. and Simon P., Long-term cycling behavior of asymmetric activated carbon/MnO_2 aqueous electrochemical supercapacitor, Journal of Power Sources, 173 (2007) 633-641.

[47] Sopcic S., Rokovic M. K. and Mandic Z., Preparation and characterization of RuO_2/polyaniline/polymer binder composite electrodes for supercapacitor applications, J. Electrochem. Sci. Eng. 2 (2012) 41-52.

[48] Tsay K.-C., Zhang L. and Zhang J., Effects of electrode layer composition/thickness and electrolyte concentration on both specific capacitance and energy density of supercapacitor, Electrochimica Acta, 60 (2012) 428-436.

[49] Wang Z., Dupré N., Gaillot A.-C., Lestriez B., Martin J.-F., Daniel L., Patoux S. and Guyomard D., CMC as a binder in $LiNi_{0.4}Mn_{1.6}O_4$ 5 V cathodes and their electrochemical performance for Li-ion batteries, Electrochimica Acta, 62 (2012) 77-83.

[50] Cerbelaud M., Lestriez B., Guyomard D., Videcoq A. and Ferrando R., Brownian Dynamics Simulations of Colloidal Suspensions Containing Polymers as Precursors of Composite Electrodes for Lithium Batteries, Langmuir, 28 (2012) 10713-10724.

[51] Lai, L.; Yang, S.; Wang, L.; Teh, B.K.; Zhong, J.; Chou, H.; Chen, L.; Chen, W.; Shen, Z.; Ruoff, R.S.; et al. Preparation of supercapacitor electrodes through selection of graphene surface functionalities. ACS Nano 2012, 6, 5941–5951.

[52] Xie, L. ; Sun, G.-H. ; Su, F. ; Guo, X. ; Kong, Q. ; Li, X. ; Huang, X. ; Wan, L. ; Song, W. ; Li, K. ; et al. Hierarchical porous carbon microtubes derived from willow catkins for supercapacitor applications. J. Mater. Chem. A 2016, 4, 1637–1646.

[53] Frackowiak, E.; Béguin, F. Carbon materials for the electrochemical storage of energy in capacitors. Carbon 2001, 39, 937–950.

[54] Wang, Y., Zhang, L., Hou, H., Xu, W., Duan, G., He, S., ... & Jiang, S. (2021). Recent progress in carbon-based materials for supercapacitor electrodes: a review. Journal of Materials Science, 56, 173-200.

[55] Ma, Y., Xie, X., Yang, W., Yu, Z., Sun, X., Zhang, Y., ... & Du, W. (2021). Recent advances in transition metal oxides with different dimensions as electrodes for high-performance supercapacitors. Advanced Composites and Hybrid Materials, 1-19.

[56] Guo, X. L., Liu, X. Y., Hao, X. D., Zhu, S. J., Dong, F., Wen, Z. Q., & Zhang, Y. X. (2016). Nickel-manganese layered double hydroxide nanosheets supported on nickel foam for high-performance supercapacitor electrode materials. Electrochimica Acta, 194, 179-186.

[57] Raza, N., Kumar, T., Singh, V., & Kim, K. H. (2021). Recent advances in bimetallic metal-organic framework as a potential candidate for supercapacitor electrode material.

Coordination Chemistry Reviews, 430, 213660.

[58] A. Muzaffar, M. B. Ahamed, K. Deshmukh, J. Thirumalai, A Review on Recent Advances in Hybrid Supercapacitors: Design, Fabrication and Applications, Renew. Sust. Energy Rev. 101 (2019) 123-145.

[59] V. Augustyn, P. Simon, B. Dunn, Pseudocapacitive Oxide Materials for High-rate Electrochemical Energy Storage, Energy Environ. Sci. 7 (2014) 1597-1614.

[60] W. Zuo, R. Li, C. Zhou, Y. Li, J. Xia, J. Liu, Battery-Supercapacitor Hybrid Devices: Recent Progress and Future Prospects, Adv. Sci. 4 (2017) 1600539.

[61] T. Brousse, D. Bélanger, J. W. Long, To Be or Not to Be Pseudocapacitive? J. Electrochem. Soc. 162 (2015) A5185-A5189.

[62] Y. X. Chen, D. Ni, X. W. Yang, C. C. Liu, J. L. Yin, K. F. Cai, Microwave-assisted Synthesis of Honeycomb like Hierarchical Spherical Zn-doped Ni-MOF as a High-Performance Battery-Type Supercapacitor Electrode Material, Electrochim. Acta 278 (2018) 114-123.

[63] Y. M. Lv, A. F. Liu, Z. X. Shi, H. W. Che, J. B. Mu, Z. C. Guo, X. L. Zhang, Construction of Hierarchical Zinc Cobalt Sulfide@Nickel Sulfide Core-Shell Nanosheets Arrays for High-Performance Asymmetric Solid-state Supercapacitors, Chem. Eng. J. 349 (2018) 397-407.

[64] M. R. Lukatskaya, B. Dunn, Y. Gogotsi, Multidimensional Materials and Device Architectures for Future Hybrid Energy Storage, Nat. Commun. 7 (2016) 12647.

[65] R. Sahoo, A. Pal, T. Pal, Proportion of Composition in a Composite Does Matter for Advanced Supercapacitor Behavior, J. Mater. Chem. A 4 (2016) 17440-17454.

[66] Y. Huang, C. Luo, Q. Zhang, H. Zhang, M.-S. Wang, Rational design of

three-dimensional branched NiCo-P@CoNiMo-P core/shell nanowire heterostructures for high-performance hybrid supercapacitor, J. Energy Chem. 61 (2021) 489–496,

[67] A. Burke, H. B. Zhao, Applications of Supercapacitors in Electric and Hybrid Vehicles, 5th ESSCAP (2015).

[68] Y. Wang, Y. Song, Y. Xia, Electrochemical Capacitors: Mechanism, Materials, Systems, Characterization and Applications, Chem. Soc. Rev. 45 (2016) 5925-5950.

Chapter II:

Synthesis and Characterization Techniques

This chapter is devoted to the description of the synthesis methods of the studied materials as well as the characterization techniques used, with a theoretical presentation and then a description of the conditions utilized during the analysis.

II.1. Synthesis Method

Various methods have been developed to prepare materials with different characteristics depending on their intended use. Chemical methods are widely used in material elaboration, offering precise control over the synthesis process to produce materials with tailored properties. Chemical methods can synthesize materials with properties like grain size, shape, porosity, surface area, homogeneity, and composition. Furthermore, chemical methods can be utilized to produce complex structures like nanoparticles, thin films, and composites with unique and adjustable properties. The most commonly used chemical processes include sol-gel, which is the technique used in this thesis, co-precipitation synthesis, and hydrothermal synthesis.

II.1.1. Sol-gel method

The term "sol-gel" stands for "solution-gelation" abbreviation. First, a "sol" is a stable dispersion of colloidal particles in a liquid **[1]**. The solid particles must be small enough (between 10–100 A°) so that the forces responsible for the dispersion (Brownian motion, Van der Waals interaction) are not overcome by the gravitational forces to remain dispersed **[2]**. Second, a "gel" is a solid, amorphous, three-dimensional array of macromolecules, swollen by a solvent and containing sub-micrometric pores. If the solid lattice is constituted of colloidal particles, the gel is referred to as colloidal (physical gel), while if the solid lattice is composed of macromolecules, the gel is called polymeric (chemical gel) **[1]**.

II.1.2. Principle

As depicted in Fig. II. 1, the sol-gel process is a highly versatile technique that allows for the precise production of a wide range of materials, including fibers, thin films, dense materials, powders, and ultra-low-density materials **[3]**.

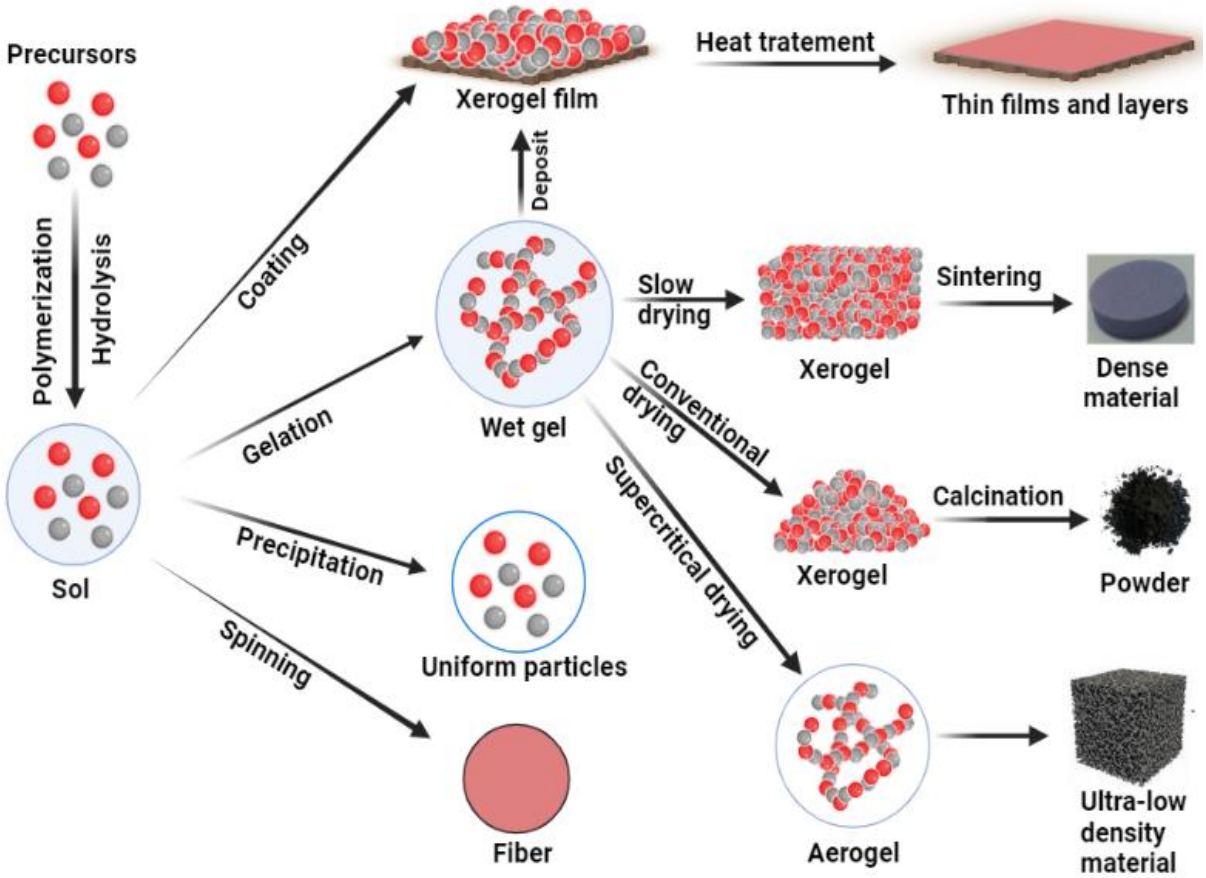

Fig. II. 1. Main steps of a material synthesis by the sol-gel process.

This versatility arises from the ability of the sol-gel process to enable precise control over the composition, microstructure, and morphology of the resulting material. For instance, the sol-gel process can be used to create thin films with precisely controlled thickness and exceptional adhesion to substrates, finding applications in fields such as microelectronics, optoelectronics, and sensors. Similarly, the sol-gel process can also be used to create fibers with controlled diameter and length, offering utility in the reinforcement of composites and

applications such as optical fibers. Furthermore, the sol-gel process can produce dense materials that have a uniform microstructure and excellent mechanical properties, making them useful in various applications like thermal barrier coatings, catalyst supports, and membranes. Additionally, powders produced by the sol-gel process have a narrow size distribution and controlled morphology, making them useful in several applications such as catalysis, sensing, and energy storage **[4]**.

The starting solution generally consists of a precursor, a solvent (usually an alcohol), sometimes a catalyst (acid or basic), and water. Each compound is dosed very precisely, as the properties of the gel depend on it. The selection of solvent and catalyst is then dictated by the chemical properties of the precursor, which is the central compound of the solution. Depending on the nature of the molecular precursor, two approaches are generally used in the sol-gel process **[5]**:

- Organometallic route: the precursors used are the molecular alkoxides M(OR)n where M designates a metal of valence n and R an alkyl chain of type ($-C_nH_{2n+1}$).
- Inorganic route: the precursors used are metal salts in aqueous solutions (nitrates, chlorides, ...), and complexing agents, such as citric acid, EDTA, maleic acid, sucrose, DEA, TEA, propionic acid, etc.

As shown in Fig. II. 2, the significant steps involved in the sol-gel synthesis are the followings **[6]**:

Hydrolysis; in which the reaction is initiated by mixing metal alkoxides with water in a solvent such as alcohol at ambient or slightly elevated temperatures. Acidic or basic catalysts

are used to expedite the polymerization process, leading to the condensation of adjacent molecules and the formation of metal oxide bonds while eliminating H_2O and ROH. As a result, the polymeric networks reach colloidal dimensions in the liquid state, also known as a "sol".

Gelation: the polymer networks combine to create a 3D structure in the liquid, resulting in a slightly rigid gel. The gel's pores trap solvents like water and alcohol. Over time, smaller polymer units aggregate into the main network, contributing to the gel's aging process.

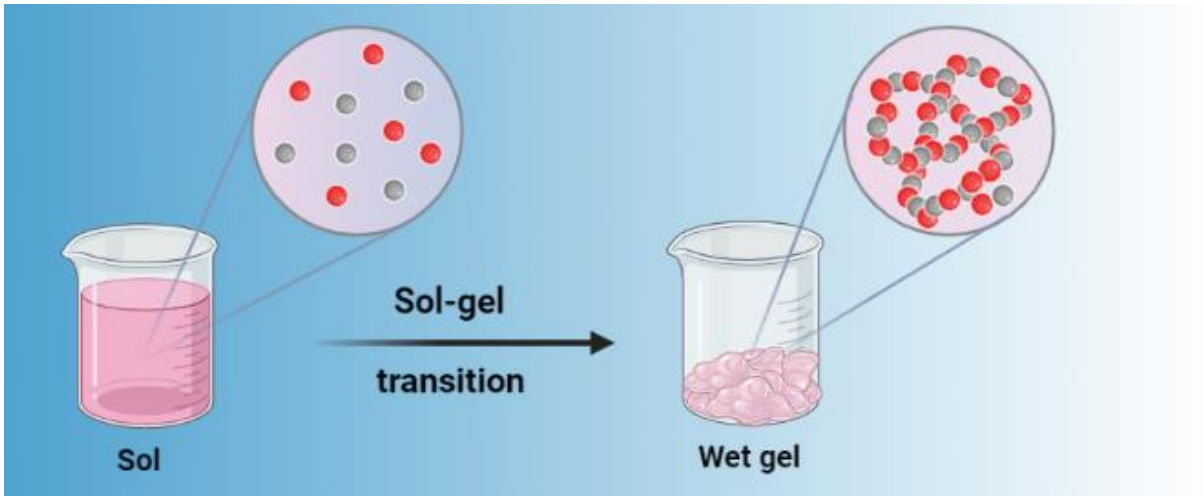

Fig. II. 2. Sol-gel transition.

The gels must be dried, i.e., subjected to an operation of solvent evacuation. As presented in Fig. II. 3, two types of dry gels can be distinguished **[7]**:

- Aerogel: the removal of the solvent is done by hypercritical evacuation, leading to a material of very low density .
- Xerogel: drying takes place by evaporation at atmospheric pressure to obtain a dense material or a powder.

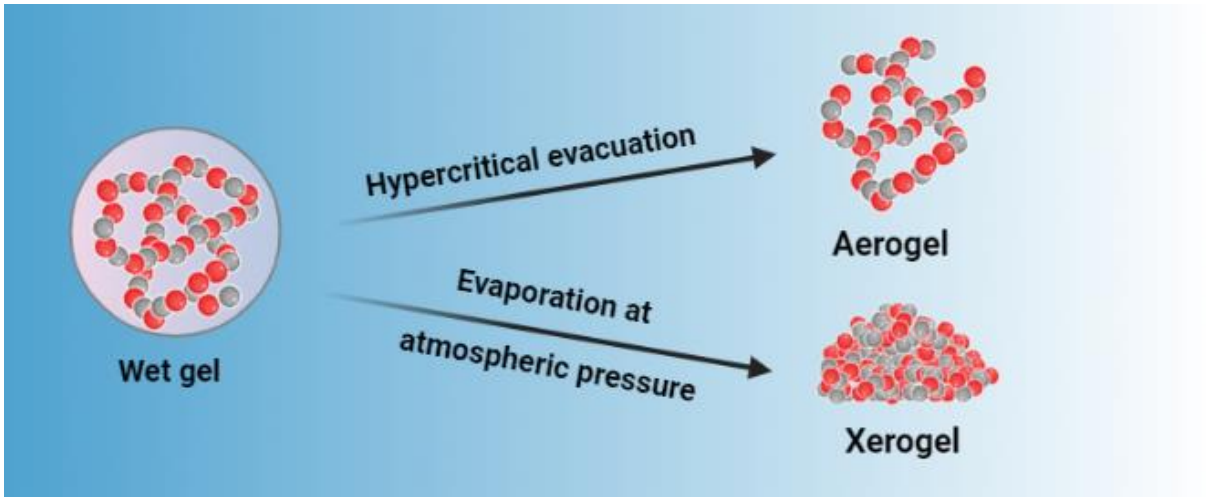

Fig. II. 3. Schematic drawing of the difference between xerogel and aerogel**.**

II.1.3. Factors influencing the reaction mechanisms

As in all other chemical technologies, the synthesis conditions influence the structure and properties of the products. Among the most preponderant parameters in sol-gel synthesis are the following **[8]**:

- **Composition and nature of precursors:** the choice of precursors in the sol-gel process has a significant influence on the characteristics of the end product. Precursor reactivity is a key factor, with highly reactive precursors resulting in a dense, highly cross-linked network structure. Precursor molecule size and shape can also impact the final material, with smaller molecules contributing to higher surface area and larger molecules producing bigger particles. Additionally, precursor composition plays a role, as the use of different metal alkoxides or salts can yield different metal oxides or mixed metal oxides, leading to distinct chemical and physical properties. Therefore, thoughtful selection of precursors is vital for achieving the desired material properties in the sol-gel process.
- **Solvent:** alkoxides are not miscible in water, so it is necessary to mix the precursors, water and possibly the catalyst, in a common solvent. It is then preferable to use the

alcohol corresponding to the –OR ligand of the alkoxide, in order to avoid possible reactions between the different components likely to modify the reaction kinetics.

- **Temperature:** as in all other types of synthesis, temperature has a considerable impact on the properties of the synthesized sol. It affects the rate, the mechanism, and the interaction of hydrolysis and condensation reactions. On the other hand, it also affects the vaporization of the solvent and consequently the substance concentration in the sol.
- **Surfactants:** Surfactants act by modifying the surface tension between the system components. Thus, they could serve as stabilizers of particles in the sol, firmly depressing the sedimentation process. Therefore, it is possible to achieve a homogeneous film and to modify the surface porosity and flexibility of the film found on the surface.

II.1.4. Sol-gel process advantages and disadvantages [9-11].

- Control of material porosity and nanoparticle size.
- Possibility of obtaining highly porous materials (dense, mesoporous, ultra-porous) in the form of thin film, fiber, and powder.
- Very high purity and homogeneity.
- Heat treatments required at low temperatures.
- Hydroxyl groups and carbonates remain after heat treatment.
- The duration of gel formation can vary from hours to days.
- High cost of precursors.
- Significant gel shrinkage during drying.

II.2. Physico-chemical characterizations

In order to determine the physico-chemical properties, the elaborated materials were characterized by means of differential thermal analysis and thermo-gravimetric, X-ray diffraction, Fourier transform infrared spectroscopy, X-ray photoelectron spectroscopy, scanning electron microscopy, energy-dispersive X-ray spectroscopy, laser particle size, and nitrogen adsorption-desorption analysis.

II.2.1. Differential thermal analysis and thermo-gravimetric (DTA-TG)

The TG analysis consists of measuring the variation of the material's weight as a function of temperature or time in a controlled atmosphere (air, Ar, N_2). This variation is a loss of weight in the case of decomposition or dehydration, it is a gain of weight in the case of oxidation or adsorption, and is null in the case of fusion or crystallization. The TG is usually coupled with DTA, which involves monitoring the temperature difference between the studied sample and a reference sample (thermally inert material). The measurement of this temperature difference allows the characterization of the endothermic and exothermic transformations of material **[6,12]**. During this thesis, DTA/TG analysis was carried out using SETARAM LABSYS Evo thermal analyzer in the range of 25-1000 °C with a heating rate of 10 °C.min^{-1} in the air.

II.2.2. X-ray diffraction (XRD)

X-ray diffraction is a common technique used to identify the structure, phase and atomic spacing of crystalline materials. As shown in Fig. II. 4, X-rays are scattered by the atoms of a crystal system as they pass through it. The scattered waves appear as spherical waves emitted from the atomic center. As the atoms are periodically aligned in the crystal,

there are fixed phase relationships between these spherical waves. Inevitably, the waves interfere constructively or destructively with each other, so that they are intensified in some directions and shifted in others, resulting in diffraction patterns. In other terms, the diffraction spots appear only in specific directions depending on the original incident line. This phenomenon can be described mathematically by Bragg's law:

$$2d \sin\theta = n\lambda \quad \text{..... (II.1)}$$

Where d is the distance between the diffracting planes, θ is the incident angle, n is an integer, and λ is the wavelength of the X-ray

The path length difference between two different X-rays can be determined as $2dsin\theta$, and the X-rays will interfere constructively when their path length difference is equal to an integral multiple of the wavelength. As the d-spacing varies in different crystals, the corresponding diffraction patterns will be different. From this point of view, it is possible to identify the phases of a sample by comparing the obtained diffractograms with the standards of the database in which all known species with their characteristics are indexed. However, materials with the same structure will have similar diffractograms **[13]**.

The characterization technique chosen in our case is X-ray powder diffraction. Initially, it allows us to verify, in the case of powders, the state of progress of the reaction and the purity of our materials. The final objective is the structural determination, i.e. the investigation of the atomic positions in the crystal lattice. In this thesis, the X-ray measurements were performed on a high flux Rigaku Ultima IV rotary anode X-ray diffractometer equipped with CuKα radiation source (λ = 1.542 Å). The diffraction angles (2θ) ranged between 15° and 82° and the crystalline phase identification is done by comparing

with the JCPDS (Joint Committee on Powder Diffraction Standards) with the use of Highscore Plus software.

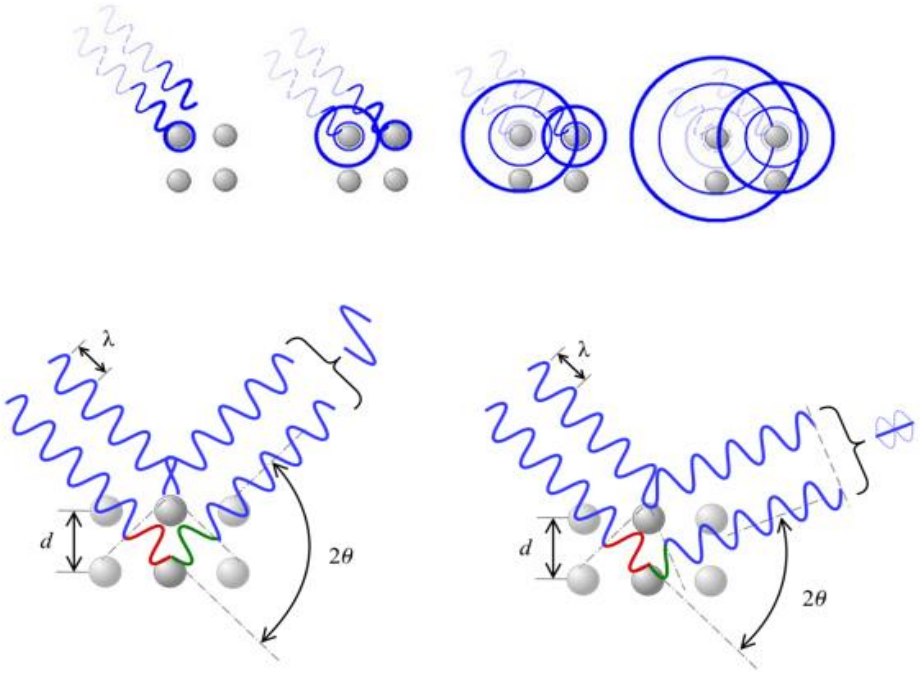

Fig. II. 4. X-ray diffraction principle.

II.2.3. Fourier transform infrared spectroscopy (FT-IR)

FT-IR spectroscopy is one of the most widely used absorption spectroscopic techniques which allows the identification of certain groups and gives structural information from their vibrational properties. As depicted in Fig. II. 5, the source of infrared radiation passes through a half-silvered mirror. Half of the signal is reflected and hits the second moving mirror. After reflection on the second mirror, the recombined IR signal will pass through the sample and will then be collected by the detector. Once a molecule is subjected to infrared radiation, it will vibrate or rotate. The vibrational energy can be classified into stretching and bending vibrations in which the stretching vibration occurs at a higher wavenumber than bending vibrations **[14]**.

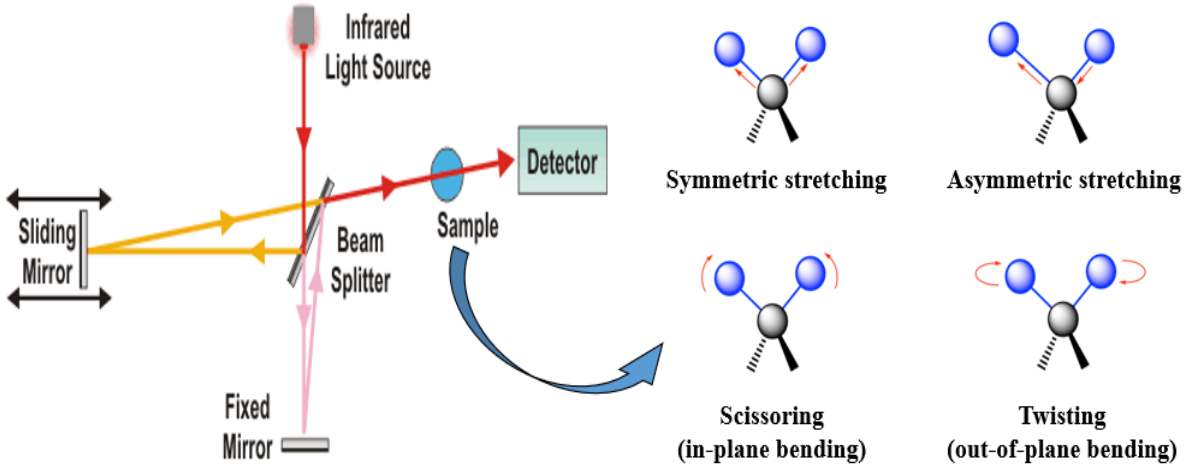

Fig. II. 5. Fourier transform infrared spectroscopy principle.

This technique measures the frequencies at which the sample absorbs radiation as well as the absorptions' intensity. It is known that chemical functional groups absorb radiation at characteristic frequencies. Therefore, the chemical structure can be determined from the recorded frequencies. In this thesis, the FT-IR spectra, for the synthesized samples, were conducted on an FT- IR PerkinElmer spectrometer across the range of 380 – 4000 cm^{-1} using the KBr pellet technique in which, a solid mixture of $LaCo_{1-x}Zn_xO_3$/KBr with a mass ratio of (1/99) was well ground and then pressed in a hydraulic press to form the pellets. The attribution of the bands to the different vibration modes is done by comparison with those reported in the literature.

II.2.4. X-ray photoelectron spectroscopy (XPS)

XPS is a technique that enables the description of the chemical compositions of the surface as well as their valence states. As shown in Fig. II. 6, it consists of irradiating the studied sample with a beam of X-ray photons that will ionize the surface atoms by means of the photoelectric effect. Part of the radiation energy (*hv*) is lost in the bond rupture (binding

energy) and the rest is given to the ripped-off electron in the form of kinetic energy (E_k). Photoelectron production only takes place if the energy of the incident photons is greater than the ionization potential of the core electrons in a given layer **[15]**.

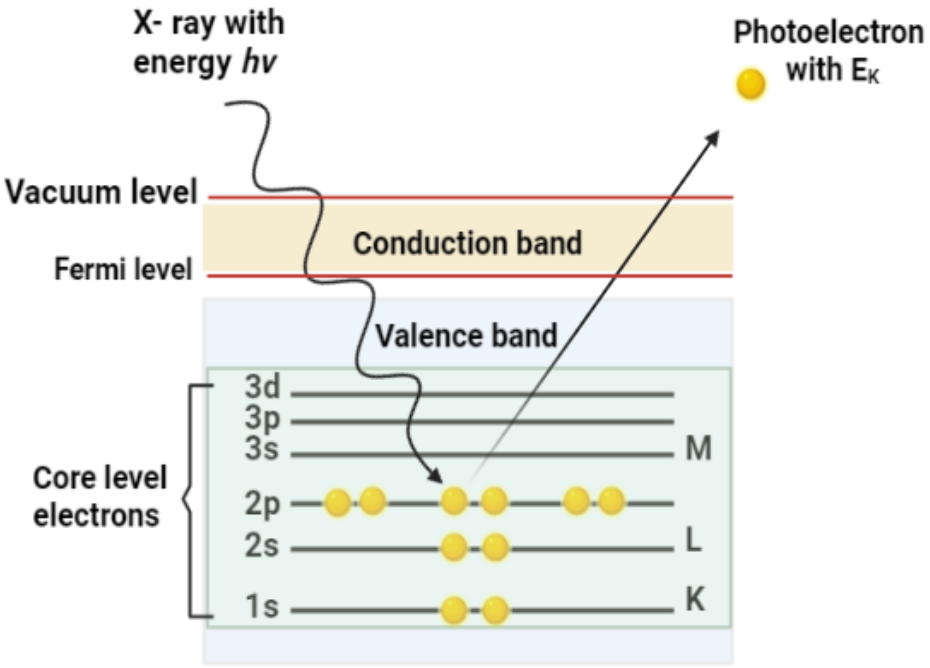

Fig. II. 6. X-ray photoelectron spectroscopy principle.

If we consider that the energy of the incident X-ray is *hv,* the kinetic energy that is recorded E_k, then it is possible to determine the binding energy (E_b) according to the following relation.

$$hv = E_K + E_B \quad \ldots\ldots\ldots\ldots\ldots\ldots \text{(II.2)}$$

This binding energy is characteristic of the atom considered, but also of its degree of oxidation, the type of binding in which it is engaged, its stoichiometry or its concentration. Therefore, by plotting the number of photoelectrons as a function of their binding energy it is quite possible to obtain information on the surface of the sample **[6]**.

In this thesis, the XPS experiments were performed on a Thermo Scientific ESCALAB 250 Xi^+ spectrometer with an Al Kα (1486.6 eV) monochromatic X-ray source at a base pressure of less than 5×10^{-10} mbar. the X-ray beam, focused to a diameter of 200 µm, was scanned over an area of 250 × 250 µm at an operating power of 40 W (15 kV). The photoelectron probing spectra were obtained using a hemispheric analyzer at pass energy of 200 eV with an energy step of 0.1 eV. The high-resolution spectra were recorded at a passing energy of 50 eV with the same energy step of 0.1 eV. All spectra were measured with a 90° angle between the X-ray source and the analyzer and without using low-energy electrons and argon ions for charge neutralization. After subtracting the Shirley background, the high-resolution spectra were deconvoluted into their components with mixed Gaussian-Lorentzian (30:70) line shapes using Casa XPS software.

II.2.5. Scanning electron microscopy (SEM)

SEM is a powerful technique used for the investigation of materials' surface morphology and composition analysis (when coupled with an EDS system). It involves using a very fine electron beam that scans the surface of the sample point by point. Indeed, the interaction of the electron beam with the sample surface creates or generates different particle emissions such as; secondary electrons, X-ray emissions, and backscattered electrons, which are then analyzed using appropriate detectors **[16]**.

As presented in Fig. II. 7, the secondary electrons are used for imaging. In fact, these electrons are very sensitive to the surrounding environment that images are made by collecting these types of electron through a detector formed by a scintillator coupled to a photomultiplier **[6]**.

II.2.6. Energy-dispersive X-ray spectroscopy (EDS)

EDS also known as EDX, or EDXA is a technique used to analyze the purity as well as the elemental compositions of a specimen. As presented in Fig. II. 7, the characteristic X-rays are generated after interactions of the incident primary electrons with the specimen. More precisely, a primary electron of energy E removes an electron from the inner shell (E_1) of an atom, leaving the atom in an excited energy state. An electron from the outer shell at the E_2 orbit will jump into this vacancy. Simultaneously, a photon of energy E_1-E_2 is released, which is known as the characteristic X-ray. The characteristic X-rays released are gathered and counted by energy difference, which is known as the EDX spectrum. As the energy difference corresponds to the specific electronic configuration of the atom, the specific elements present in the sample can be derived by comparing the signals to the elemental standards **[13]**.

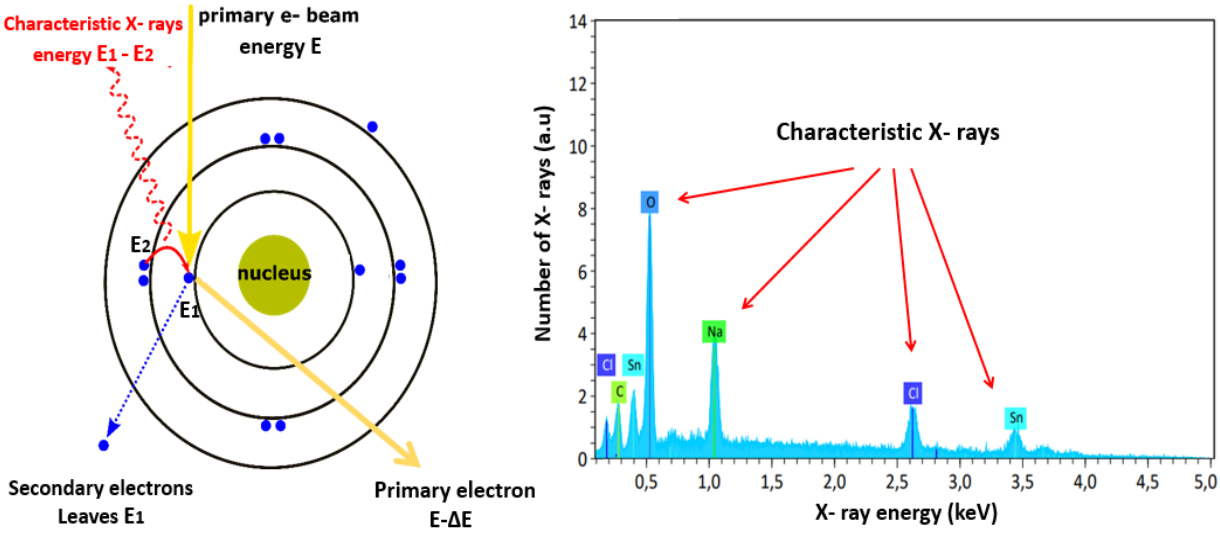

Fig. II. 7. Energy-dispersive X-ray spectroscopy principle.

In this thesis, A Joël JSM 7–7610F PLUS scanning electron microscope coupled to an EDS was used to study the morphology as well as to analyze the elemental compositions of the synthesized samples. The surface of non-conductive samples must be metalized because it

must be conductive to prevent the sample from charging. Therefore, the $LaCo_{1-x}Zn_xO_3$ samples are deposited on aluminum pads and then metalized by evaporation of silver under a secondary vacuum.

II.2.7. Laser particle size

Laser particle size is a technique used to determine the grain size of a powder and the statistical frequency of the different sizes in the sample (i.e. the particle size distribution). As illustrated in Fig. II. 8, this technique is based on the diffraction and diffusion principle of a laser beam, by measuring the angular variation in the intensity of the scattered light as a laser beam passes through a sample of dispersed particles. Large particles will scatter light at small angles to the laser beam and small particles at larger angles. The angle-dependent scattered intensity data is analyzed to calculate the size of the particles that created the diffraction pattern. Two models are used depending on the particle size: for large particles, the Fraunhofer theory (diffraction by the particle's contours) is applicable. For smaller particles, the Mie theory should be used, which takes into account diffusion, absorption, and diffraction phenomena **[17]**.

During this thesis, particle size distribution analysis was assessed using a laser particle size analyzer (HORIBA LA-950). The powders are first dispersed in distilled water and ultrasound to avoid the formation of clusters. Afterward, a sufficient quantity of the solution is taken and introduced into the cell. During the measurement, the powders are dispersed in a sampling module equipped with an ultrasonic probe, a circulation drives the powder in suspension in the optical cell through which the laser beam passes, in which the optical properties of the powders and those of the solvents should be known (the refractive index of

$LaCoO_3$ is 3.04 and that of water is 1.33).

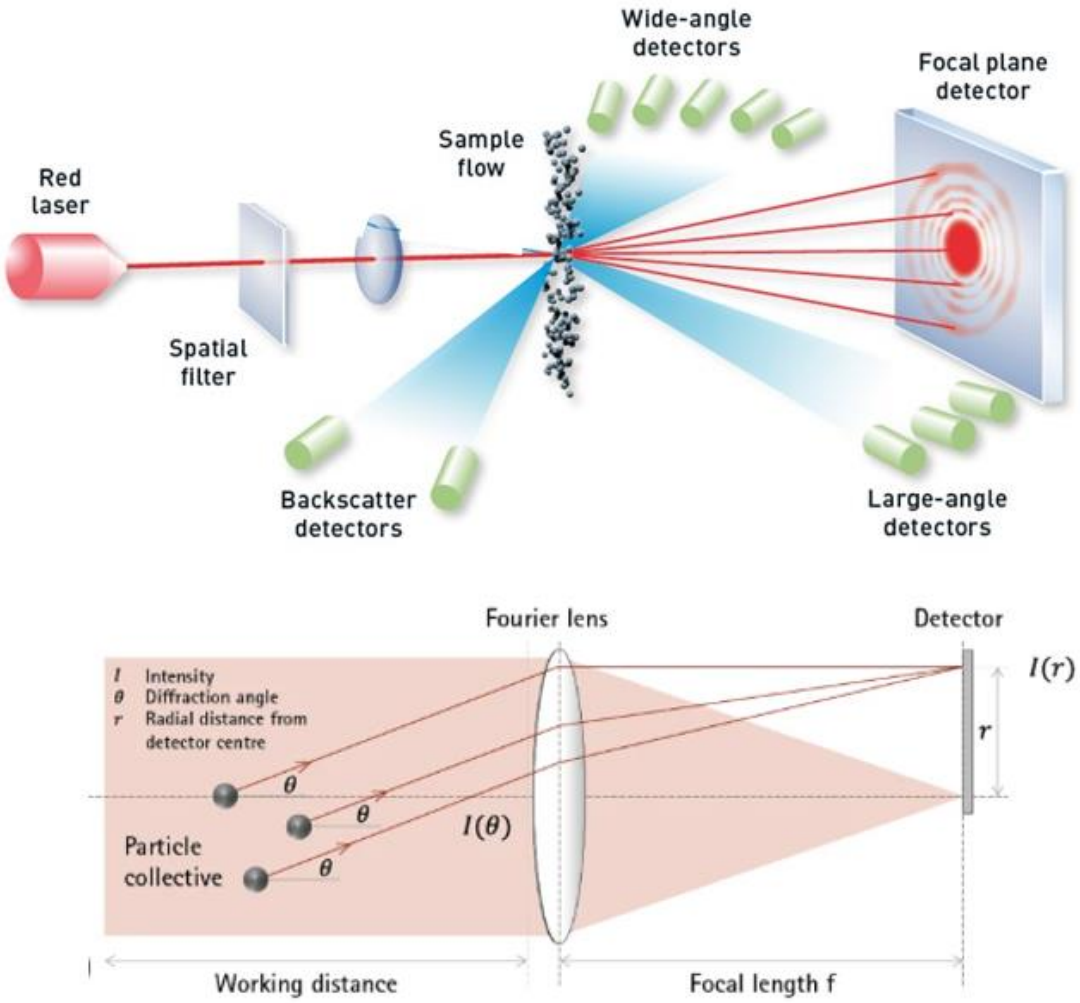

Fig. II. 8. Laser particle size principle.

II.2.8. Nitrogen adsorption-desorption

Nitrogen adsorption-desorption is a technique used to further characterize the surface texture of the porous media. First, the adsorption is a surface phenomenon which corresponds to the fixation of molecules (adsorbate) on the surface of a solid (adsorbent). Two adsorption mechanisms exist: physisorption, which is a reversible phenomenon characterized by weak Van der Waals-type forces, and chemisorption, which is an irreversible process involving the formation of a covalent chemical bond. The shape of the adsorption-desorption isotherms

depends on the adsorbate, the adsorbent, and the interactions between the gas and the solid surface **[18]**.

According to the International Union of Pure and Applied Chemistry (IUPAC) classification, six types of isotherms are used to characterize the porosity of the investigated medium (Fig. II. 9).

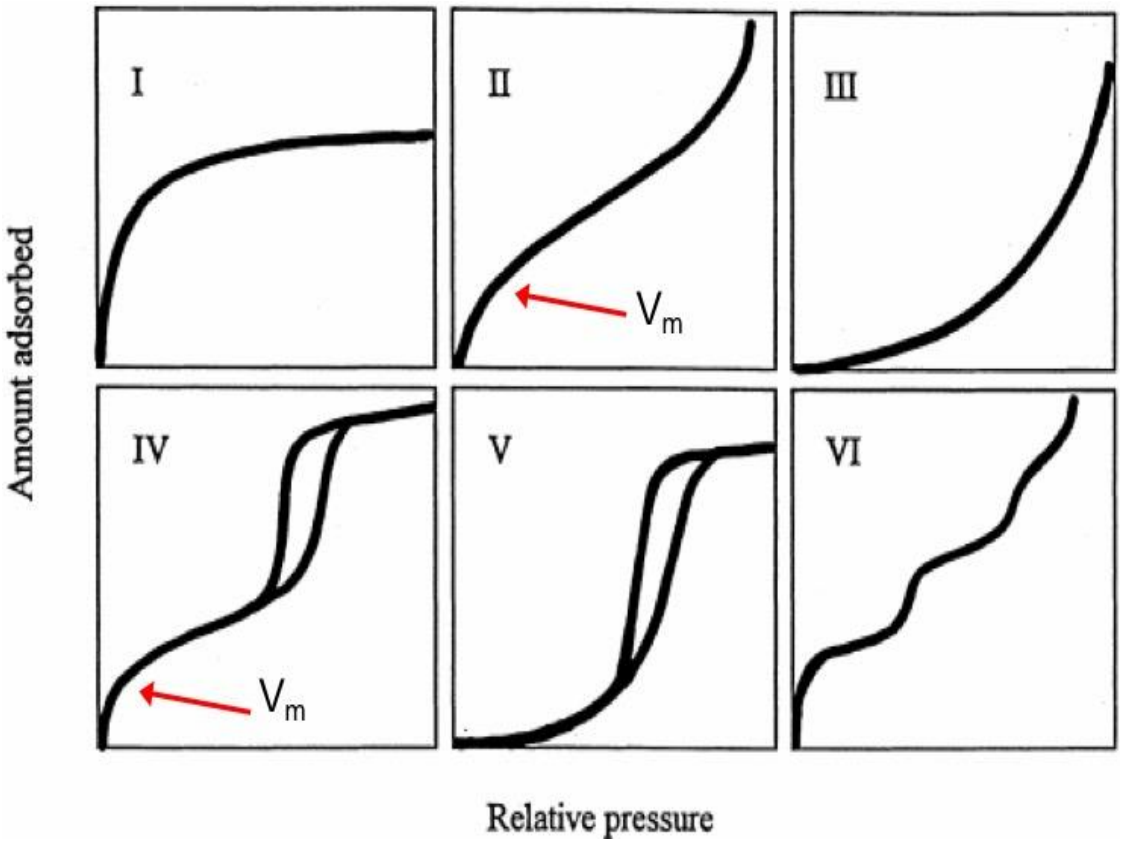

Fig. II. 9. Types of physisorption isotherms.

The type **I** adsorption isotherm is obtained with purely microporous adsorbents which fill at lower relative pressures as the pore size is smaller. The type **II** adsorption isotherm is characteristic of multi-molecular adsorption. The type **IV** adsorption isotherm shows a similar pattern to that of type **II** for low relative pressures. Nevertheless, for the highest relative

pressures, it is characterized by a saturation plateau whose length is very variable: this adsorption isotherm is obtained with mesoporous adsorbents in which capillary condensation occurs in the mesopores at high P/P_0 values. Desorption of capillary condensed nitrogen in the mesopores is not reversible and hysteresis is generally observed on desorption. Type **III** and **V** adsorption isotherms are significantly rarer. The inversion of curvature at the start of the adsorption isotherm characterizes a weak adsorbent/adsorbate interaction. This type of isotherm is for example observed in the case of water vapor adsorption on a hydrophobic surface. The type **VI** step adsorption isotherm is only seen in the case of adsorption by energetically homogenous surfaces on which the layers are formed one after the other **[18]**.

The treatment of nitrogen adsorption-desorption isotherms gives access to certain parameters, including the specific surface area, which defines the total surface area per unit of mass accessible to atoms and molecules. The BET method (Brunauer, Emmett, and Teller) is undoubtedly the most widely used to determine the value of the specific surface area. The pore distribution such as pore diameter and pore volume is obtained by the BJH (Barrett, Joyner, Halenda) treatment of the desorption branch of the isotherm.

In this thesis, the specific surface area, the pores' volume and diameter were measured by the Nitrogen adsorption-desorption technique using a physisorption analyzer (Micromeritics ASAP 2010). The texture parameters are identified at the nitrogen liquefaction temperature (77K), the samples having been previously degassed at 723 K for 4 hours (in order to remove all traces of water and CO_2).

II.3. Electrochemical measurements

II.3.1. Experimental apparatus

The electrochemical properties of the LCZ materials with different (x) contents were carried out on an AUTO LAB-AUT85204 electrochemical workstation assisted by a computer and equipped with software (Nova 2) that allows both, the setting of the operating parameters and the selection of the targeted electrochemical technique, such as the linear sweep voltammetry (LSV), Tafel polarization, electrochemical impedance spectroscopy (EIS), chronopotentiometry (CA), cyclic voltammetry (CV), and galvanostatic charge-discharge (GCD). To study the effect of zinc doping on the electrochemical performances either for the oxygen evolution reaction or for the supercapacitor application, we used a conventional three-electrode electrochemical cell consisting of LCZ materials, platinum, Ag/AgCl (3 M KCl), and 1M KOH serving respectively as the working electrode, counter electrode, reference electrode, and the electrolyte solution. The electrochemical setup used is shown in Fig. II. 10.

The electrochemical performance of assembled hybrid supercapacitor was realized in a two-electrode system composed of the LCZ 05 as a positive electrode (anode) and activated carbon (AC) as a negative electrode (cathode) in 1M KOH electrolyte solution.

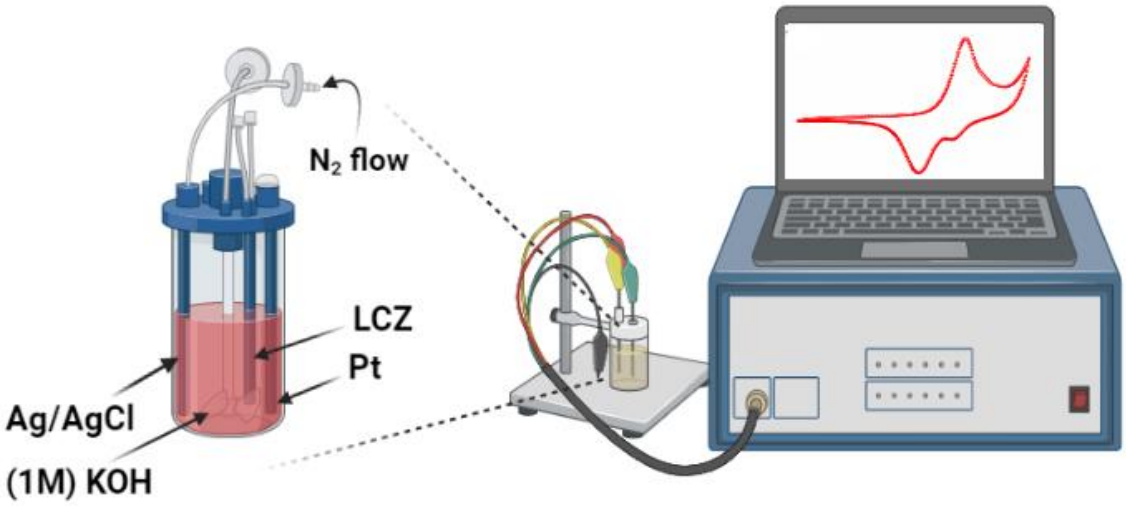

Fig. II. 10. Experimental setup used for the electrochemical measurements.

II.3.2. Experimental techniques

II.3.2.1. Linear Sweep Voltammetry (LSV)

Linear sweep voltammetry (LSV) is an electrochemical method used to measure the reactivity of a chemical species in a solution. As shown in Fig. II. 11, It consists of applying a sweep potential varying linearly with time between two predetermined potential limits E_i and E_λ (input signal) to an electrode immersed in an electrolyte and measuring the current-voltage response (output signal), thereby enabling the identification of electrochemical reactions occurring at the electrode/electrolyte interface. A typical response curve of the LSV is given in Fig. II. 11b . If the scan starts, only the non-faradic (capacitive) current circulate for a period of time. When the potential of the electrode reaches the proximity of E°, the oxidation reaction starts and the anodic current begins to flow. As the potential becomes more positive, the concentration of the electroactive species at the surface must reduce; therefore, the flux towards the surface as well as the current will increase. As the potential rises above E°, the

concentration of the electroactive species at the surface drops to almost zero, the mass transfer to the surface achieves a maximum rate, then it decreases as the effect of depletion sets in. The result is a current-potential curve with a peak like the one shown **[19]**.

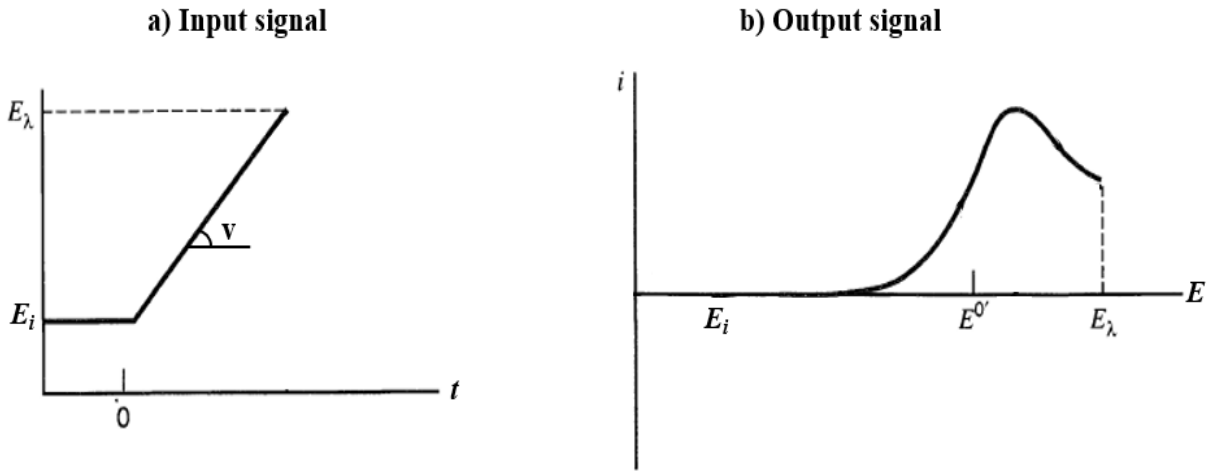

Fig. II. 11. linear sweep voltammetry principle.

These polarization measurements also enable the determination of the reaction kinetic parameters such as the exchange current density and the limit step of the reaction mechanism through the estimation of the Tafel slopes, as shown in Fig. II. 12. In the present work, a procedure was developed to evaluate the overpotential phenomena and the kinetic parameters of the oxygen evolution reaction for each electrocatalyst. The measurements were conducted between 1.05 and 1.73 (V vs RHE) in N_2-saturated 1M KOH at a sweep rate of 10 $mV.s^{-1}$. This upper limit of potential was chosen in order to avoid any disturbances due to the formation of oxygen bubbles and the catalysts that they might cause **[6]**.

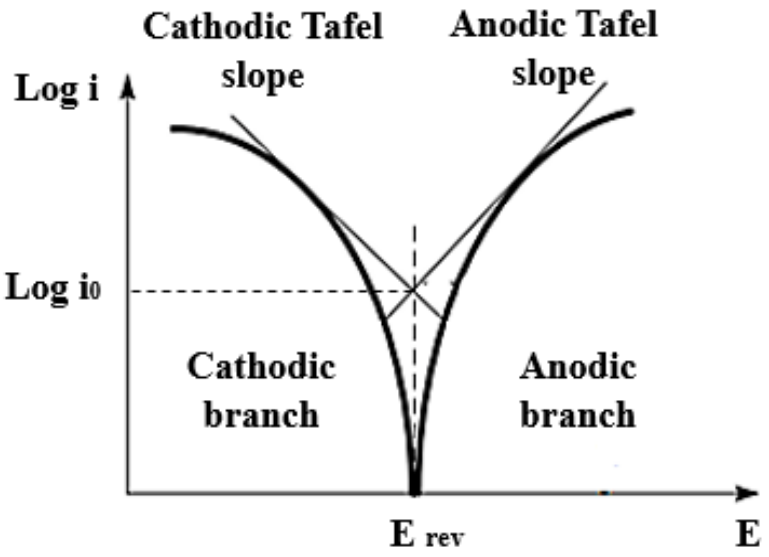

Fig. II. 12. Schematic representation of a Tafel curve enabling the determination of the exchange current density and the Tafel slope.

II.3.2.2. Electrochemical Impedance Spectroscopy (EIS)

EIS is a technique that provides information about the charge transport properties within electrode materials as well as the electrochemical phenomena occurring at the electrode-electrolyte interfaces. It consists in applying a periodic perturbation by means of an alternating voltage or current with low amplitude depending on its frequency (generally over the range of kHz and mHz) and studying the way the excited electrochemical system responds to this perturbation (Fig. II. 13b and c). The electrochemical impedance spectroscopy measurements are frequently represented in the form of Nyquist and/or Bode representations (Fig. II. 13d), which can be correlated with an equivalent electrical circuit (Fig. II. 13e), whereby a mechanistic interpretation of the studied system is used to infer the electrochemical parameters such as the internal resistance R_e, charge transfer resistance Z_F, double layer capacitance CPE_{dl}, and so on **[20]**.

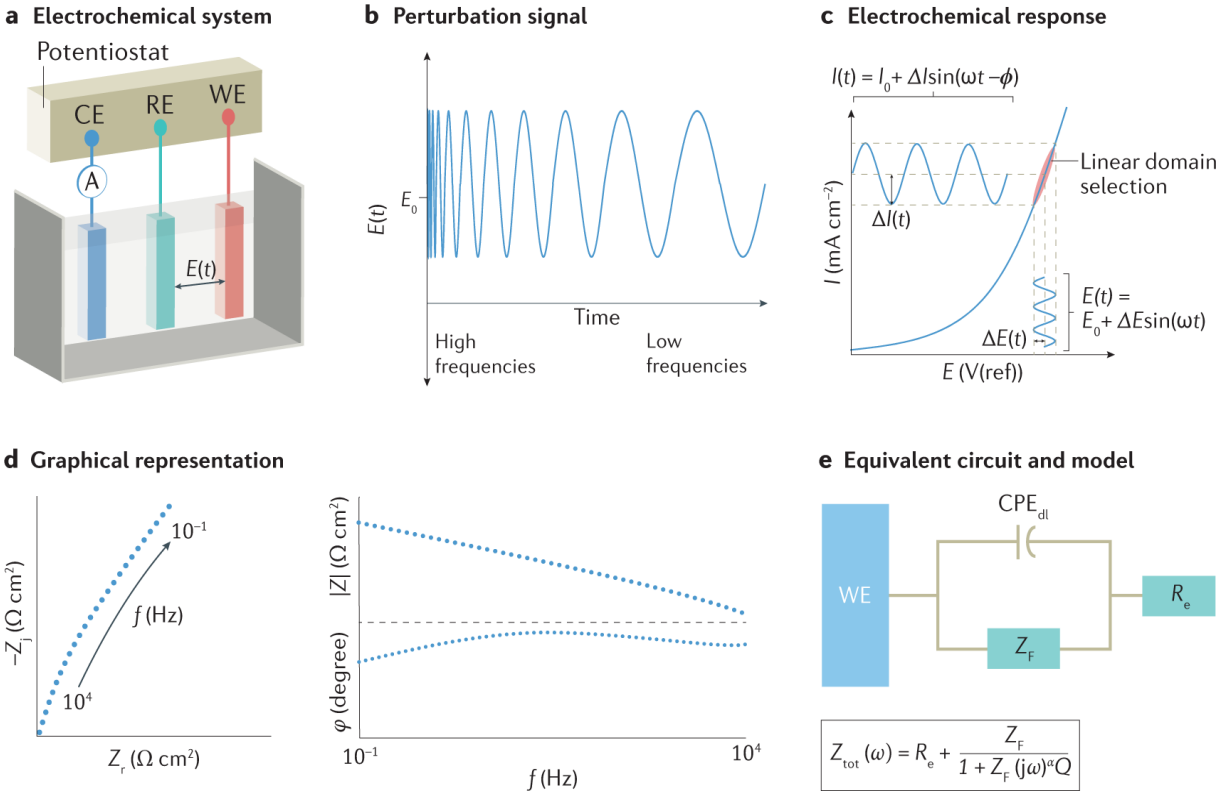

Fig. II. 13. The electrochemical impedance spectroscopy principle.

The conditions of the measurements conducted during this thesis are the following; the imposed amplitude is 10 mV and 50 frequencies with five sines distributed uniformly in a logarithmic way over the range of 100 kHz and 10 mHz. The applied potentials for the oxygen evolution reaction application are the potentials corresponding to the current density of 10 mA.cm^{-2}, while for the supercapacitor application they are the open circuit potentials.

II.3.2.3. Chronopotentiometry (CP)

The chronopotentiometry method consists of applying a constant current density (input signal (Fig. II. 14a) and measuring the variation of the potential between the working and reference electrodes as a function of time (output signal (Fig. II. 14b)). This variation depends

on the concentration change of the studied species within the working electrode **[21]**. In general terms, the CP method is usually used to evaluate the number of electrochemical reactions occurring at the working electrode, where each observed plateau is related to an electrochemical process. Beyond the plateau, the flow of the electrolyzed substance to the electrode is insufficient to consume all the imposed current, so a potential jump occurs to reach a value such that another electrochemical reaction can take place and consume all the imposed current **[22]**. In our case, the CP method is employed to study the durability of the prepared electrocatalysts, i.e., how much potential should be applied to achieve the same current density during their use. So we applied a current density of 10 $mA.cm^{-2}$ over 24 hrs.

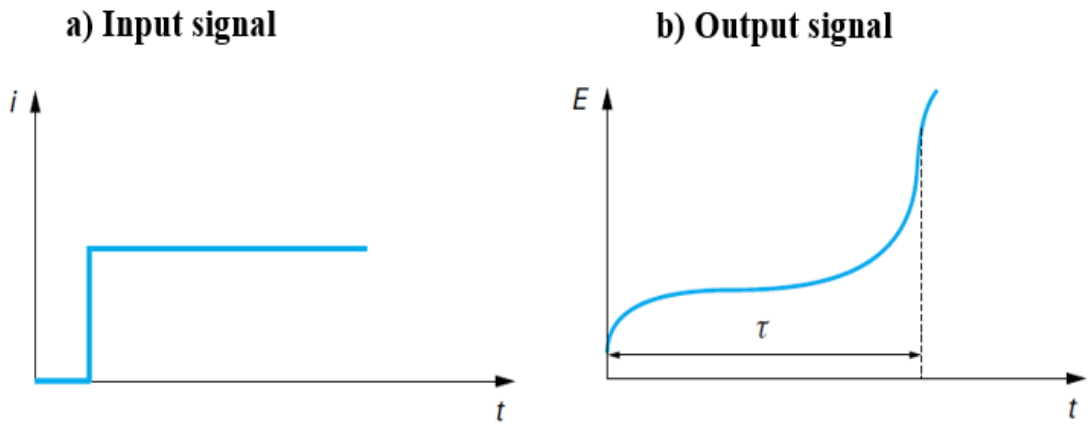

Fig. II. 14. The chronopotentiometry principle.

II.3.2.4. Cyclic voltammetry (CV)

Cyclic voltammetry became a well-known technique for preliminary electrochemical studies of novel systems and proved to be very useful for obtaining information on rather complicated electrode reactions as well as on phenomena occurring at the electrode/electrolyte interface. In brief, it consists of applying a forward scan of potential

from E_i to E_λ followed by a backward scan to the initial potential E_i at constant speed v (Fig. II. 15a), where a complete forward-backward scan of the potential applied at the same scan rate is called a cycle **[23]**.

A typical response curve of the CV is given in Fig. II. 15b. The forward scan from E_i to E_λ is discussed in details in the LSV above. If we switch the potential scan from E_λ to E_i (backward scan) there is a high concentration of the oxidized species in the vicinity of the electrode. As the potential nears and then exceeds E°, the electrochemical balance at the electrode surface becomes increasingly favorable to the neutral species. Thus, the oxidized ions become reduced and a cathodic current circulates. This inversion current will have a very similar form to the forward scan for the same reasons as discussed in the LSV method **[19]**.

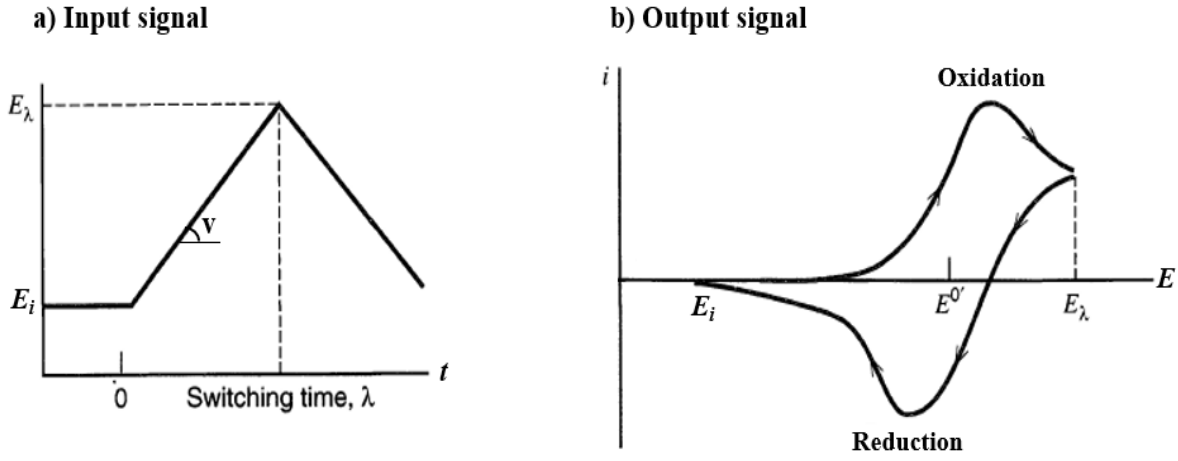

Fig. II. 15. Cyclic voltammetry principle.

The resulting CV curve can provide useful information about the electrode reaction process, such as the reversibility of the electrode reactions, rate capability, polarization and the electrochemical storage mechanism, and also enables the evaluation of capacitances by using the following Eq. (**II.3**) **[24]**.

$$C_s = \frac{\int_{V_i}^{V_f} I(V)dV}{2.m.v.\Delta V} \quad \ldots\ldots\ldots\ldots\ldots\ldots\ldots\ldots\ldots\ldots (II.3)$$

where C_s (F/g) is the specific capacitances and m (g) the active material mass. For the assembled supercapacitor m is the overall weight of both negative and positive electrode active materials, V_i and V_f (V) are the initial and final potentials, v (V. s^{-1}) is the sweep rate, I (A) the specific current, ΔV (V) the potential working window.

In the work presented in this thesis, the CV measurements are recorded at several sweep rates ranging from 2 to 100 mV.s-1 over a potential working window of -0.05 to 0.45V (for the three-electrode system) and 0 to 1.5V (for the two-electrode system).

II.3.2.5. Galvanostatic charge and discharge (GCD)

GCD is a significant method for studying the electrochemical energy storage performance of the electrode materials. A consecutive charge-discharge of the working electrode is performed at a constant current density (input signal (Fig. II. 16a)) over a potential window with or without a rest period (a period of time between the charge and discharge process, while the peak voltage V_0 remains constant). Moreover, the charge-discharge measurements at different current densities can be also used to study the rate performance of the electrode materials. Based on the GCD curve (output signal (Fig. II. 16b), we can obtain the charge and discharge times. Therefore, the specific capacitance (C_s) of the active material can be calculated according to the following equation (**II.4**) **[25]**:

$$C_s = \frac{I.\Delta t}{m.\Delta V} \ldots\ldots\ldots\ldots\ldots (II.4)$$

where C_s (F/g) is the specific capacitance, I (A); the applied current density, Δt (s); the discharge time, m (g); the active material mass, and ΔV (V) is the potential chosen working window.

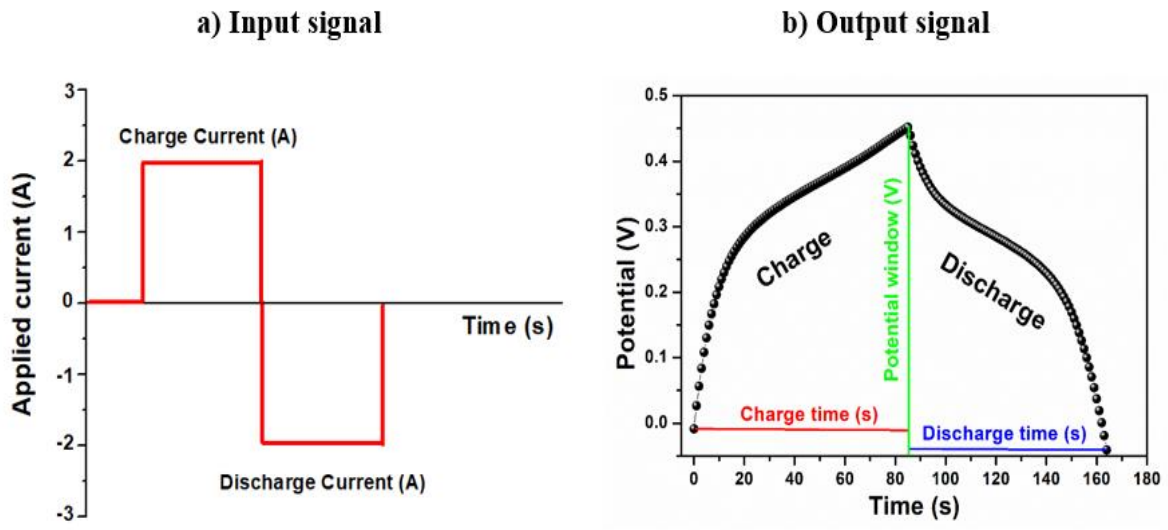

Fig. II. 16. The galvanostatic charge and discharge principle.

Another important aspect of SCs is their cycle stability. In the laboratory, 1,000 to 10,000 charge-discharge cycles are preferably performed to study the potential durability of the cycle, where a cycle is equivalent to a charging and discharging process at a constant current density. Extended cycling typically deteriorates the electrodes and induces corrosion in the constituents of a cell, resulting in a performance loss. To get an idea of how the material will perform in real SCs, initial and final performances are compared and analyzed **[13]**.

The energy density (E) and the corresponding power density (P) of SCs are also preponderant factors to study their practical application. Based on the calculated specific capacitance from the GCD, the E and P values of the device can be calculated. The formulas used to determine E and P, respectively, are as follows **[26]**:

$$E = \frac{C_s.(\Delta V)^2}{2 \times 3.6} \dots\dots\dots\dots\dots\dots (II.5)$$

$$P = \frac{3600.\mathrm{E}}{\Delta t} \dots\dots\dots\dots\dots\dots\dots (II.6)$$

where E ($Wh.kg^{-1}$) and P ($W.kg^{-1}$) are, respectively, the energy and the corresponding power densities, ΔV (V) the potential working window, and Δt (s) the discharge time.

The conditions of the measurements carried out during this thesis are the following;

- The three electrode system; the applied current densities are 0.5, 1, 2, 3, 4, and 5 A/g over the potential window of -0.05 to0.45V without a rest period. For the cycle stability, we have conducted 5000 successive charge and discharge cycles between -0.05 and 0.45V at a constant current density (5 A/g),
- The two electrode system; the applied current densities are 0.5, 1, 2, and 3 A/g over the potential window of 0 to 1.5V without a rest period. For the cycle stability, we have conducted 5000 successive charge and discharge cycles between 0 and 1.5V at a constant current density (3 A/g).

References

[1] P. C. Hiemenz, Principles of colloid and Surface Chemistry Marcel Decker, New-York, 1997.

[2] H. B. Weiser, A textbook of colloid Chemistry, Wiley, New-York, p. 2-4, 1949.

[3] M. Keshmiri, T. Troczynski, M. Mohseni, Oxidation of gas phase trichloroethylene and toluene using composite sol–gel TiO_2 photocatalytic coatings, J. Hazard. Mater. 128 (2006) 130-137.

[4] M. Barczak, C. M. Donagh, D. Wencel, Micro- and nanostructured sol-gel-based materials for optical chemical sensing (2005–2015), Microchim. Acta. 183 (2016) 2085–2109.

[5] Schubert, U. Chemistry and Fundamentals of the Sol–Gel Process. In The Sol-Gel Handbook; John Wiley & Sons, Ltd.: Hoboken, NJ, USA, 2015; pp. 1–28.

[6] E. Omari, Doctoral thesis, University of Mohamed Khider Biskra (2021).

[7] H. Tüysüz, F. Schüth, Ordered Mesoporous Materials as Catalysts, Adv. Catal., 55 (2012) 127-239.

[8] C. Colleoni, Doctoral thesis, University of Bergamo (2012).

[9] C. B. Carter, M. G. Norton, Sols, Gels, and Organic Chemistry. In: Ceramic Materials. Springer, New York, NY, 2007, 400-411.

[10] D, Navas, S. Fuentes, A. C. Alvarez, E. C. Angel. Review on Sol-Gel Synthesis of Perovskite and Oxide Nanomaterials. Gels, 7 (2021) 275.

[11] C. R. Cho, Prof. Dr. M. S. Jang, Prog. Dr. S. Y. Jeong, Y. B. Kim, Ferroelectric PbTiO3 Powders and Thin Films Derived from Sol-Gel Processing, Cryst. Res. Technol. 28 (1993) 1085-1092.

[12] P. J. Palermo, Solid Dosage-Form Analysis. In: Ahuja S, Scypinski S (eds.) Sep Sci Technol, 3 (2001) 235–267.

[13] M. Abdelkader, Doctoral thesis, University of Science and Technology HOUARI BOUMEDIENE (2021).

[14] Y. Duan. Understanding the oxygen evolution reaction(OER) for Co based transition metal oxides / hydroxides in alkaline electrolytes. Material chemistry. Sorbonne University; Nanyang Technological, Singapore University (2021).

[15] D. Son, S. Cho, J. Nam, H. Lee, M. Kim, X-Ray-Based Spectroscopic Techniques for Characterization of Polymer Nanocomposite Materials at a Molecular Level. Polymers 12 (2020) 1053.

[16] F. Hidayanti, A. A. Harnovan, Application of scanning electron microscopy: a review, International Journal of Applied Science and Engineering Review (IJASER) 1 (2020) 91-102.

[17] M. Lebid, Doctoral thesis, University of Mohamed Khider Biskra (2016).

[18] K.S. Sing, Reporting physisorption data for gas/solid systems with special reference to the determination of surface area and porosity (Recommendations 1984), Pure Appl. Chem. 57 (1985) 603-619.

[19] A.J. Bard, L.R. Faulkner, Electrochemical Methods: Fundamentals and Applications (second ed.), Wiley, New York (2000).

[20] S. Wang, J. Zhang, O, Gharbi, V. Vivier, M. GaO, M. E. Orazem, Electrochemical impedance spectroscopy, Nat Rev Methods Primers 1, 41 (2021).

[21] S. Abdelfetteh, Doctoral thesis, University of Ferhat Abbas Setif-1 (2018).

[22] G. Picard, F. Chouaib, S. Sanchez, Chronopotentiométrie, Techniques de l'Ingénieur, P

2175 1-20.

[23] N. Madoui, Doctoral thesis, University of Mohamed Khider Biskra (2017).

[24] J. Xie, P. Yang, Y. Wang, T. Qi, Y. Lei, C.M. Li, Puzzles and confusions in supercapacitor and battery: Theory and solutions, J. Power Sources 401 (2018) 213-223.

[25] C.I. Priyadharsini, G. Marimuthu, T. Pazhanivel, P. Anbarasan, V. Aroulmoji, S. Prabhu, R. Ramesh, Electrochemical supercapacitor studies of Ni^{2+}-doped $SrTiO_3$ nanoparticles by a ball milling method, Ionics 26 (2020) 3591-3597.

[26] B. Zhang, C. Yu, Z. Li, Enhancing the Electrochemical Properties of $LaCoO_3$ by Sr-Doping, rGO-Compounding with Rational Design for Energy Storage Device, Nanoscale Res. Lett. 15 (2020) 1-13.

Chapter III:

Synthesis and electrocatalytic properties of zinc doping lanthanum cobaltite perovskite as an electrocatalyst for the oxygen evolution reaction

Chapter III: Synthesis and electrocatalytic properties of zinc doping lanthanum cobaltite perovskite as an electrocatalyst for the oxygen evolution reaction

III.1. Introduction

The rapid increase in global energy requirements and the environmental pollution resulting from the consumption of fossil resources, have caused researchers to look at the transition to sustainable and renewable energy sources, which is deemed as a promising and perhaps inevitable solution to overcome these crises **[1-3]**. As a result, water splitting for the production of H_2 and O_2 has emerged as an efficient and promising way for energy storage and conversion, in addition to being simple and environmentally friendly **[4-6]**. The oxygen evolution reaction (OER) at the anode is usually slower than the hydrogen evolution reaction (HER) at the cathode **[7]**. In particular, the kinetics of OER is hindered due to the complex process of four-electron oxidation at the anode catalyst, and thus require a large overpotential, which could restrict the overall efficiency of water electrolysis **[8]**. Nevertheless, the slower kinetics and the large energy barrier make it necessary to develop high-performance catalysts to hasten the reaction and to overcome this stalemate **[9]**. Oxides of ruthenium and iridium (RuO_2, IrO_2) are regarded to be the leading-edge for OER electrocatalysts in light of their best catalytic activity. Unfortunately, the low stability, scarcity, and high costs have severely hampered their widespread application **[10]**.

Perovskite-type oxides (ABO_3) are anticipated to be one of the most promising alternate catalysts for the OER based on their structural and compositional flexibility **[11]**, high catalytic activity and stability **[12]**, in addition to low cost **[13]**. Numerous studies have been devoted on using perovskites as a catalyst, among these, $LaCoO_3$ has been known as an active and durable OER electrocatalyst in a basic medium **[14, 15]**. Moreover, the partial

introduction of appropriate cations into the A or/and B sites will produce oxygen vacant sites, which results in an alteration in the transition metal valence states. This can enhance considerably their catalytic activity (i.e., reducing the overpotential) **[16]**. Evidence can be found in preceding reports. For example, M. E. Hilal et al **[17]** investigate the substitution of both A and B sites with Ca and Mn in $LaCoO_3$ generating the creation of oxygen vacancy in the material bulk, thus significantly enhances the OER activity. Likewise, K. Li et al. **[18]** studied the co-doping effect of Sr and Mn into $PrFeO_{3-\delta}$ in which the $Pr_{0.6}Sr_{0.4}FeO_{3-\delta}$ electrocatalyst displays the best OER activity with an overpotential value of merely 400 mV compared to the other composition. Furthermore, M.A. Ghanem et al. **[19]** demonstrate that the partial replacement of cobalt by 30 % of rhodium into the $LaCoO_3$ crystal lattice promotes the OER activity with 300 mV overpotential. Similarly, B. Bao and coworkers reduce the overpotential up to 310 mV by incorporating 25 % of iron into $LaCoO_3$ **[20]**. Identically, 50 % Pr-doped $LaCoO_3$ decreases the overpotential from 371 to 312 mV **[21]** and 20 % V-doped $LaCoO_3$ reduces the overpotential value from 407 to 306 mV **[22]**.

Zinc has been introduced into various kinds of materials as a dopant because of its capability to generate extrinsic defects **[23]**, in addition to its pivotal role in boosting the OER activity. For example, O. Elies et al. **[24]** found that the OER activity was enhanced by substituting iron with zinc in the $LaFe_{1-x}Zn_xO_3$, and the highest OER activity is achieved at x = 0.1. Likewise, J. Wu and colleagues confirmed that the overpotential was diminished to 248 mV just by introducing zinc into CoS_2 Nanoarrays **[25]**. Also, $MnCo_2O_4$ doped with zinc enhanced considerably the electrocatalytic performance by narrowing the overpotential by 48

mV compared to the pristine one **[26]**. Furthermore, a superior electrocatalytic activity with a significantly reduced overpotential of 221 mV was achieved when zinc is incorporated into cobalt-iron LDH Arrays **[27]**.

In the present chapter, zinc-doped lanthanum cobaltite $LaCo_{1-x}Zn_xO_3$ with x = 0, 0.1, 0.2, 0.3 and 0.4, denoted as LCZ 00, LCZ 10, LCZ 20, LCZ 30 and LCZ 40, respectively, were prepared using the sol-gel method and characterized by TGA/DTA, XRD, FTIR, XPS, SEM, laser diffraction granulometry and the N_2 adsorption-desorption. The electrocatalytic performance toward the OER of the elaborated electrocatalysts was examined in alkaline media, by means of linear sweep voltammetry, anodic Tafel polarization, electrochemical impedance spectroscopy, and electrochemical stability tests by using chronopotentiometry.

III.2. Experimental

III.2.1. Elaboration of LCZ electrocatalysts

The sol-gel technique was used to prepare a series of $LaCo_{1-x}Zn_xO_3$ perovskite with (x = 0, 0.03, 0.05 and 0.1) using $Co(NO_3)_2.6\ H_2O$, $La(NO_3)_3.6\ H_2O$, and $Zn(NO_3)_2.6\ H_2O$ as raw materials and citric acid (CA) as a chelating agent. As depicted in Fig. III. 1, metal nitrates were dissolved in ethanol separately, whereas the CA was added dropwise to the combined solution in a molar ratio of 1:1:2 (lanthanum: cobalt–zinc: citric acid). The blended solution was heated at about 80 °C under vigorous magnetic stirring until a purple translucent gel was formed. Afterward, the as-prepared gel was dried at around 100 °C in the air for 24 hrs. Then the obtained dry powder was ground by a mortar and calcined at different calcination temperatures (800-1100°C) in the air for 6hrs with a 5 °C /min heating rate for giving a black

powder of $LaCo_{1-x}Zn_xO_3$ perovskite.

III.2.2. Electrodes preparation

As presented in Fig. III. 2 ,the LCZ working electrodes have been deposited by painting the catalyst ink on a pretreated nickel plates (1 cm^2). The powder is suspended in a solvent chloroform containing 1% polystyrene by mass. A brush is used to paint a thin layer. Once the deposition is completed, the solvent is evaporated in an air atmosphere until the electrode dries to carry out the electrochemical tests, where the catalyst mass loading was 8 ± 1 mg/cm^2 in each sample.

All potentials applied in this chapter are calibrated to the reversible hydrogen electrode (RHE), and the overpotential (η) are determined using the following equations **[28]**:

$$\mathbf{E}_{RHE} = \mathbf{E}_{Ag/AgCl} + 0.197 + 0.059 \times pH \ldots\ldots\ldots\ldots\ldots \textbf{(III.1)}$$

$$(\boldsymbol{\eta}) = \mathbf{E}_{RHE} - 1.23V \ldots\ldots\ldots\ldots\ldots\ldots\ldots\ldots\ldots\ldots \textbf{(III.2)}$$

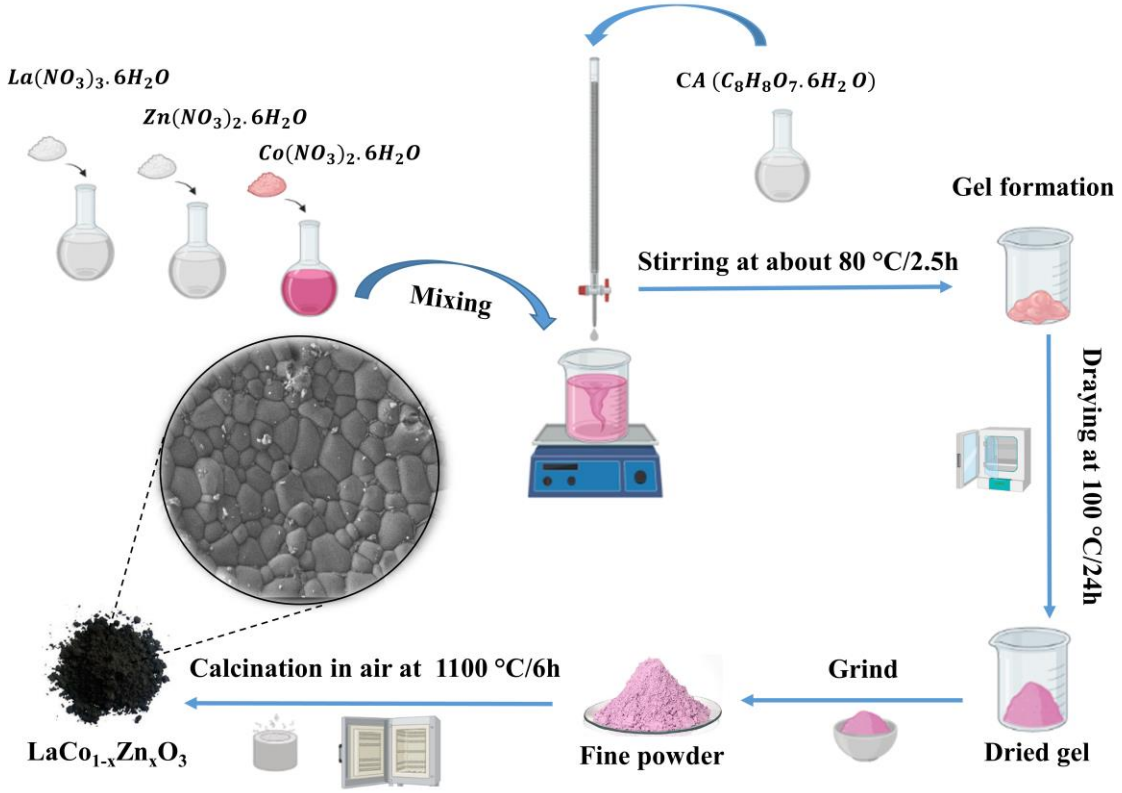

Fig. III. 1. schematic description of the LCZ materials preparation via sol-gel method.

Fig. III. 2. Schematic of LCZ electrodes preparation steps.

III.3. Results and discussion

III.3.1. Structural properties

To explore the thermal stability and decomposition reactions, the solid precursor obtained at 90 °C was examined using conventional thermal methods (TG/DTA). Since all the samples based on $LaCoO_3$ oxides, the LCZ 20 was utilized as a representative (Fig. III. 3). The TG curve exhibits that the decomposition reaction can be divided into four parts. The first part (I) of the mass loss occurs between 25 and 190 °C and is accompanied by wide endothermic and sharp exothermic processes around 125 and 160 °C in the DTA curve, possibly caused by the elimination of the remaining water and primary decomposition of the CA chain **[29]**. The second part (II) of mass loss that appears from 190 to 350 °C along with a wide-ranging endothermic process at about 248 °C, may be assigned to the transformation reaction of the citrate to aconitate **[30]**. The third part (III) of weight loss observed within the range 350 - 750 °C associated with an endothermic process centred at 430 °C, corresponds probably to reactions involving organic-metal complexes with escaping gases, such as CO_2 **[31]**. The last part (IV) of weight loss occurs above 800 °C and involves two small endothermic processes taking place at 830 and 890 °C, may be related to the formation of LCZ 20 perovskite phase **[32]**.

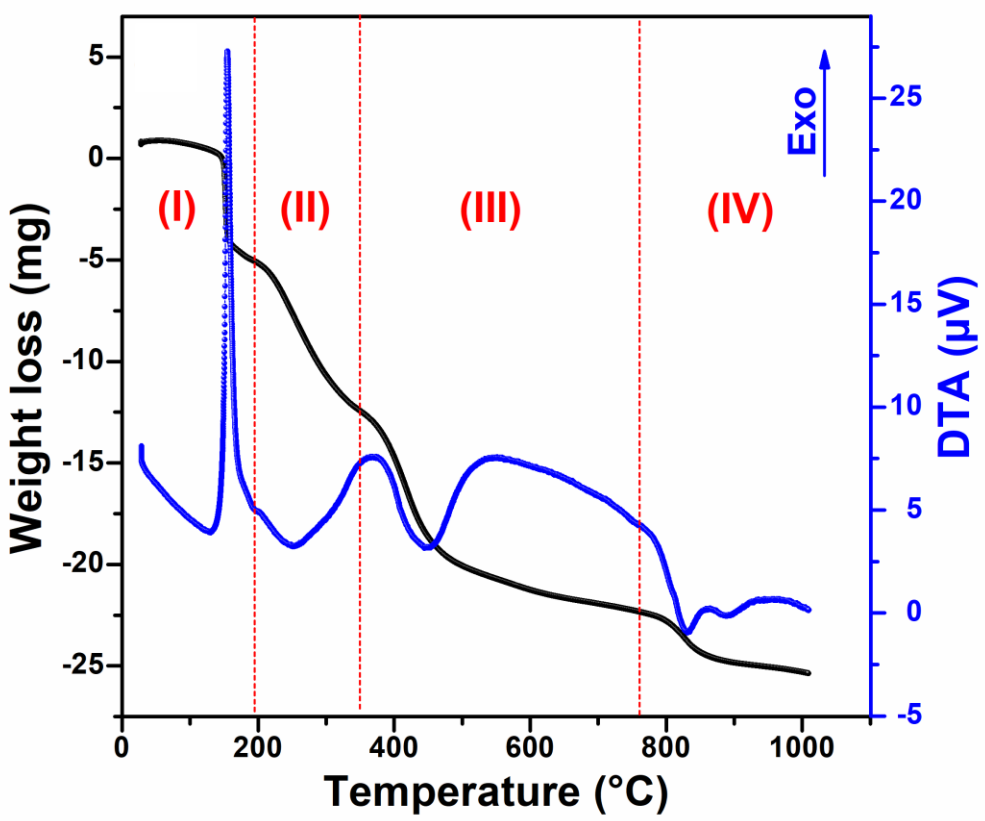

Fig. III. 3. TG-DTA curve of LCZ 20.

In order to determine the crystal structure and the purity, the prepared LCZ powders have been characterized by XRD analysis. Fig. III. 4 displays the XRD patterns of LCZ 00 heated at different calcination temperatures ranging from 800 to 1100 °C. For sample annealed at 800°C, the diffractogram shows the formation of $LaCoO_3$ perovskite structure as well as the Co_3O_4 spinel structure, where the peaks at 2θ = 23.26°, 32.94°, 33.34°, 40. 65°, 41.35°, 47.55°, 53.25°, 53.85°, 59.05°, 59.85°, 69.05°, 69.95°, 78.75°, and 79.45° correspond respectively to the (012), (110), (104), (202), (006), (024), (122), (116), (214), (018), (220), (208), (134), and (128) lattice planes of $LaCoO_3$ hexagonal system (JCPDS card 98-016-7257), while the peaks appearing at 2θ = 31.4°, 37.08° and 65.4 6° correspond

respectively to the (220), (311) and (440) lattice planes of Co_3O_4 cubic system (JCPDS card 01-076-1802). The intensity of these Co_3O_4 peaks decreases as the calcination temperature increases and the peaks completely disappear at 1100°C, where a pure $LaCoO_3$ perovskite is formed A similar trend has been previously found **[33]**.

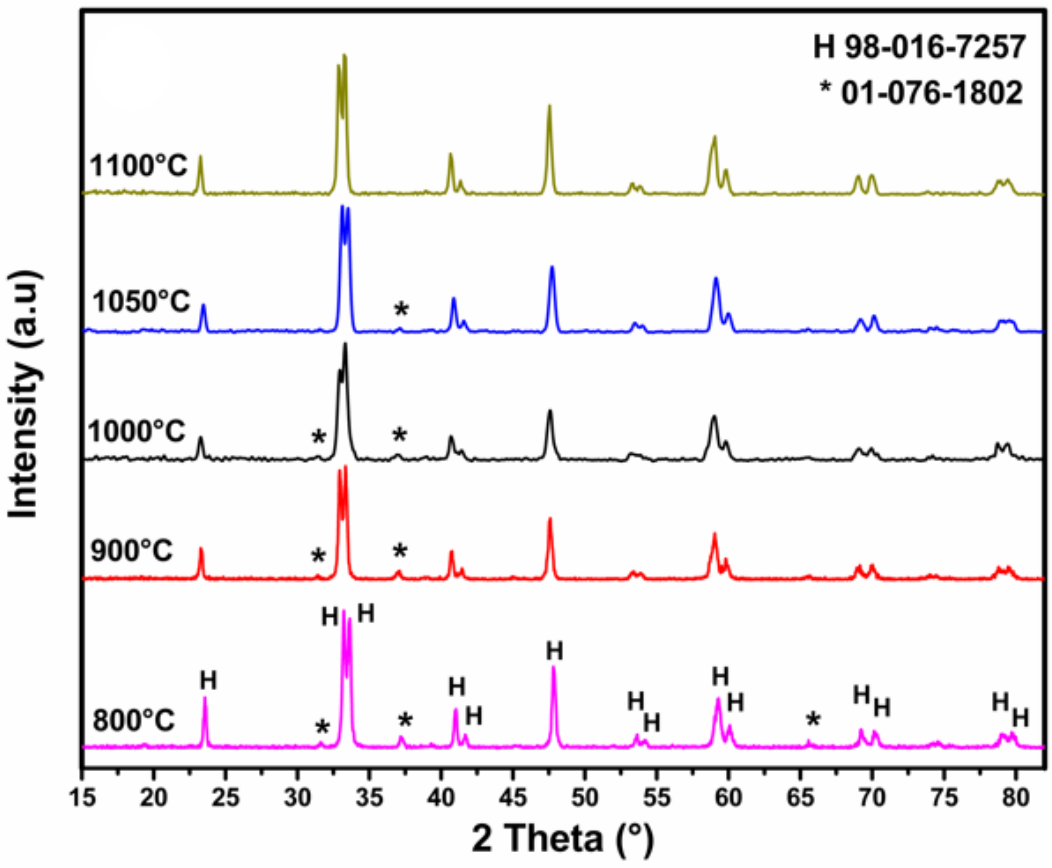

Fig. III. 4. XRD patterns of LCZ 00 calcined at different calcination temperatures (**H** $LaCoO_3$ and * Co_3O_4).

Fig. III. 5 depicts the X-ray diffractograms of the calcined LCZ powders at 1100 °C for 6 hours. The patterns of LCZ 00, 10, 20, and 30 exhibit a pure hexagonal perovskite structure (JCPDS card 98-016-7257). As the x value increases to 0.4 (LCZ 40) new peaks appear

without demolishing the perovskite structure, where the peaks marked with the * symbol could be linked to ZnO (JCPDS card 98-008-2028) and those marked with the + symbol to La_2ZnO_x (JCPDS card 00-042-0340). This result confirms that the cobalt substitution by zinc is achieved at $x \leq 0.3$, whereas another report found that the limit of solubility of zinc is reached at $x = 0.1$ when the samples are calcined for 3 hours at 750 °C **[34]**.

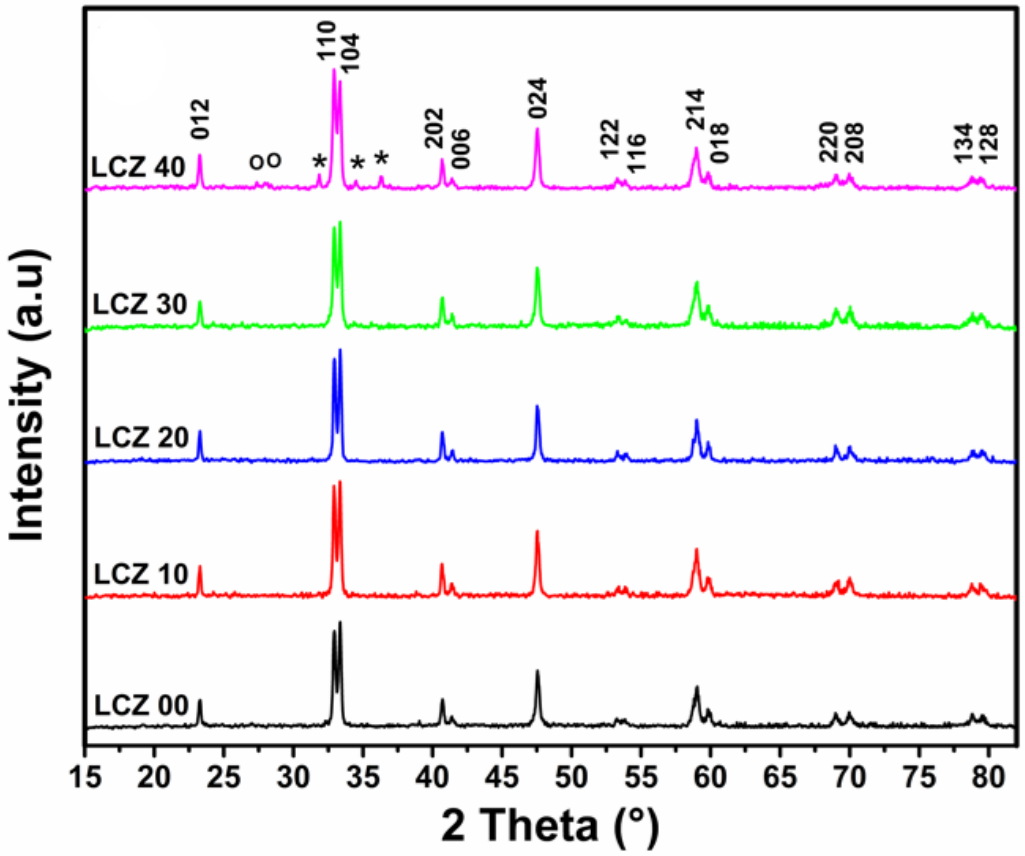

Fig. III. 5. XRD patterns of LCZ 00, 10, 20, 30 and 40 calcined at 1100 °C.

A slight shift of peaks to a lower angle with increasing the amount of zinc. Such shift can be imputable by the fact that cobalt ions were replaced by zinc ions. A comparable tendency has been previously found, where the substitution of zinc in $LaNi_{1-x}Zn_xO_3$ causes the

shift of diffraction peaks to the lower 2 theta value **[35]**. In addition, the parameters and the unit cell volumes (Table. III. 1) increase as the incorporated amount of zinc increases. The possible reason for such increase could be the difference between the Zn (0.74Å) and Co (0.61Å) ionic radius **[36]**. Furthermore, the average crystallite sizes determined by the Debye-Scherrer formula were evaluated from the peaks corresponding to the (104) and (110) planes. Such decrease confirms the replacement of cobalt ions with zinc ones in the $LaCoO_3$ lattice.

Table. III. 1. Cell parameters and crystallite sizes of LCZ powders.

Sample	LCZ 00	LCZ 10	LCZ 20	LCZ 30	LCZ 40
2 Theta (110) (°)	32.9499	32.9432	32.9393	32.9352	32.9339
2 Theta (104) (°)	33.3553	33.3479	33.3409	33.3345	33.3291
FWHM (110) (°)	0.22434	0.23355	0.24211	0.25941	0.26543
FWHM (104) (°)	0.22216	0.23748	0.23328	0.22928	0.25228
d (110)	0.271618	0.271672	0.271703	0.271736	0.271746
d (104)	0.268409	0.268466	0.268521	0.268571	0.268614

a=b (Å)	5.4323	5.4334	5.4340	5.4347	5.4349
c (Å)	13.071	13.075	13.078	13.082	13.085
V ($Å^3$)	334.10	334.30	334.46	334.62	334.71
D (nm)	37.12	35.19	34.88	34.05	32.04

To more investigate the LCZ perovskite structure, the FT-IR analysis was conducted in the range of 400-2000 cm^{-1}. Fig. III. 6 reports the FT-IR spectra of LCZ 00, 10, 20, 30 and 40 calcined at 1100 °C. The obtained spectra are fairly similar; the IR absorption bands that occurred around 415, 555, and 595 cm^{-1} may be assigned respectively to the vibrational stretching bond of La-O, the vibrational bending bond of Co-O-Co, and the vibrational stretching bond of Co-O of the octahedrally coordinated MO_6 **[37, 38]**. The less intense absorption bands located around 1110, 1388, 1461, 1613 and 1728 cm^{-1} reflect probably the crystal lattice vibrations of the LCZ perovskite **[39, 40]**. These findings are coherent with the above XRD findings and reconfirm the perovskite structure formation.

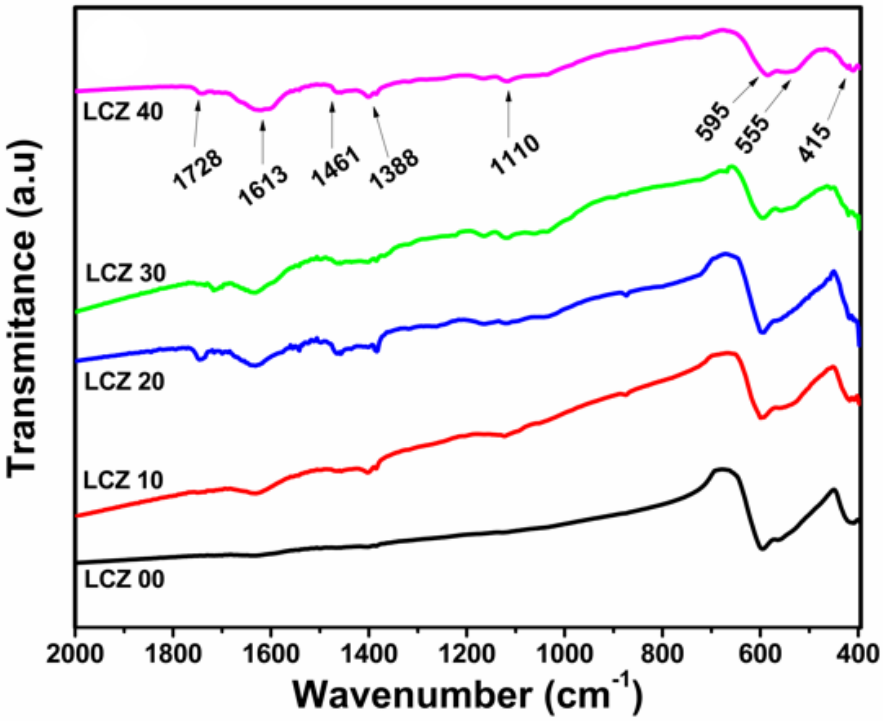

Fig. III. 6. FT-IR spectra of LCZ powders.

To investigate the elemental composition and the valence state of the LCZ catalysts' surfaces, XPS analysis was performed on LCZ 00 and LCZ 10 samples. As presented in Fig. III. 7a, the principal peaks shown in the complete XPS spectra indicate the existence of O, La, Co, Zn, as well as the C elements, proving the high purity of the synthesized LCZ samples. The fine-scanned XPS spectra of La 3d are illustrated in Fig. III. 7b, the peaks situated at around 841 and 857 eV are probably associated with La $3d_{5/2}$ and $3d_{3/2}$ electronic states of La^{3+} in the $LaCoO_3$, while the other ones located at 844 and 860 eV, might be assigned to satellite peaks resulting from the transfer of charge from oxygen 2p to lanthanum 4f **[41]**. The Cobalt 2p core level spectra are presented in Fig. III. 7c. The two major spin-orbit peaks located at ~787.5 and ~802 eV could be ascribed to the Cobalt $2p_{3/2}$ and $2p_{1/2}$, where these

peaks could be deconvolved into four minor peaks situated at 803.3, 800.3, 788.3 and 785.2 binding energies, which are probably associated to Co^{2+} ($2p_{1/2}$), Co^{3+} ($2p_{1/2}$) Co^{2+} ($2p_{3/2}$) and Co^{3+} ($2p_{3/2}$), respectively **[42]**, reflecting the coexistence of Co^{3+} and Co^{2+} valence states in the prepared LCZ catalysts. The high-resolution O 1s spectra (Fig. III. 7d) are divided into four minor peaks located roughly at 533.4, 537.2, 540.3 and 542.1 eV, which correspond possibly to the oxygen of the lattice (O^{2-}), strongly oxidative species of oxygen (O_2^{2-}/O^-), the oxygen adsorbed on the surface or hydroxyl groups (OH^-/O_2), and the surface adsorbed H_2O, sequentially **[43]**. Moreover, the Zn 2p XPS spectrum (Fig. III. 7e) exhibits the presence of Zn $2p_{1/2}$ and $2p_{3/2}$ energy states, revealing the existence of Zn^{2+} species in the LCZ catalysts **[27, 44]**. Indeed, oxygen vacancies within the perovskite-type oxides are considered to be linked to the oxygen molecules adsorbed on the surface **[45]**. Besides, the partial replacing of Co (III) by Zn (II) will yield either an increase in the valence state of Co (III) to Co (IV) or will create oxygen deficiencies for neutralizing the overall charge of $LaCoO_3$. The relative area of Co and O species are listed in Table. III. 2. The increase of the (Co^{2+}) and (-OH/O_2) peaks relative areas, suggest that the introduction of Zn into the $LaCoO_3$ led eventually to the generation of oxygen deficiencies ($La[\ (Co/Zn)^{2+}_{2\delta},\ Co^{3+}_{1-2\delta}\ ]\ O_{3-\delta}$), which are regarded as key factors in improving the OER activity **[46]**.

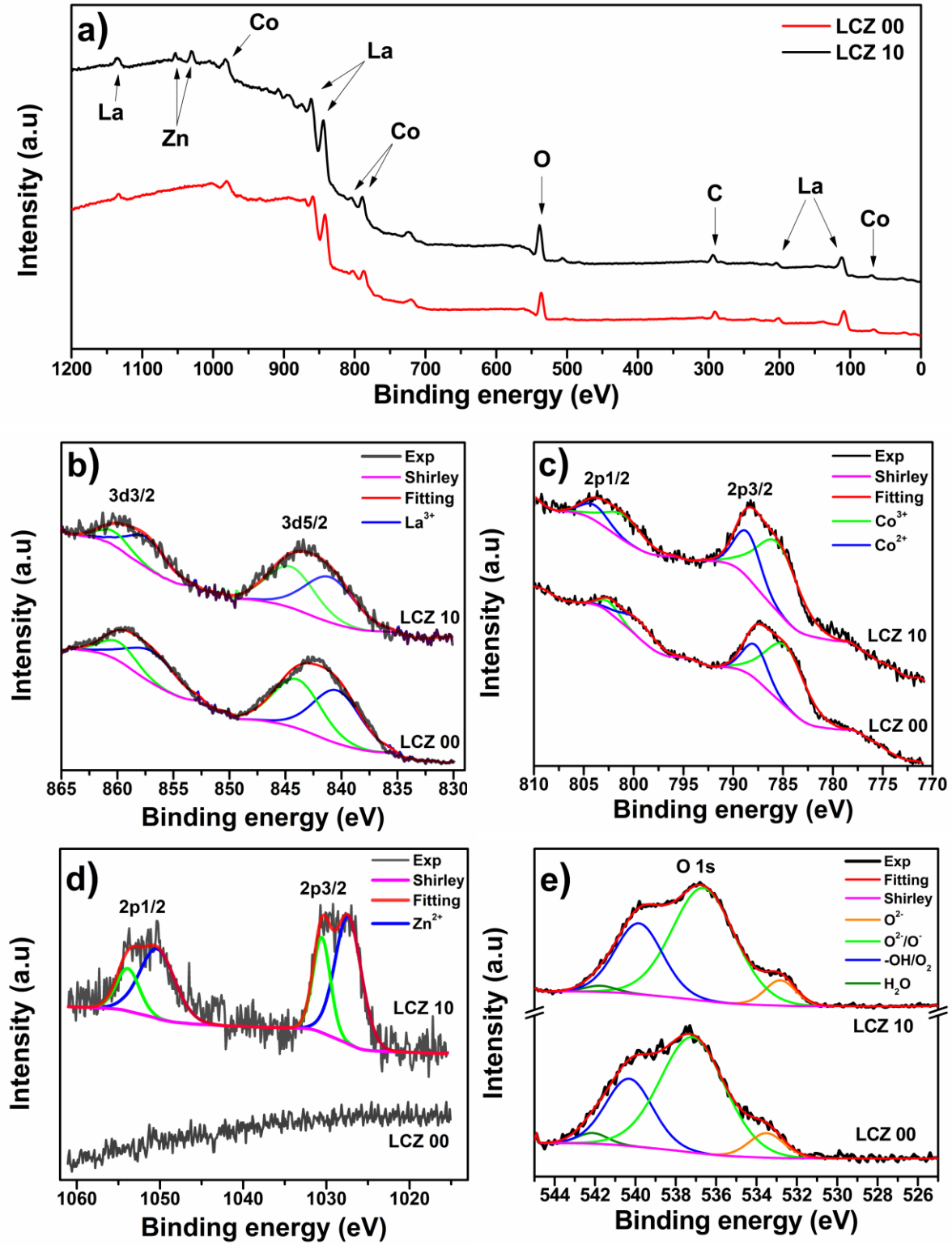

Fig. III. 7. a) Survey spectra of LCZ 00 and LCZ 10, b) La 3d XPS spectra of LCZ 00 and LCZ 10 c) Co 2p XPS spectra of LCZ 00 and LCZ 10, d) Zn 2p XPS spectra of LCZ 00 and LCZ 10, and e) O 1s XPS spectra of LCZ 00 and LCZ 10.

Table. III. 2. Relative concentrations of Co 2p and O 1s in LCZ 00 and LCZ 10.

Sample	LCZ 00 (%)	LCZ 10 (%)
O^{2-}	7.28	6.86
O^{2-}/O^{-}	63.23	61.99
-OH/O_2	26.78	29.48
H_2O	2.71	1. 67
Co^{2+}	25.39	28.96
Co^{3+}	74.61	71.04

III.3.2. Morphological properties

The microstructure of the as-synthesized LCZ perovskite was explored by SEM as depicted in Fig. III. 8a, b, c and d. The surface morphology is nearly identical and its texture appears to consist of macro-agglomeration of grains, having various shapes and sizes randomly distributed. Similar trends have been found previously for $La_{1-x}Sr_xCoO_3$ **[32]** and $La_{0.9}K_{0.1}CoO_3$ **[47]**. The agglomerate formation may be due to the solvent nature used in the synthesis of the samples as reported earlier **[48]**. It was proven that ethanol treatment of the precipitate causes interactions between the grains, which induces the forming of chemical bonds. The presence of black color in SEM images means void, which indicates high surface area. Besides, the grain size distribution presented in Fig. III. 8e shows that the grain median diameter D_{50} increases, elucidating that increasing the amount of Zn releases the grain growth.

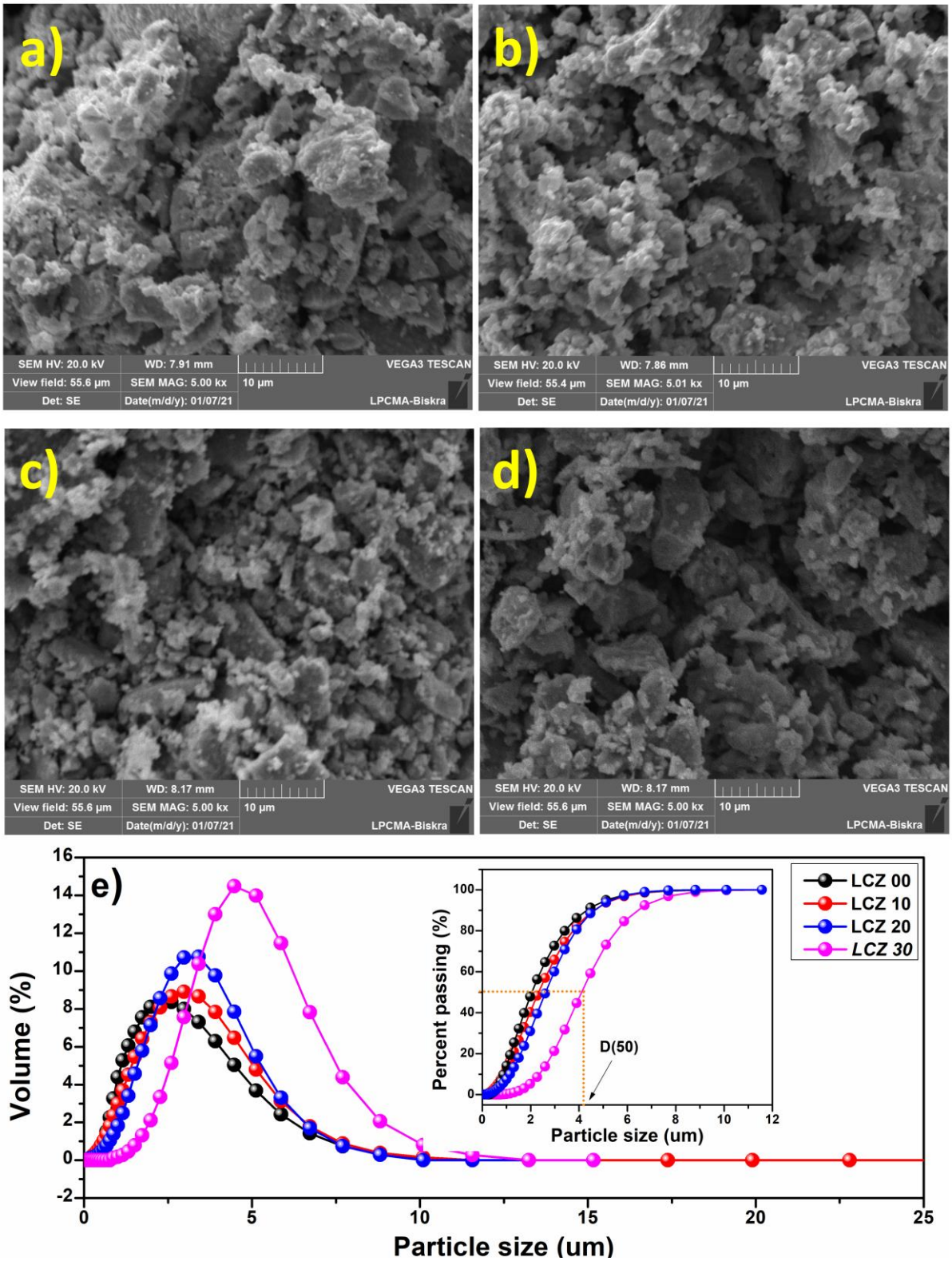

Fig. III. 8. a, b, c and d) SEM micrographs of LCZ 00, 10, 20 and 30 respectively, c) grain size distribution of LCZ 00, 10, 20 and 30.

The EDS analysis was conducted to further explore the purity and elements contained in the elaborated LCZ samples. The EDS spectra depicted in Fig. III. 9 reveals clearly the existence of zinc, cobalt, lanthanum, and oxygen atoms. The presence of silver peaks at around (3 KeV) is most likely resulting from the metallization of the samples before analysis. No further elemental peaks are present, which demonstrates the high purity of the elaborated LCZ samples.

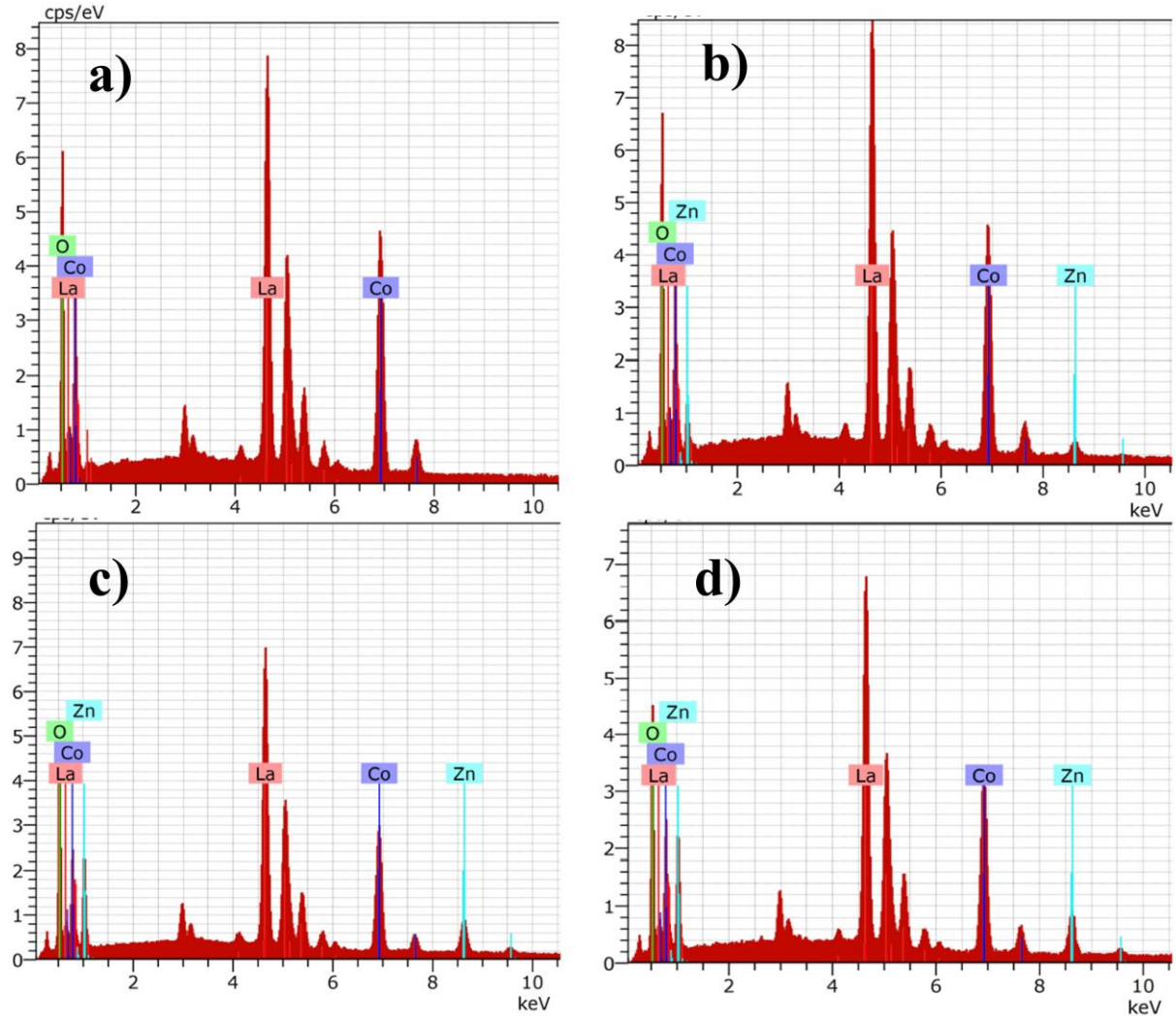

Fig. III. 9. EDS spectra. a) LCZ 00, b) LCZ 10, c) LCZ 20 and d) LCZ 30.

N_2 adsorption-desorption measurements were implemented to assess the pore size distribution as well as specific surface area of the LCZ microstructure. Fig. III. 10 a, b, c and d show distinct hysteresis loops with typical type IV isotherm behavior, revealing the mesoporosity as well as the suspected microporosity of the LCZ catalysts **[49]**. In addition, Fig. III. 10 e and f illustrate the BJH pore size distribution. The LCZ catalysts have a pore size ranging from 1.55 to 8.5 nm, and most of the pores are less than 3.5 nm, indicating the presence of micropores and mesopores.

As a result, the introduction of zinc into $LaCoO_3$ catalyst increases both the BET specific surface, volume and diameter of the pores (Table. III. 3). We suppose that this will allow for high accessibility of the electrolyte ions, an enhanced interface (electrode/electrolyte) and facilitate the diffusion of ions **[50]**.

Table. III. 3. The D50, specific surface area, pore volume, and pore diameter of LCZ 00, LCZ 10, LCZ 20, and LCZ 30.

Catalyst	D_{50} (µm)	Specific surface ($m^2.g^{-1}$)	Pore volume ($cm^3.g^{-1}$)	Pore diameter (nm)
LCZ 00	2.05	2.58	0.004	1.564
LCZ 10	2.32	2.77	0.004	1.583
LCZ 20	2.65	2.67	0.006	1.891
LCZ 30	4.05	3.03	0.006	1.564

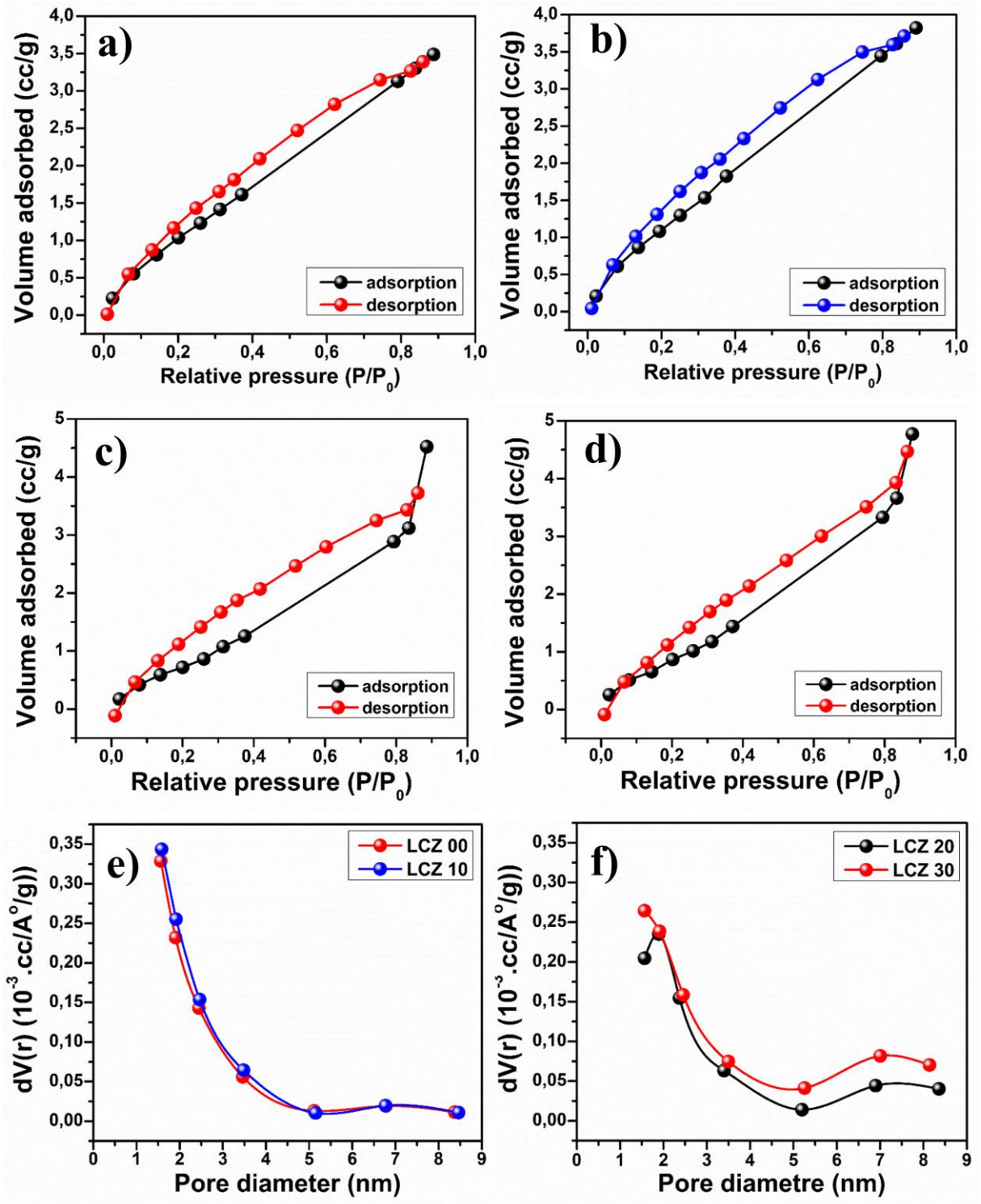

Fig. III. 10. N_2 adsorption-desorption isotherms of; a) LCZ 00, b) LCZ 10, c) LCZ 20 and d) LCZ 30. Pore size distribution of; e) LCZ 00 and LCZ 10, f) LCZ 20 and LCZ 30.

III.3.3. Electrocatalytic properties

The linear sweep voltammograms of the LCZ materials recorded between 1.05 and 1.73 (V vs RHE) in N_2-saturated 1 M KOH at 10 $mV.s^{-1}$ sweep rate are represented in Fig. III. 11. Apparently, the electrocatalysts behave fairly similarly and the voltammograms can be divided into three sections: the small increase in the current density over the potential window of 1.1-1.38 V may be ascribed to the electrochemical double layer formation, the broad peak appears between 1.37 and 1.53 V possibly because of the intercalation of the electrolyte's oxygen ions into the oxygen deficiencies included in the $LaCoO_3$ lattice, which leads the Co (II) to oxidize Co (III) and then to Co (IV) **[51, 52]**, while the continuous increase in the current density beyond 1.53 V, most likely associated with the OER **[53]**. In addition, the substitution of cobalt by zinc can trigger the improvement of the electrocatalytic activity, where the LCZ 10 electrocatalyst displays the best OER activity compared to the other studied samples. This is presumably due to a large amount of oxygen vacancies observed in the previous XPS analysis **[46]**.

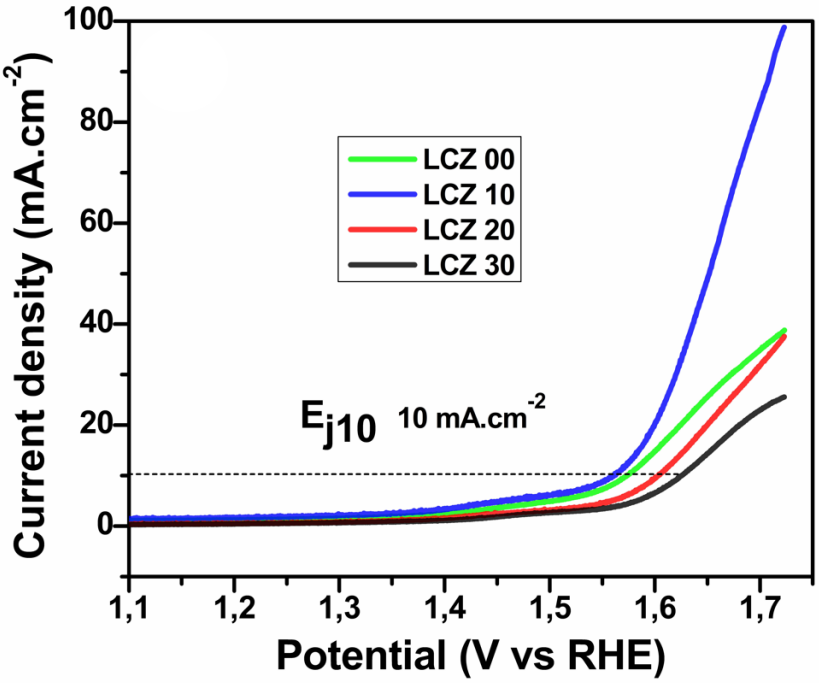

Fig. III. 11. linear sweep voltammograms of LCZ electrocatalysts.

The overpotentials and current densities versus the zinc content are given in Fig. III. 12. The LCZ 10 electrocatalyst exhibits the least overpotential of only 325 mV to attain the specific current of 10 $mA.cm^{-2}$, whereas the undoped LCZ 00, LCZ 20, and LCZ 30 electrocatalysts need overpotentials of 347, 375 and 398 mV, respectively, to afford the similar current density. Moreover, at a specified overpotential of 450 mV, LCZ10 delivers the highest current density ~73.41 $mA.cm^{-2}$, which is about two times higher than that of LCZ 00 ~32.57 $mA.cm^{-2}$. Besides, it has been shown that higher zinc substitution (LCZ 20 and LCZ 30) adversely affect the catalytic efficiency. A comparable performance was shown when zinc was introduced into $LaFeO_3$ **[24]**.

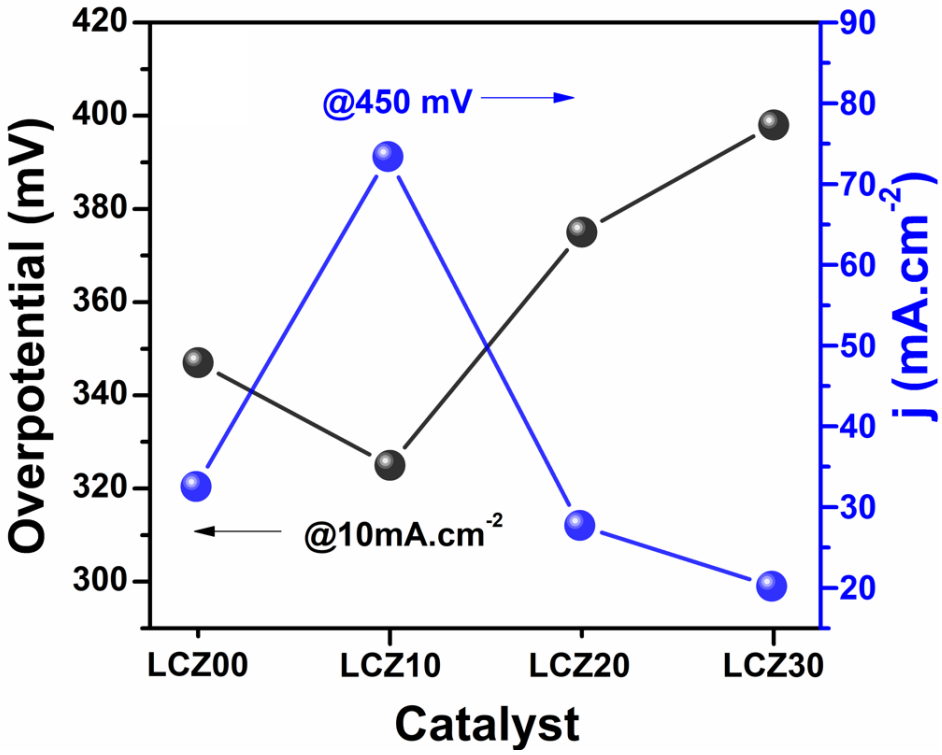

Fig. III. 12. Overpotentials and current densities at given current and potential as a function of LCZ electrocatalysts.

To evaluate the OER kinetic parameters, the anodic Tafel polarization of the LCZ electrocatalysts were accomplished at 10 $mV.s^{-1}$ scan rate. As illustrated in Fig. III. 13, the LCZ 10 has the much lower slope of 92 $mV.dec^{-1}$ compared to the studied samples, where the undoped sample gives 117 $mV.dec^{-1}$, LCZ 20 (102 $mV.dec^{-1}$) and LCZ 30 (128 $mV.dec^{-1}$). This outcome indicates probably the rapid transfer of electrons and mass in LCZ 10 during the water splitting reaction [54], which could explain the enhanced electrocatalytic performance of LCZ 10.

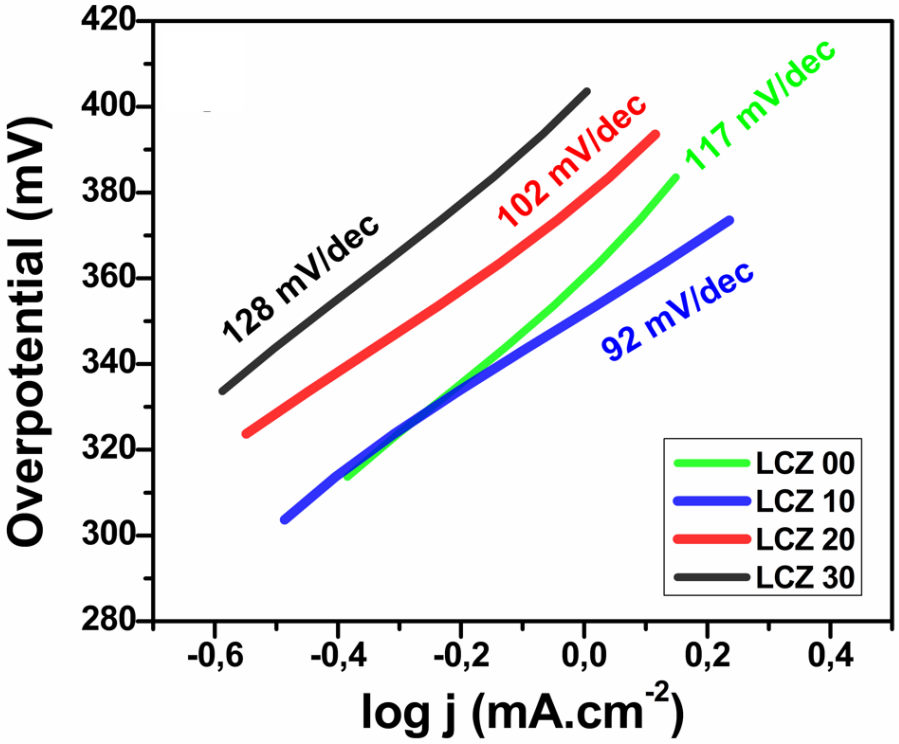

Fig. III. 13. Tafel plot of LCZ electrocatalysts.

The alteration of the Tafel slope by zinc doping indicates an adjustment of the rate-determining step **[55]**. In fact, it has been proven that the OER rate-step on perovskite is determined by the removal difficulty of the OH intermediates **[56]**. Hence, it is possible to suggest that this change from 117 $mV.dec^{-1}$ (LCZ 00) to 92 $mV.dec^{-1}$ (LCZ 10) is caused by the decreased difficulty in removing OH intermediates. Moreover, Fig. III. 14 exhibits the Tafel slope versus the overpotential of several perovskite-type-based OER electrocatalysts. The as-synthesized LCZ 10 demonstrates a comparable and even better performance than several materials previously reported **[16, 22, 41, 57-67]**.

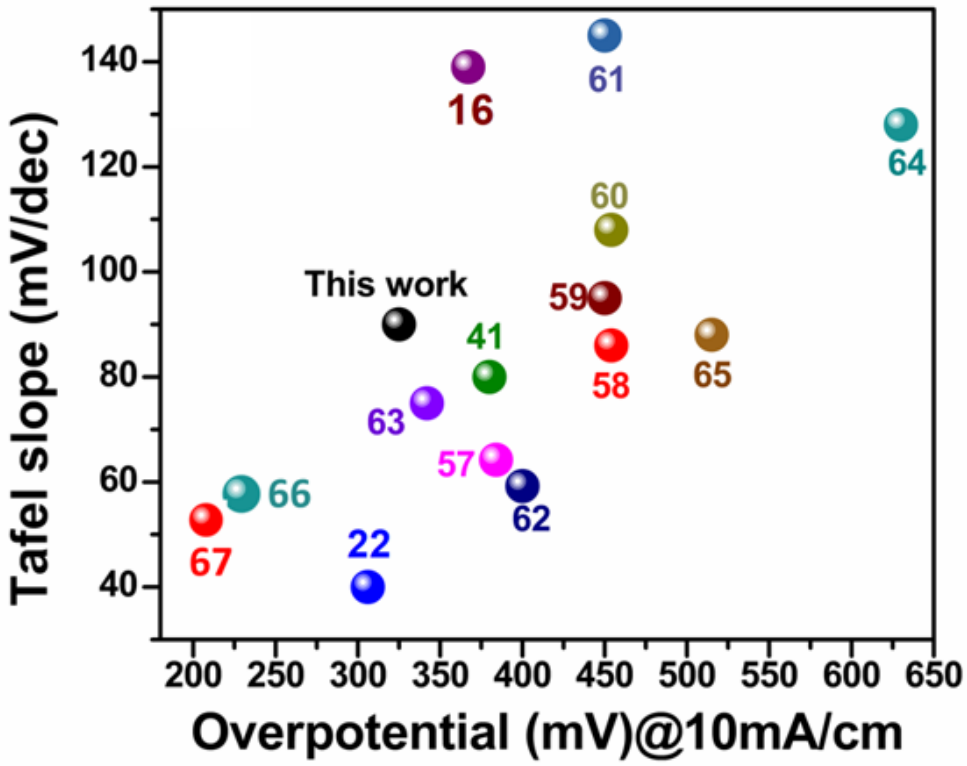

Fig. III. 14. Tafel slopes vs. overpotentials (@10 mA.cm^{-2}) of previously reported electrocatalysts.

Electrochemical impedance spectroscopy was used to obtain further information on the kinetic process of the OER. Fig. III. 16 presents the obtained Nyquist plots of LCZ electrocatalysts measured at the obtained potentials corresponding to 10 mA.cm^{-2}, along with their fitted spectra. Fig. III. 15 depicts the equivalent circuit that was used to simulate the impedance parameters and Table. III. 4 lists the estimated values, in which L, R_s, R_{ct}, Q_{dl}, R_f, and Q_f refer, respectively, to the inductance, electrolyte resistance, constant phase element linked to the electrochemical double layer, charge transfer resistance, oxide film resistance, and constant phase element associated with the oxide film capacitance.

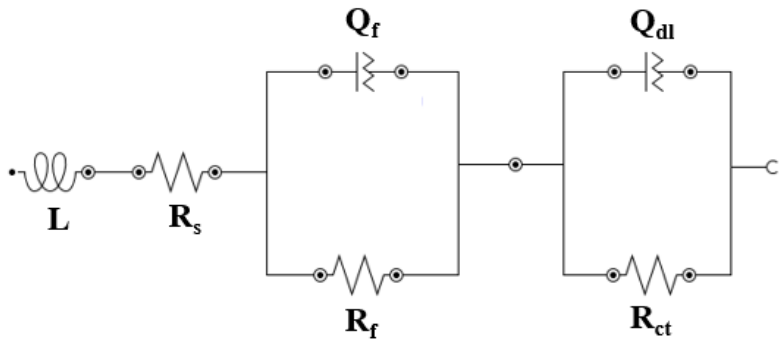

Fig. III. 15. The equivalent circuits used to fit the impedance data.

Table. III. 4. Electrochemical parameters of LCZ electrocatalysts obtained by fitting EIS-Nyquist plot with an equivalent circuit model.

Electro-catalyst	L (10^{-7}.H)	R_s (Ω)	R_{ct} (Ω)	Q_{dl} ($F.s^{n-1}/cm^2$)	n_{dl}	R_f (Ω)	Q_f ($F.s^{n-1}/cm^2$)	n_f
LCZ 00	4.87	2.0	343	0.0167	0.26	802	0.0114	0.97
LCZ 10	1.49	1.5	122	0.0068	0.88	32.2	0.0097	0.51
LCZ 20	12	1.8	248	0.0079	0.85	16.7	0.0117	0.39
LCZ 30	23	2.7	462	0.0044	0.84	23.2	0.0075	0.37

A good correspondence is found between the experimental and simulated curves. The LCZ 10 electrocatalyst unravels the lowest electrolyte resistance (1.5 Ω), elucidating the enhanced electronic conductivity compared to the pristine one (2 Ω) **[68]**. Moreover, the LCZ 10 electrocatalyst also exhibits the lowest charge-transfer resistance followed by LCZ 20,

LCZ 00 and LCZ 30 respectively, reflecting the good charge-transfer efficiency and also faster reaction kinetics in comparison with the other samples **[53]**. The obtained results are entirely consistent with the LSV and Tafel slope above and strongly confirm that the incorporation of an appropriate amount of zinc considerably boosts the OER activity of $LaCoO_3$ perovskite.

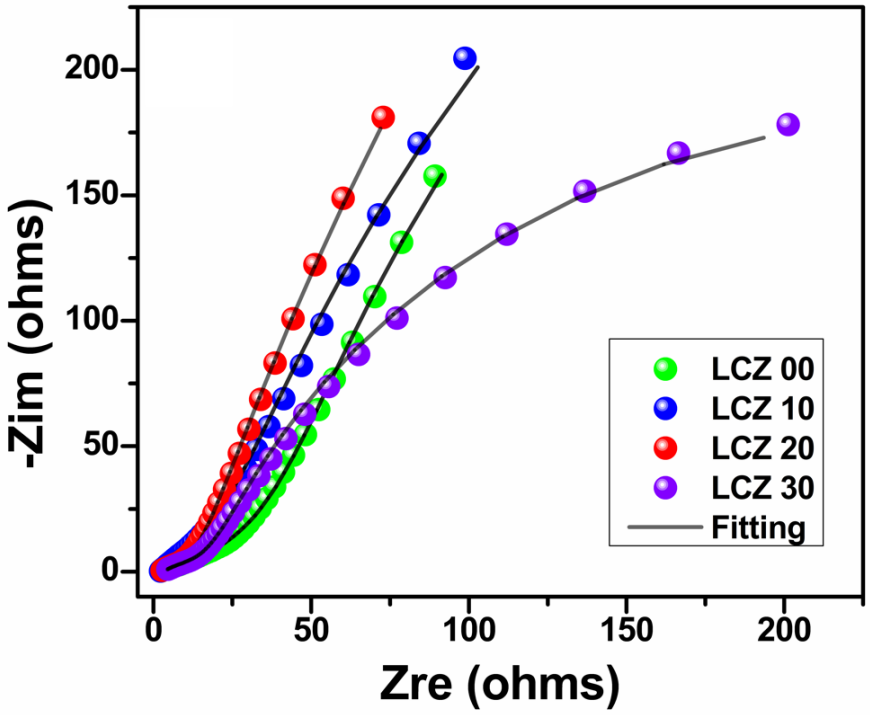

Fig. III. 16. EIS spectra of LCZ electrocatalysts.

At last, the durability of an electrocatalyst is a further key factor to be considered, particularly for the practical application **[69]**. The lifetime durability of the LCZ 10 electrocatalyst is tested by using the chronopotentiometry measurement recorded at 10 $mA.cm^{-2}$ over 24 hours. As illustrated in Fig. III. 17, time-dependent potential of the LCZ 10 electrocatalyst starts to gradually decline up to ~3 hours, this phenomenon is likely to be

caused by the activation process (i.e. the increase of electroactive sites) **[53].** Thereafter, the electrocatalyst remains steady up to ~12 hours, then begins to decay gradually up to ~24 hours. This behavior could be related to the continual formation and destruction of oxygen gas bubbles on the electrocatalyst's surface, resulting in an activity loss of less than 4 %, reflecting excellent electrocatalytic stability toward the OER **[62]**.

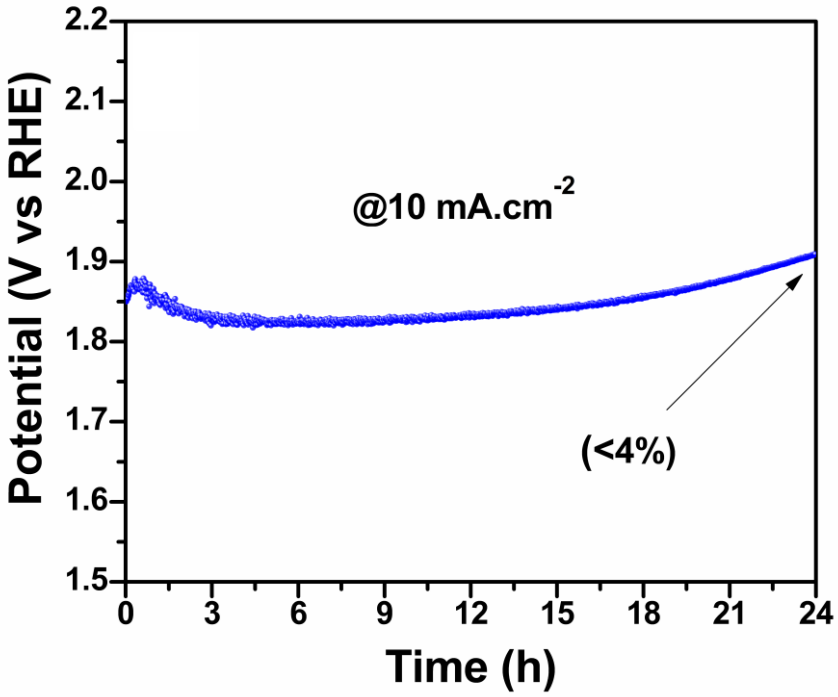

Fig. III. 17. Chronopotentiometric measurements of LCZ 10 electrocatalyst.

Conclusions

In summary, we have examined the impact of Zn doping on the structural and electrocatalytic performance of new $LaCo_{1-x}Zn_xO_3$ electrocatalysts elaborated using the sol-gel technique. The structural analysis confirms that the solubility limit of zinc into $LaCoO_3$ achieved up to $x \leq 0.3$. Furthermore, the incorporation of zinc causes the unit cell

volume to swell, led to the generation of oxygen deficiencies, allows grain size to grow and increases the pore volume as well as specific surface. The electrocatalytic investigations demonstrate that Zn-doping with an appropriate amount (x = 0.1) boosts the electrocatalytic performance of $LaCoO_3$ toward the OER by reducing the overpotential (only 327 mV), Tafel slope (92 $mV.dec^{-1}$), resistance of charge-transfer (122 Ω) compared to the pristine electrocatalyst. Moreover, the LCZ 10 electrocatalyst also demonstrates an excellent stability over 24 hours of use. The outstanding electrochemical performance of this novel LCZ 10 electrocatalyst confirms the promising candidate for replacing precious metal electrocatalysts for practical alkaline water electrolysis.

References

[1] R. Sankannavar, A. Sarkar, The electrocatalysis of oxygen evolution reaction on $La_{1-x}Ca_xFeO_{3-\delta}$ perovskites in alkaline solution, Int. J. Hydrog. Energy 43 (2018) 4682-4690.

[2] F. Manzano-Agugliaro, A. Alcayde, F.G. Montoya, A. Zapata-Sierra, C. Gil, Scientific production of renewable energies worldwide: An overview, Renew. Sust. Energ. Rev. 18 (2013) 134-143.

[3] R. Baños, F. Manzano-Agugliaro, F.G. Montoya, C. Gil, A. Alcayde, J. Gómez, Optimization methods applied to renewable and sustainable energy: A review, Renew. Sust. Energ. Rev. 15 (2011) 1753-1766.

[4] Z. Xiao, Y. Wang, Y.-C. Huang, Z. Wei, C.-L. Dong, J. Ma, S. Shen, Y. Li, S. Wang, Filling the oxygen vacancies in Co_3O_4 with phosphorus: an ultra-efficient electrocatalyst for overall water splitting, Energy Environ. Sci. 10 (2017) 2563-2569.

[5] M. Negem, H. Nady, M.M. El-Rabiei, Nanocrystalline nickel–cobalt electrocatalysts to generate hydrogen using alkaline solutions as storage fuel for the renewable energy, Int. J. Hydrog. Energy 44 (2019) 11411-11420.

[6] M. Li, H. Wang, W. Zhu, W. Li, C. Wang, X. Lu, RuNi Nanoparticles Embedded in N-Doped Carbon Nanofibers as a Robust Bifunctional Catalyst for Efficient Overall Water Splitting, Adv. Sci. 7 (2020) 1901833.

[7] L. Trotochaud, S.W. Boettcher, Precise oxygen evolution catalysts: Status and opportunities, Scr. Mater. 74 (2014) 25-32.

[8] Z.W. Seh, J. Kibsgaard, C.F. Dickens, I. Chorkendorff, J.K. Norskov, T.F. Jaramillo,

Combining theory and experiment in electrocatalysis: Insights into materials design, Science 355 (2017).

[9] T. Zhao, Y. Wang, X. Chen, Y. Li, Z. Su, C. Zhao, Vertical Growth of Porous Perovskite Nanoarrays on Nickel Foam for Efficient Oxygen Evolution Reaction, ACS Sustain. Chem. Eng. 8 (2020) 4863-4870.

[10] Y. Lee, J. Suntivich, K.J. May, E.E. Perry, Y. Shao-Horn, Synthesis and Activities of Rutile IrO_2 and RuO_2 Nanoparticles for Oxygen Evolution in Acid and Alkaline Solutions, J. Phys. Chem. Lett. 3 (2012) 399-404.

[11] S. She, J. Yu, W. Tang, Y. Zhu, Y. Chen, J. Sunarso, W. Zhou, Z. Shao, A Systematic Study of Oxygen Evolution Activity and Stability on $La_{1-x}Sr_xFeO_{3-\delta}$ Perovskite Electrocatalysts in Alkaline Media, ACS Appl. Mater. Interfaces 10 (2018) 11715-11721.

[12] R.-h. Yuan, Y. He, W. He, M. Ni, M.K.H. Leung, Bifunctional electrocatalytic activity of $La_{0.8}Sr_{0.2}MnO_3$-based perovskite with the A-site deficiency for oxygen reduction and evolution reactions in alkaline media, Appl. Energy 251 (2019) 113406.

[13] K. Zhu, H. Liu, X. Li, Q. Li, J. Wang, X. Zhu, W. Yang, Oxygen evolution reaction over Fe site of $BaZr_xFe_{1-x}O_{3-\delta}$ perovskite oxides, Electrochim. Acta 241 (2017) 433-439.

[14] W.T. Hong, M. Risch, K.A. Stoerzinger, A. Grimaud, J. Suntivich, Y. Shao-Horn, Toward the rational design of non-precious transition metal oxides for oxygen electrocatalysis, Energy Environ. Sci. 8 (2015) 1404-1427.

[15] B. Han, M. Risch, Y.L. Lee, C. Ling, H. Jia, Y. Shao-Horn, Activity and stability trends of perovskite oxides for oxygen evolution catalysis at neutral pH, Phys. Chem. Chem. Phys.

17 (2015) 22576-80.

[16] E. Omari, M. Omari, Cu-doped $GdFeO_3$ perovskites as electrocatalysts for the oxygen evolution reaction in alkaline media, Int. J. Hydrog. Energy 44 (2019) 28769-28779.

[17] M.E. Hilal, S.B. Şanlı, S. Dekyvere, G. Çakmak, H.A. Younus, F. Pişkin, F. Verpoort, B. Pişkin, A dual-doping strategy of $LaCoO_3$ for optimized oxygen evolution reaction toward zinc-air batteries application, Int. J. Energy Res. 46 (2022) 22014-22024.

[18] K. Li, Z. Dong, Z. Lü, Study of the bifunctional catalytic activity on Sr and Mn co-doped $PrFeO_{3-\delta}$ Zinc-Air batteries cathode, Electrochim. Acta 430 (2022) 141123.

[19] M.A. Ghanem, M.S. Amer, P. Arunachalam, A.M. Al-Mayouf, M.T. Weller, Role of rhodium doping into lanthanum cobalt oxide ($LaCoO_3$) perovskite and the induced bifunctional activity of oxygen evolution and reduction reactions in alkaline medium, Arab. J. Chem. 15 (2022) 104256.

[20] B. Bao, Y. Liu, M. Sun, B. Huang, Y. Hu, P. Da, D. Ji, P. Xi, C.H. Yan, Boosting the Electrocatalytic Oxygen Evolution of Perovskite $LaCo_{1-x}Fe_xO_3$ by the Construction of Yolk-Shell Nanostructures and Electronic Modulation, Small 18 (2022) 2201131.

[21] R. Xie, Z. Nie, X. Hu, Y. Yu, C. Aruta, N. Yang, Pr-doped $LaCoO_3$ toward stable and efficient oxygen evolution reaction, ACS Appl. Energy Mater. 4 (2021) 9057-9065.

[22] Y. Sun, Z. Zhao, S. Wu, W. Li, B. Wu, G. Liu, G. Chen, B. Xu, B. Kang, Y. Li, Engineering of the d-Band Center of Perovskite Cobaltite for Enhanced Electrocatalytic Oxygen Evolution, ChemSusChem 13 (2020) 2671-2676.

[23] R. Andoulsi-Fezei, K. Horchani-Naifer, M. Férid, Influence of zinc incorporation on the

structure and conductivity of lanthanum ferrite, Ceram. Int. 42 (2016) 1373-1378.

[24] E. Omari, M. Omari, Synthesis and electrocatalytic properties of $LaFe_{1-x}Zn_xO_3$ perovskites, J. Sol. -Gel Sci. Technol. 96 (2020) 219-225.

[25] J. Wu, Y. Zhang, B. Zhang, S. Li, P. Xu, Zn-doped CoS_2 nanoarrays for an efficient oxygen evolution reaction: understanding the doping effect for a precatalyst, ACS Appl. Mater. Interfaces 14 (2022) 14235-14242.

[26] L. Song, X. Zhang, S. Zhu, Y. Xu, Y. Wang, Transition metal (Fe, Ni, and Zn) doping-induced modulation of geometric and electronic structures to optimize the potential-determining step of $MnCo_2O_4$ for oxygen evolution reaction, Sci. China Mater. 65 (2022) 2871-2878.

[27] J. Han, J. Zhang, T. Wang, Q. Xiong, W. Wang, L. Cao, B. Dong, Zn Doped FeCo Layered Double Hydroxide Nanoneedle Arrays with Partial Amorphous Phase for Efficient Oxygen Evolution Reaction, ACS Sustain. Chem. Eng. 7 (2019) 13105-13114.

[28] X. Bo, Y. Li, R.K. Hocking, C. Zhao, NiFeCr Hydroxide Holey Nanosheet as Advanced Electrocatalyst for Water Oxidation, ACS Appl. Mater. Interfaces 9 (2017) 41239-41245.

[29] M. Lebid, M. Omari, Synthesis and Electrochemical Properties of $LaFeO_3$ Oxides Prepared Via Sol–Gel Method, Arab J Sci Eng 39 (2013) 147-152.

[30] Y.-M. Hon, K.-Z. Fung, M.-H. Hon, Synthesis and characterization of $Li_{1+\delta}Mn_{2-\delta}O_4$ powders prepared by citric acid gel process, J. Eur. Ceram. Soc. 21 (2001) 515-522.

[31] E. Omari, S. Makhloufi, M. Omari, Preparation by Sol–Gel Method and Characterization of Co-doped LaNiO3 Perovskite, J Inorg Organomet Polym Mater 27 (2017) 1466-1472.

[32] S. Cizauskaite, A. Kareiva, Sol-gel preparation and characterization of non-substituted and Sr-substituted lanthanum cobaltates, Cent. Eur. J. Chem. 6 (2008) 456-464.

[33] Y. Wu, B. Chu, M. Zhang, Y. Yi, L. Dong, M. Fan, G. Jin, L. Zhang, B. Li, Influence of calcination temperature on the catalytic properties of $LaCu_{0.25}Co_{0.75}O_3$ catalysts in NO_x reduction, Appl. Surf. Sci. 481 (2019) 1277-1286.

[34] F. Ma, W. Chu, L. Huang, X. Yu, Y. Wu, Steam Reforming of Ethanol over Zn-Doped $LaCoO_3$ Perovskite Nanocatalysts, Chinese J. Catal. 32 (2011) 970-977.

[35] J. Shao, G. Zeng, Y. Li, Effect of Zn substitution to a $LaNiO_{3-\delta}$ perovskite structured catalyst in ethanol steam reforming, Int J Hydrogen Energy 42 (2017) 17362-17375.

[36] I. Chadli, M. Omari, M. Abu Dalo, B.A. Albiss, Preparation by sol–gel method and characterization of Zn-doped $LaCrO_3$ perovskite, J. Sol. -Gel Sci. Technol. 80 (2016) 598-605.

[37] S. Priyatharshni, A. Tamilselvan, C. Viswanathan, N. Ponpandian, $LaCoO_3$ Nanostructures Modified Glassy Carbon Electrode for Simultaneous Electrochemical Detection of Dopamine, Ascorbic Acid and Uric Acid, J. Electrochem. Soc. 164 (2017) B152-B158.

[38] R. Andoulsi, K. Horchani-Naifer, M. Férid, Effect of the preparation route on the structure and microstructure of $LaCoO_3$, Chemical Papers 68 (2014) 608-613.

[39] M. Surendar, T.V. Sagar, G. Raveendra, M. Ashwani Kumar, N. Lingaiah, K.S. Rama Rao, P.S. Sai Prasad, Pt doped $LaCoO_3$ perovskite: A precursor for a highly efficient catalyst for hydrogen production from glycerol, Int. J. Hydrog. Energy 41 (2016) 2285-2297.

[40] M. Sivakumar, M. Sakthivel, S.-M. Chen, P. Veerakumar, S.-B. Liu, Sol-Gel Synthesis of Carbon-Coated $LaCoO_3$ for Effective Electrocatalytic Oxidation of Salicylic Acid, ChemElectroChem 4 (2017) 935-940.

[41] D. Ji, C. Liu, Y. Yao, L. Luo, W. Wang, Z. Chen, Cerium substitution in $LaCoO_3$ perovskite oxide as bifunctional electrocatalysts for hydrogen and oxygen evolution reactions, Nanoscale 13 (2021) 9952-9959.

[42] Y. Cao, B. Lin, Y. Sun, H. Yang, X. Zhang, Symmetric/Asymmetric Supercapacitor Based on the Perovskite-type Lanthanum Cobaltate Nanofibers with Sr-substitution, Electrochim. Acta 178 (2015) 398-406.

[43] B. Zhang, C. Yu, Z. Li, Enhancing the electrochemical properties of $LaCoO_3$ by Sr-doping, rGO-compounding with rational design for energy storage device, Nanoscale Res. Lett. 15 (2020) 1-13.

[44] X. Liu, Z. Chang, L. Luo, T. Xu, X. Lei, J. Liu, X. Sun, Hierarchical $ZnxCo_{3-x}O_4$ Nanoarrays with High Activity for Electrocatalytic Oxygen Evolution, Chem. Mater. 26 (2014) 1889-1895.

[45] A.K. Tomar, G. Singh, R.K. Sharma, Fabrication of a Mo-doped strontium cobaltite perovskite hybrid supercapacitor cell with high energy density and excellent cycling life, ChemSusChem 11 (2018) 4123-4130.

[46] Y. Lu, A. Ma, Y. Yu, R. Tan, C. Liu, P. Zhang, D. Liu, J. Gui, Engineering oxygen vacancies into $LaCoO_3$ perovskite for efficient electrocatalytic oxygen evolution, ACS Sustain. Chem. Eng. 7 (2018) 2906-2910.

[47] W. Wei, D. Chuanjin, X. Xiang, Q.J.J.o.W.U.o.T.-M.S.E. Xiaojin, Preparation of $La_{0.9}K_{0.1}CoO_3$ perovskite composite oxide, J. Wuhan Univ. Technol. Mater. Sci. Ed. 20 (2005) 32-34.

[48] G. Jung, T. Huang, M. Huang, C. Chang, Preparation of samaria-doped ceria for solid-oxide fuel cell electrolyte by a modified sol-gel method, J. Mater. Sci. 36 (2001) 5839-5844.

[49] K.S. Sing, Reporting physisorption data for gas/solid systems with special reference to the determination of surface area and porosity (Recommendations 1984), Pure Appl. Chem. 57 (1985) 603-619.

[50] G.M. Tomboc, H.S. Jadhav, H. Kim, PVP assisted morphology-controlled synthesis of hierarchical mesoporous $ZnCo_2O_4$ nanoparticles for high-performance pseudocapacitor, Chem. Eng. J. 308 (2017) 202-213.

[51] G. Guo, K. Ouyang, J. Yu, Y. Liu, S. Feng, M. Wei, Facile synthesis of $LaCoO_3$ with a high oxygen vacancy concentration by the plasma etching technique for high-performance oxygen ion intercalation pseudocapacitors, ACS Appl. Energy Mater. 3 (2019) 300-308.

[52] F. Hadji, M. Omari, M. Mebarki, N. Gabouze, A. Layadi, Zinc doping effect on the structural and electrochemical properties of $LaCoO_3$ perovskite as a material for hybrid supercapacitor electrodes, J. Alloy. Compd. 942 (2023) 169047.

[53] E. Omari, M. Omari, Enhancing catalytic activity of $NdFeO_3$ perovskite by tuning A-site cation deficiency for oxygen evolution reaction, Int. J. Hydrog. Energy 47 (2022) 14542-14551.

[54] J. Chen, J. Wu, Y. Liu, X. Hu, D. Geng, Assemblage of Perovskite $LaNiO_3$ Connected With In Situ Grown Nitrogen-Doped Carbon Nanotubes as High-Performance Electrocatalyst for Oxygen Evolution Reaction, Phys. Status Solidi 215 (2018) 1800380.

[55] J. Gaudet, A. Tavares, a.S. Trasatti, D. Guay, Physicochemical characterization of mixed RuO_2– SnO_2 solid solutions, Chem. Mater. 17 (2005) 1570-1579.

[56] J.O.M. Bockris, T. Otagawa, The electrocatalysis of oxygen evolution on perovskites, J. Electrochem. Soc. 131 (1984) 290-302.

[57] H. Wang, W. Xu, S. Richins, K. Liaw, L. Yan, M. Zhou, H. Luo, Polymer-assisted approach to $LaCo_{1-x}Ni_xO_3$ network nanostructures as bifunctional oxygen electrocatalysts, Electrochim. Acta 296 (2019) 945-953.

[58] C. Wang, L. Zeng, W. Guo, C. Gong, J. Yang, Enhancing oxygen and hydrogen evolution activities of perovskite oxide $LaCoO_3$ via effective doping of platinum, RSC Adv. 9 (2019) 35646-35654.

[59] J. Bian, R. Su, Y. Yao, J. Wang, J. Zhou, F. Li, Z.L. Wang, C. Sun, Mg doped perovskite $LaNiO_3$ nanofibers as an efficient bifunctional catalyst for rechargeable zinc–air batteries, ACS Appl. Energy Mater. 2 (2019) 923-931.

[60] J. Zhang, S. Zhu, Y. Min, Q. Xu, Mn-doped perovskite-type oxide $LaFeO_3$ as highly active and durable bifunctional electrocatalysts for oxygen electrode reactions, Front. Mater. Sci. 14 (2020) 459-468.

[61] W. Li, Y. Yin, K. Xu, F. Li, K. Maliutina, Q. Wu, C. Li, B. Zhu, L.J. Fan, Enhancement of oxygen evolution activity of perovskite $(La_{0.8}Sr_{0.2})_{0.95}$ $MnO_{3-\delta}$ electrode by Co phase surface

modification, Catal. Today 364 (2021) 148-156.

[62] A. Sivanantham, P. Ganesan, L. Estevez, B.P. McGrail, R.K. Motkuri, S. Shanmugam, A stable graphitic, nanocarbon-encapsulated, cobalt-rich core-shell electrocatalyst as an oxygen electrode in a water electrolyzer, Adv. Energy Mater. 8 (2018) 1702838.

[63] T. Li, Y. Lv, J. Su, Y. Wang, Q. Yang, Y. Zhang, J. Zhou, L. Xu, D. Sun, Y. Tang, Anchoring $CoFe_2O_4$ nanoparticles on N-doped carbon nanofibers for high-performance oxygen evolution reaction, Adv. Sci. 4 (2017) 1700226.

[64] Z. Li, L. Lv, X. Ao, J.-G. Li, H. Sun, P. An, X. Xue, Y. Li, M. Liu, C. Wang, An effective method for enhancing oxygen evolution kinetics of $LaMO_3$ (M= Ni, Co, Mn) perovskite catalysts and its application to a rechargeable zinc–air battery, Appl. Catal. B 262 (2020) 118291.

[65] C. Su, W. Wang, Y. Chen, G. Yang, X. Xu, M.O. Tadé, Z. Shao, $SrCo_{0.9}Ti_{0.1}O_{3-\delta}$ as a new electrocatalyst for the oxygen evolution reaction in alkaline electrolyte with stable performance, ACS Appl. Mater. Interfaces 7 (2015) 17663-17670.

[66] L. Yang, T. Yang, Y. Chen, Y. Zheng, E. Wang, Z. Du, K.-C. Chou, X. Hou, FeNi LDH/V_2CT_x/NF as self-supported bifunctional electrocatalyst for highly effective overall water splitting, Nanomaterials 12 (2022) 2640.

[67] L. Yang, F. Ru, J. Shi, T. Yang, C. Guo, Y. Chen, E. Wang, Z. Du, K.-C. Chou, X. Hou, Trifunctional electrocatalysts based on feather-like NiCoP 3D architecture for hydrogen evolution, oxygen evolution, and urea oxidation reactions, Ceram. Int. 49 (2023) 659-668.

[68] Y. Jing, W. Li, D. Wang, X. Chang, M. He, Z.J. Ren, B-site regulated bimetallic

perovskite fluoride $NaCo_{1-x}Ni_xF_3$/reduced graphene oxide as the enhanced performance electrode material for supercapacitors, J. Alloy. Compd. 905 (2022) 164188.

[69] K. Lankauf, A. Mroziński, P. Błaszczak, K. Górnicka, J. Ignaczak, M. Łapiński, J. Karczewski, G. Cempura, P. Jasiński, S. Molin, The effect of Fe on chemical stability and oxygen evolution performance of high surface area $SrTi_{x-1}Fe_xO_{3-\delta}$ mixed ionic-electronic conductors in alkaline media, Int. J. Hydrog. Energy 46 (2021) 28575-28590.

Chapter IV:

Synthesis and electrochemical properties of zinc doping lanthanum cobaltite perovskite as an electrode material for hybrid supercapacitors

Chapter IV: Synthesis and electrochemical properties of zinc doping lanthanum cobaltite perovskite as an electrode material for hybrid supercapacitors

IV.1. Introduction

Increasing energy demand and depletion of fossil fuels have led researchers to focus on how to stock electricity from sustainable sources through efficient storage devices to overcome these crises **[1]**. In the last few years, supercapacitors have aroused extensive interest among the various energy storage devices, due to their high power density, quick charging and discharging times, and superior long cycle lifetime. These properties make them the perfect choice for bridging the void between traditional capacitors and batteries **[2]**. Despite these advantages, the practical utilization of supercapacitors remains hampered by their comparatively lower energy density **[3]**. An efficient approach for boosting supercapacitors' energy density is to construct hybrid supercapacitors consisting of a capacitive electrode (non-Faradaic) as a power source and a battery-type electrode (Faradaic) as an energy source **[4]**. This energy storage device can deliver a superior energy density over traditional capacitors and enhance the power density over batteries **[5]**. Furthermore, electrode materials have a significant impact on the supercapacitor performance; substantial research has been devoted for exploring efficient electrode materials that exhibit both high specific capacitance and long cycle stability **[6]**. As a result, transition metal oxides have gained preponderance due to a better electrochemical stability than conductive polymer materials and provide more energy density than conventional carbon materials **[7]**.

Perovskite oxides containing transition metals (ABO_3, where A denotes the alkaline and/or the rare earth metals and B the transition metal) are viewed as potential materials for supercapacitor electrodes because of their exceptional electronic structures, outstanding ionic conductivities and excellent thermal stability **[8]**. Among various lanthanum-based perovskite oxides ($LaMnO_3$, $LaNiO_3$, $LaFeO_3$, and so on), $LaCoO_3$ has been regarded as a promising and efficient material for supercapacitor electrodes because of multiple oxidation states of cobalt

atoms (Co^{2+}, Co^{3+}, and Co^{4+}), which supply excellent electrochemical redox properties **[9, 10]**. The existence of oxygen vacancies plays an essential role in improving the specific capacitance of electrode materials **[11]**. An effective strategy to improve the oxygen vacancies is either to dope the A and/or B sites which produces a change in the transition metal oxidation states , or to generate oxygen vacancies to compensate for the charge **[12]**. Proof can be found in previous studies, Lin and co-workers studied the impact of Sr doping on the specific capacitance of $La_xSr_{1-x}CoO_{3-\delta}$ **[13]**. The results demonstrated that as the amount of Sr increases, the amount of oxygen vacancies in the materials increases too, which causes the specific capacitance to increase from 320 to 747 $F.g^{-1}$. Likewise, R Mondal et al. **[14]** reported the electrochemical performances of $La_{1-x}K_xCoO_{3-\delta}$ with ($0 \leq x \leq 0.5$), where the $La_{0.5}K_{0.5}CoO_{3-\delta}$ electrode displays the best capacitance value of 378 $F.g^{-1}$. B. Zhang and colleagues have synthesized Sr-doped $LaNiO_{3-\delta}$ in which doping with 40% Sr^{2+} results in an increase in the capacitance value from 155.4 to 231.7 F. g^{-1} **[15]**. Similarly, the incorporation of 30% Sr^{2+} into $Bi_{1-x}Sr_xFeO_{3-\delta}$ exhibits the highest value of capacitance 1200 $F.g^{-1}$ **[16]**. Furthermore, the electrochemical behavior of $LaMn_{1-x}Ag_xO_{3-\delta}$ was reported by E. Abdel-Khalek et al **[17]**. They found that the specific capacitance achieves 80 $F.g^{-1}$ at x = 0.08 which is four times higher than x = 0 (23 $F.g^{-1}$). In addition, A. N Singh and co-workers investigated the partial replacement of yttrium with strontium in $Y_{1-x}Sr_xMnO_{3-\delta}$ perovskites in which the incorporation of Sr with x= 0.5 leads to the enhancement of the specific capacitance from 91 to 259 F. g^{-1} **[18]**. Besides, 15% Er-doped $ZnMnO_3$ nanoflake improved the specific capacitance of $ZnMnO_3$ from 866 to 1558 $F.g^{-1}$ **[19]**. Also, $SrTiO_3$ nanofibers doped with 30% Ce and $La(CoCrFeMnNiAl_x)_{1/(5+x)}$ O_3 doped with 50% Al enhance the specific capacitances, respectively, from 1650 to 2895 $mF.cm^{-2}$ **[20]** and from 281.84 to 353.65 F. g^{-1} **[21]**.

Zinc has been used as a dopant in several types of materials due to its ability to induce extrinsic defects **[22]**, as well as its critical role in improving the specific capacitance of supercapacitors. For instance, X. Qian et al. **[23]** studied the partial substitution effect of cobalt with zinc in the hollow $Zn_xCo_{3-x}S_4$. They found that the incorporation of Zn^{2+} by 30% almost doubles the capacitance value. Likewise, S.J. Uke and colleagues confirmed that zinc-doped $MgFe_2O_4$ nanocrystals exhibit the best specific capacitance value (484.6 F. g^{-1}), which is much greater compared to the undoped (375 $F.g^{-1}$) **[24]**. Similarly, J. Wu et al. **[25]** demonstrate that the introduction of Zn atoms into MnO_2 enhances the capacitance from 275 to 392 $F.g^{-1}$. In addition, a similar tendency was found when zinc was incorporated into $CoZn_{0.5}V_{1.5}O_4$ **[26]**.

The supercapacitor's energy density and long cycle life are other key factors. Considerable attention has been focused on improving them. Y. Qiao et al. **[27]** assembled a supercapacitor based on $SrFe_{0.85}Zr_{0.15}O_{3-\delta}$ cathode, the device provides a high energy density of 7.6 Wh kg^{-1} with capacitance retention of 67% over 5000 cycles. The characteristics of $ZnCo_2O_4$ nanosheets are found to be 34.6 Wh kg^{-1} with 93% retention after 3000 cycles **[28]** and for Hierarchical NiCo-LDH, they are 22.81 Wh kg^{-1} with 90.85% retention after 5000 cycles **[29]**. For $MoS_2@CoS_2$, the obtained values are 33.94 Wh kg^{-1} with 88.3% retention over 10000 cycles **[30]**. The values for MnO_2 are 37.92 Wh kg^{-1} with 97% retention after 10000 cycles **[31]**; while for the N-doped porous activated carbon, they are 21.5 Wh kg^{-1} with 90% retention over 25000 cycles **[32]**.

In this chapter, $LaCo_{1-x}$ Zn_xO_3 perovskite (x = 0, 0.03, 0.05 and 0.1, denoted as LCZ 00, LCZ 03, LCZ 05 and LCZ 10, respectively) has been synthesized via the sol-gel route and investigated to be a material for supercapacitor electrodes. The X-ray Diffraction (XRD), the FT-IR spectroscopy, the X-ray photoelectron spectroscopy (XPS), the scanning electron

microscopy (SEM) and the nitrogen adsorption-desorption techniques were used to study the physico-chemical properties of the prepared materials. While the electrochemical properties were examined by using cyclic voltammetry followed by charge-discharge, and then electrochemical impedance spectroscopy techniques.

IV.2. Experimental methods

IV.2.1. Preparation of $LaCo_{1-x}Zn_xO_3$ powder (LCZ)

The sol-gel technique was used to prepare a series of $LaCo_{1-x}Zn_xO_3$ perovskite with low zinc doping (x = 0, 0.03, 0.05 and 0.1). The technique is described in details in Chapter III.

IV.2.2. Electrochemical measurements

To yield the working electrodes, a sheet of nickel foam was cleaned in ethanol by sonication for 2 hours and then dried at 100 °C for 1 hour. As shown in Fig. IV. 1, a solid precursor of the LCZ or activated carbon (AC), the black carbon (BC) and the polyvinylidene-fluoride (PVDF) were mixed in an 80:10:10 weight ratio, respectively. The mixture was well-ground and sonicated with N-methyl pyrrolidone (NMP) for 24 hours to form a homogeneous slurry. The obtained slurry was coated onto the pre-treated nickel foam and dried for 24 hours at 80 °C.

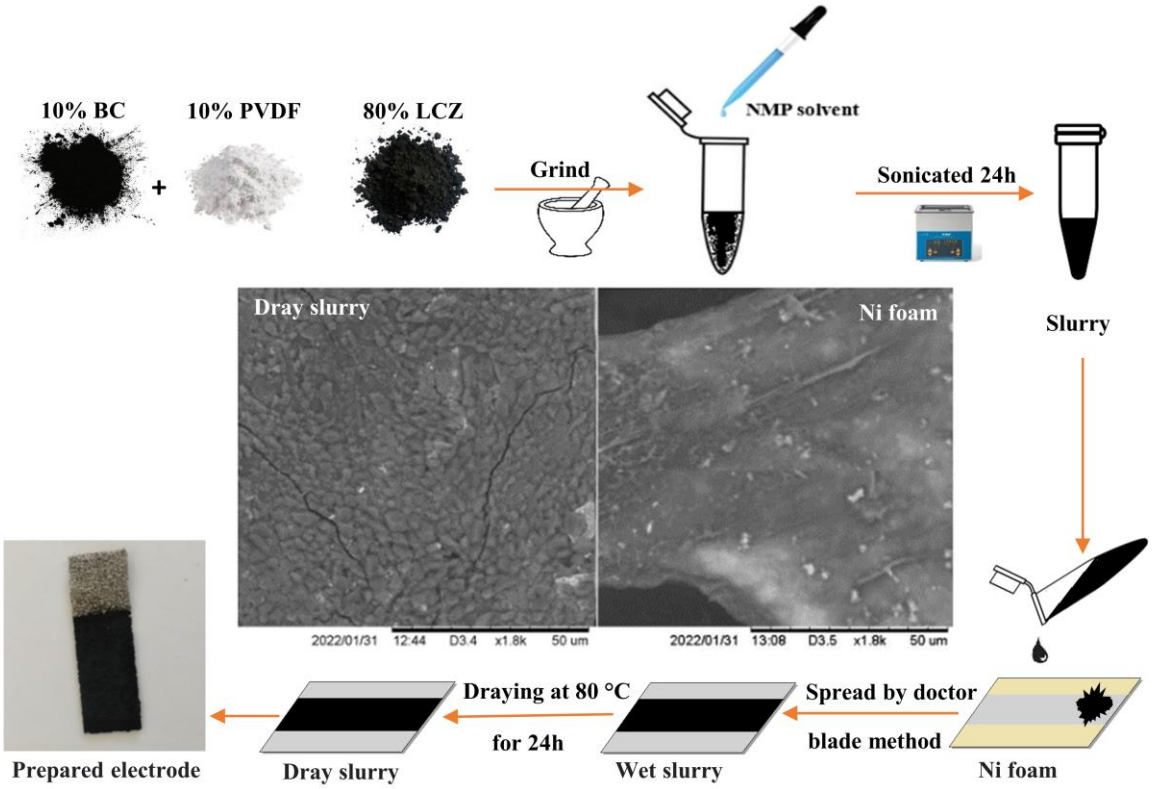

Fig. IV. 1. Schematic of LCZ electrodes preparation steps.

IV.3. Results and discussion

IV.3.1. Structural and morphological properties

X-ray diffraction was also used to study the low zinc doping impact on the $LaCoO_3$ structure. Fig. IV. 2 depicts the obtained XRD diffractograms of LCZ (00, 03, 05 and 10) calcined at 1100°C. The patterns are rather similar and exhibit a pure hexagonal perovskite structure, in which all the diffraction peaks could be indexed to $LaCoO_3$ hexagonal system (JCPDS card 98-016-7257). Furthermore, the diffraction peaks slightly shift to the lower 2θ values as the incorporated zinc amount increases, which is probably related to the substitution of the cobalt ions by the zinc ones. This finding is in agreement with a precedent report which demonstrates that the incorporation of zinc into $LaNiO_3$ perovskite shifts the peaks to a lower 2θ value **[33]**.

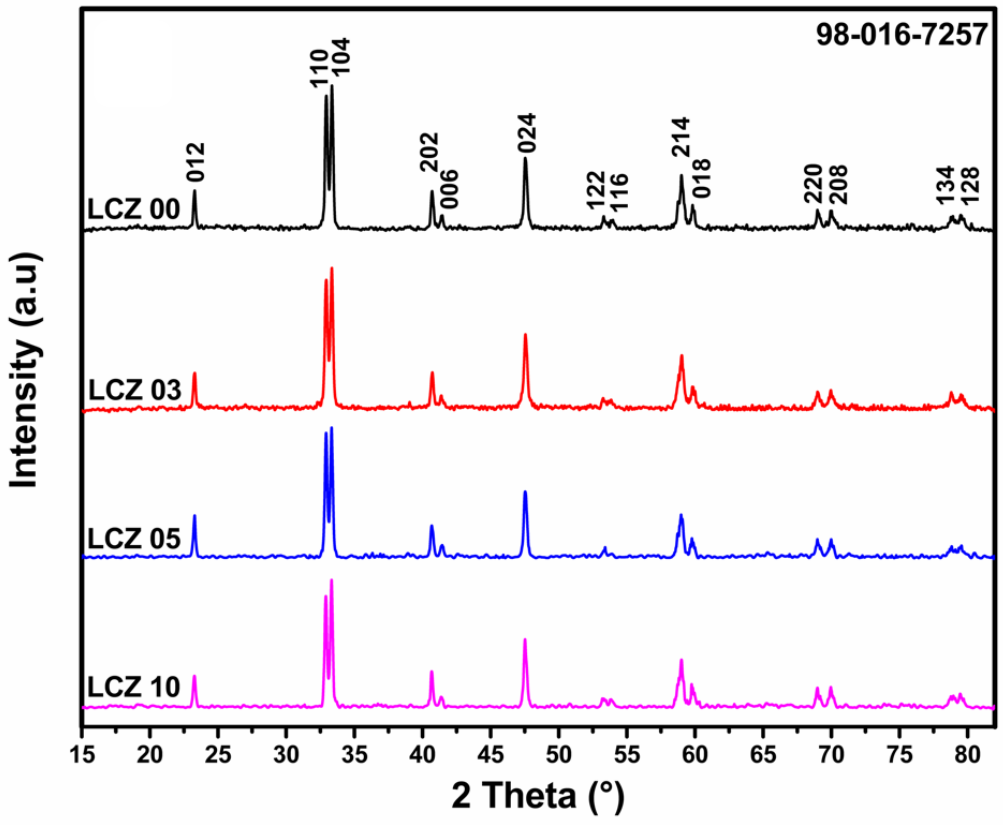

Fig. IV. 2. XRD patterns of LCZ 00, 03, 05 and 10 calcined at 1100 °C.

The lattice parameters values calculated using the Bragg's equation are listed in Table. IV. 1, indicating that the incorporation of zinc into $LaCoO_3$ leads the lattice parameters to increase which will certainly cause a swelling of the volume of the unit cell, such an increase is possibly due to the difference between the ionic radius of zinc (0.74Å) and cobalt (0.61Å). Similar trends have been previously found for $LaCr_{1-x}Zn_xO_3$ ceramics **[34]**. Furthermore, the average crystallite sizes determined by the Debye-Scherrer formula (Table. IV. 1) were evaluated from the peaks corresponding to the (104) and (110) planes. Such an increase confirms the replacement of cobalt ions with zinc ones in the $LaCoO_3$ lattice **[34]**.

Table. IV. 1. Cell parameters and crystallite sizes of LCZ powders.

Sample	LCZ 00	LCZ 03	LCZ 05	LCZ 10
2 Theta (110) (°)	32.9497	32.9392	32.9304	32.9094
2 Theta (104) (°)	33.3555	33.3410	33.3311	33.3248
FWHM (110) (°)	0.22771	0.22432	0.22066	0.21689
FWHM (104) (°)	0.22921	0.22424	0.21965	0.21113
d (110)	0.271620	0.271703	0.271775	0.271943
d (104)	0.268407	0.268520	0.268598	0.268647
a=b (Å)	5.4324	5.4340	5.4355	5.4388
c (Å)	13.0726	13.0788	13.0828	13.0834
V ($Å^3$)	334.099	334.466	334.742	335.14
D (nm)	36.28	36.95	37. 64	38.73

The infrared spectra of LCZ (00, 03, 05 and 10) calcined at 1100 °C for 6 hours are presented in Fig. IV. 3. The spectra are quite similar. The IR band found at 418 cm^{-1} might be ascribed to the La-O stretching vibration while the doublet absorption bands appearing at 560 and 595 cm^{-1} could be assigned, respectively, to the O-M-O bending vibration and the M-O stretching vibration of octahedral coordinated MO_6 (M=Co and/or Zn) **[35]**. The weak absorption bands appeared around 1642 and 1384 cm^{-1}, most likely corresponding to the vibrations of the LCZ perovskite crystal lattices as previously reported **[36]**. In addition, the sharp absorption bands located at about 2918 and 2875 cm^{-1} are probably assigned to the CH_2 and CH vibrations, whilst the broad absorption band appearing in the 3294-3653 cm^{-1} range is probably related to the O–H vibration of water molecule **[37]**. These results reconfirm the formation of the perovskite structure and support the results found in X-ray above.

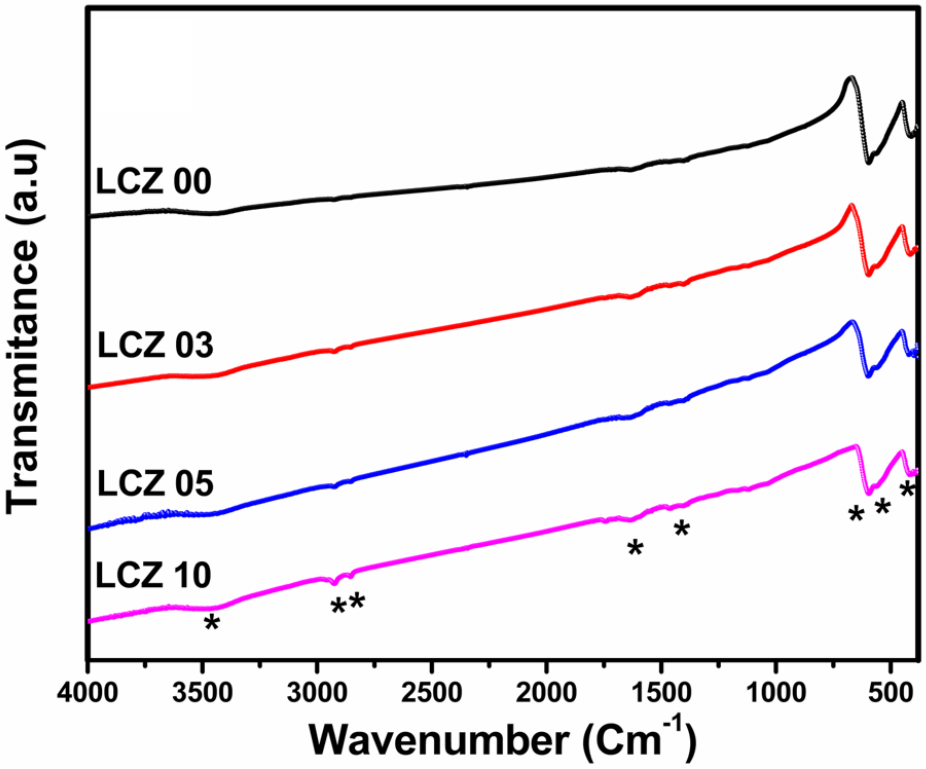

Fig. IV. 3. FT-IR spectra of LCZ powders.

The surface chemical composition of LCZ materials, as well as their valence states, were further investigated by using XPS analysis. As depicted in Fig. IV. 4, the full spectrum of the LCZ 05 sample reveals the existence of Oxygen, Lanthanum, Cobalt, Zinc and Carbon elements, demonstrating the purity of the prepared LCZ materials.

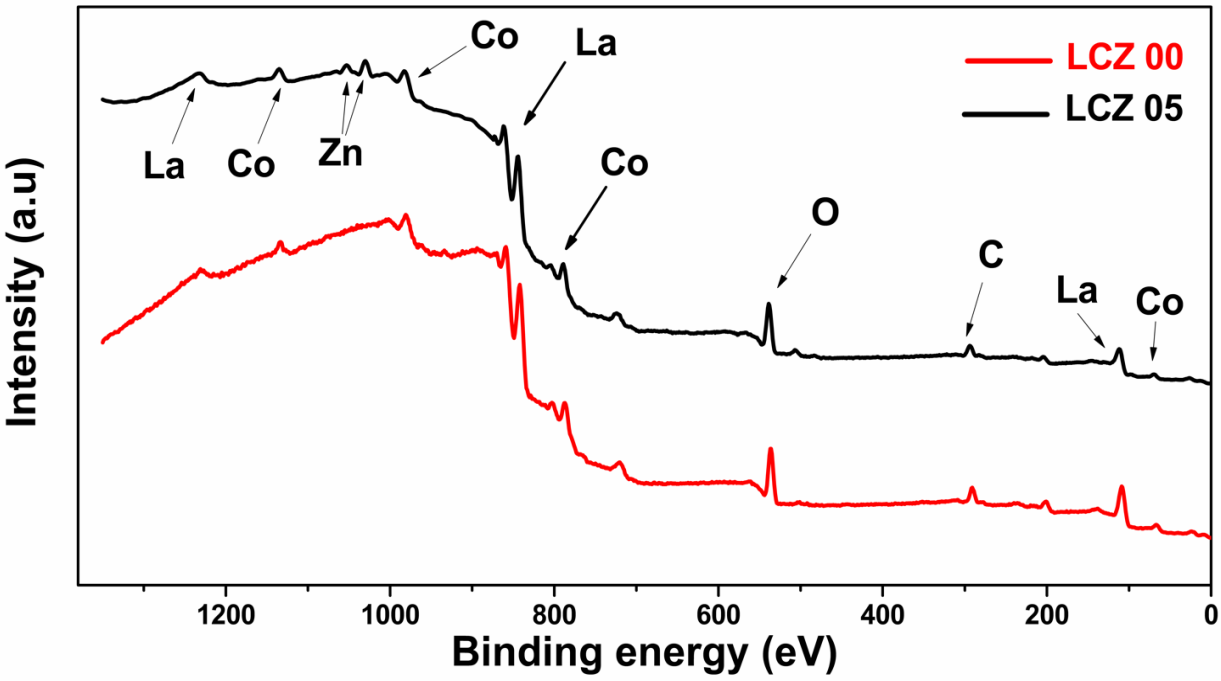

Fig. IV. 4. Survey spectra of LCZ 00 and LCZ 05.

The high-resolution Co 2p spectra of the LCZ 00 and LCZ 05 materials (Fig. IV. 5a and b) consist of two main characteristic spin-orbit peaks situated at about ~787.5 and ~802.5 eV for Cobalt $2p^{3/2}$ and Cobalt $2p^{1/2}$, where each spin-orbit peak can be deconvoluted into two secondary peaks. Moreover, these deconvoluted peaks located around ~785.5 and ~800.81 eV could be attributed to the Co^{3+} valence state whilst those located at about 789.54 and 803.28 eV can be ascribed to the Co^{2+} valence state **[13]**.

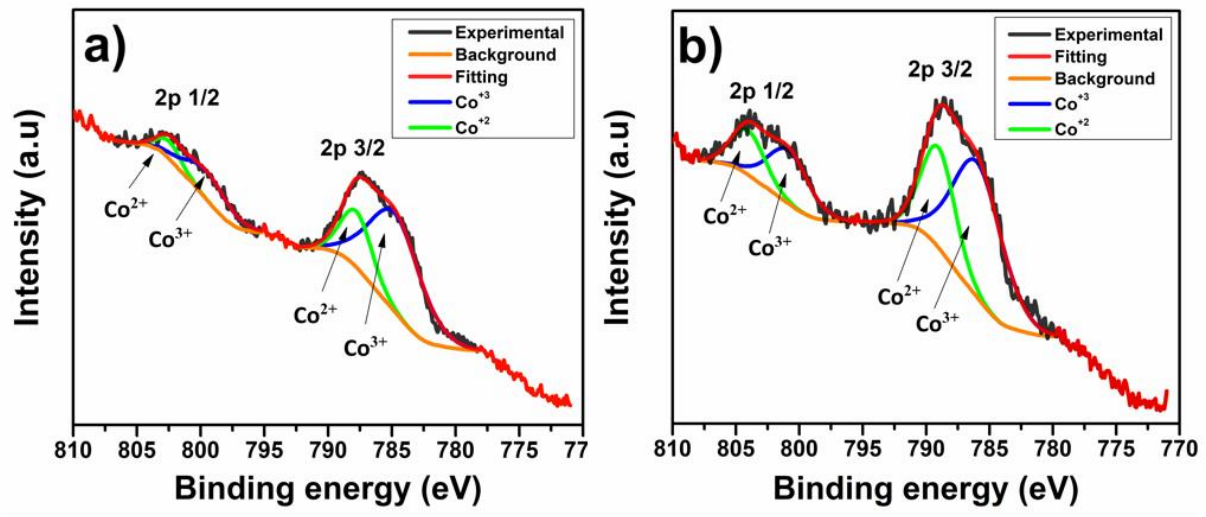

Fig. IV. 5. Co 2p XPS spectra of; a) LCZ 00 and b) LCZ 05.

The high-resolution O 1s spectra of the LCZ 00 and LCZ 05 materials (Fig. IV. 6a and b) were deconvoluted into four secondary peaks located approximately at 542.04, 540.41, 537.3, and 533.54 eV, which most likely correspond, respectively, to surface adsorbed H_2O, surface adsorbed oxygen or hydroxyl groups (-OH/O_2), highly oxidative oxygen species (O^{2-}/O^-) and surface lattice oxygen (O^{2-}) **[9, 38]**.

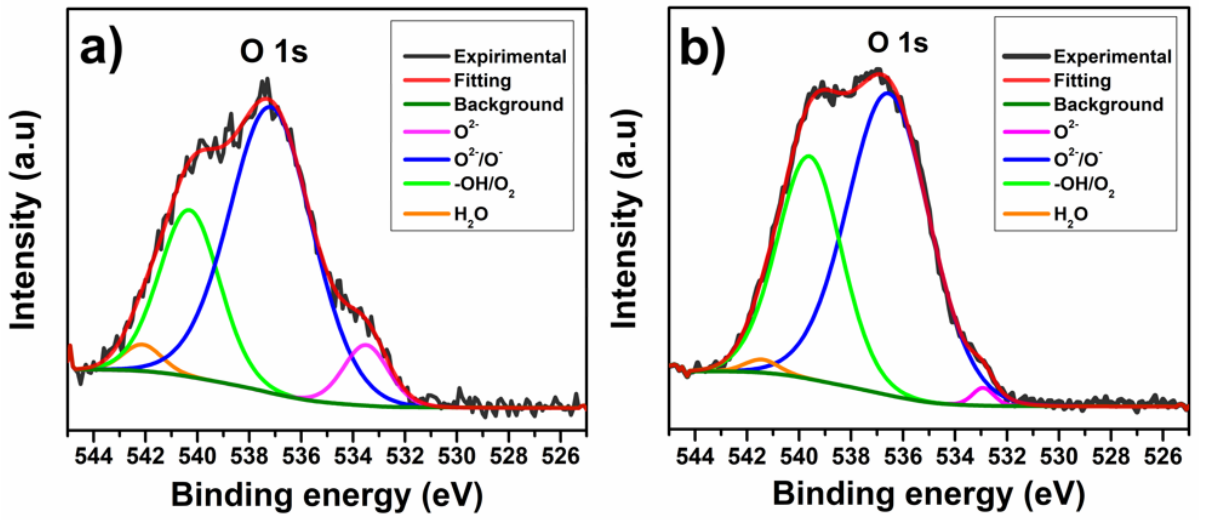

Fig. IV. 6. O 1s XPS spectra of; a) LCZ 00 and b) LCZ 05.

In fact, the partial replacement of trivalent Co^{3+} ions by divalent Zn^{2+} ions will produce a change in the transition metal valence state (Co^{3+} to Co^{4+}) and/or generate oxygen vacancies to neutralize the total charge in $LaCoO_3$. In addition, the vacancies of oxygen within the perovskite structure are directly related to the surface adsorbed oxygen molecules. As can be seen in Table. IV. 2, the increased relative area of (-OH/O_2) and (Co^{2+}) peaks indicates that the substitution of Zn into $LaCoO_3$ materials resulted in the formation of oxygen vacancies [$La(Co_{2\delta}^{2+}, Co_{1-2\delta}^{3+}) O_{3-\delta}$].

Table. IV. 2. Relative concentrations of Co 2p and O 1s in LCZ 00 and LCZ 05.

Sample	LCZ 00 (%)	LCZ 05 (%)
O^{2-}	7.28	0.96
O^{2-}/O^{-}	63.23	62.14
-OH/O_2	26.78	35.8
H_2O	2.71	1.1
Co^{2+}	25.39	35.21
Co^{3+}	74.61	64.79

The surface morphology of the LCZ perovskite samples obtained at 1100 °C was scanned by SEM, as can be seen in Fig. IV. 7a-d. It is interesting to notice that the features of the surface of the samples are almost identical and the texture of the surface consists of distinct polycrystalline particles with well-defined boundaries of different shapes and sizes. This could be ascribed to the high calcination temperature, where it was found that as the calcination temperature increases, the small grains approach each other and merge into larger grains **[39]**. In addition, the pristine LCZ 00 ceramic shows the larger grains than the doped ceramics, indicating that the substitution of cobalt with zinc into $LaCoO_3$ is effective in

repressing the grain growth, similar behavior has been found previously when nickel was substituted into $LaCoO_3$ **[40]**. Unfortunately, the formation of polycrystalline with boundaries may reduce the rate capability at high current densities and scan rates and lengthen the ion diffusion path **[41]**.

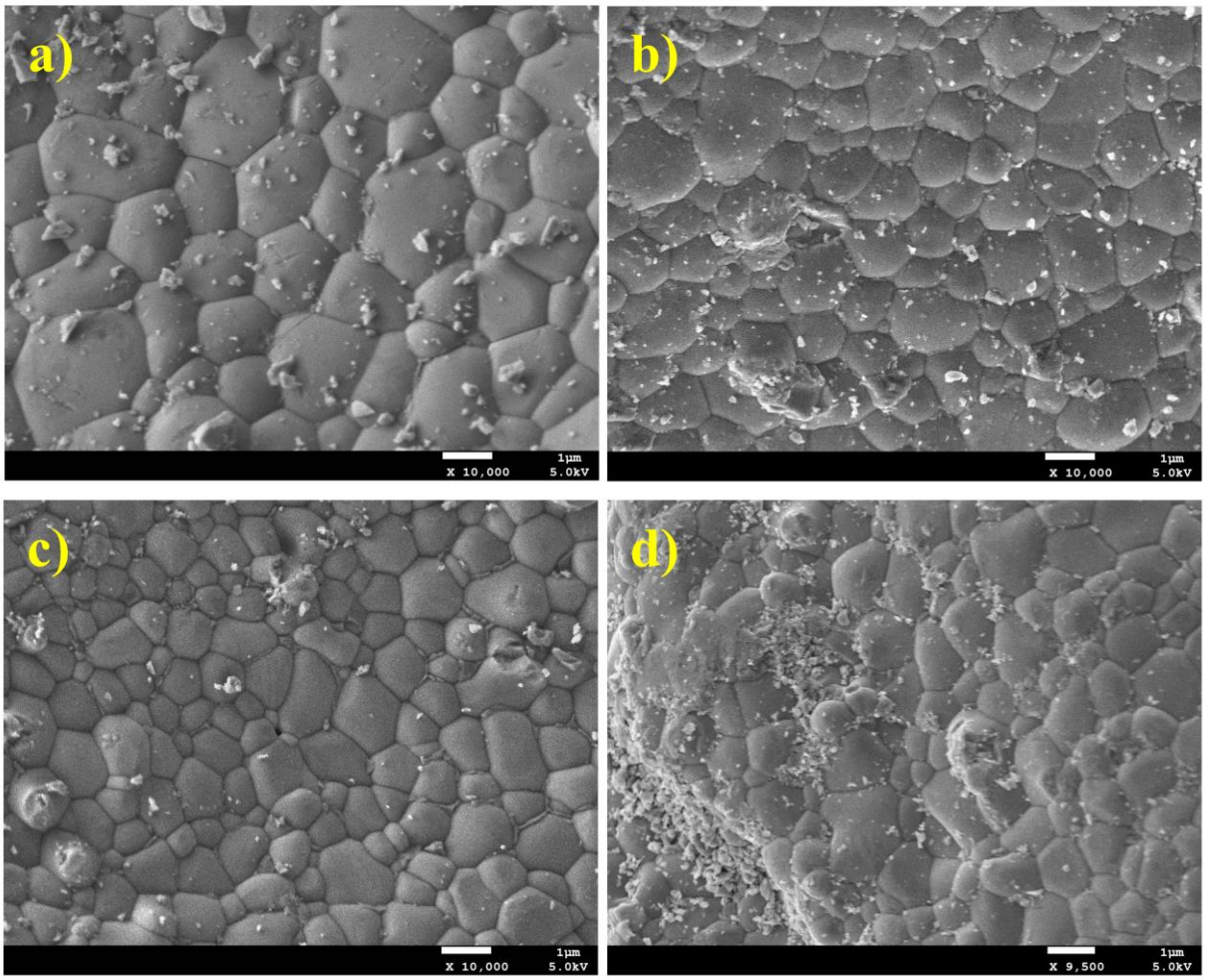

Fig. IV. 7. SEM micrographs of; a) LCZ 00, b) LCZ 03, c) LCZ 05 and d) LCZ 10.

The Nitrogen adsorption-desorption analysis was performed to further estimate the pore diameters and the specific surface of the LCZ perovskite powders. The results are given in Fig. IV. 8 and listed in Table. IV. 3. According to the International Union of Pure and Applied Chemistry (IUPAC) classification, the LCZ samples exhibit a typical IV isotherm with H4-type hysteresis loops, demonstrating the mesoporous characteristics of LCZ materials (pore diameters ranging from 3.8 to 7.19 nm) and the narrow slit-like pores **[42]**.

The specific surface area increases slightly with increasing incorporated zinc amount and then decreases for the LCZ 10 sample. Such change could be attributed to the decrease and then the increase of the particle size observed in the SEM analysis above. Additionally, the highest values of pore volume and diameter as well as the specific surface of LCZ 05 sample can facilitate the diffusion of ions from the electrolyte within the electrode material with reduced resistance and can also enhance the electrode-electrolyte interface to supply further electroactive sites to boost the electrochemical performance **[43]**.

Table. IV. 3. The specific surface area, pore size, and pore volume of LCZ 00, 03, 05, and 10.

Sample	Specific surface ($m^2.g^{-1}$)	Pore diameter (nm)	Pore volume ($10^{-3}.cm^3.g^{-1}$)
LCZ 00	2.2207	4.74	3.70
LCZ 03	2.2475	4,72	4.21
LCZ 05	2.6499	7.19	4.75
LCZ 10	2.3417	3.80	3.47

Unusually, the hysteresis loops of the adsorption-desorption isotherms remain open even at a lower relative pressure, most likely due to the weaker outgassing temperature, i.e., the adsorbed molecule cannot be fully extracted during the desorption process. This phenomenon can be explained by the non-reversible uptake of molecules into pores or through the inlets which have a width similar to that of the adsorbate molecules. It can also be caused by the non-rigid porous structure swelling or by the irreversible chemical reaction between adsorbate and adsorbent **[42]**.

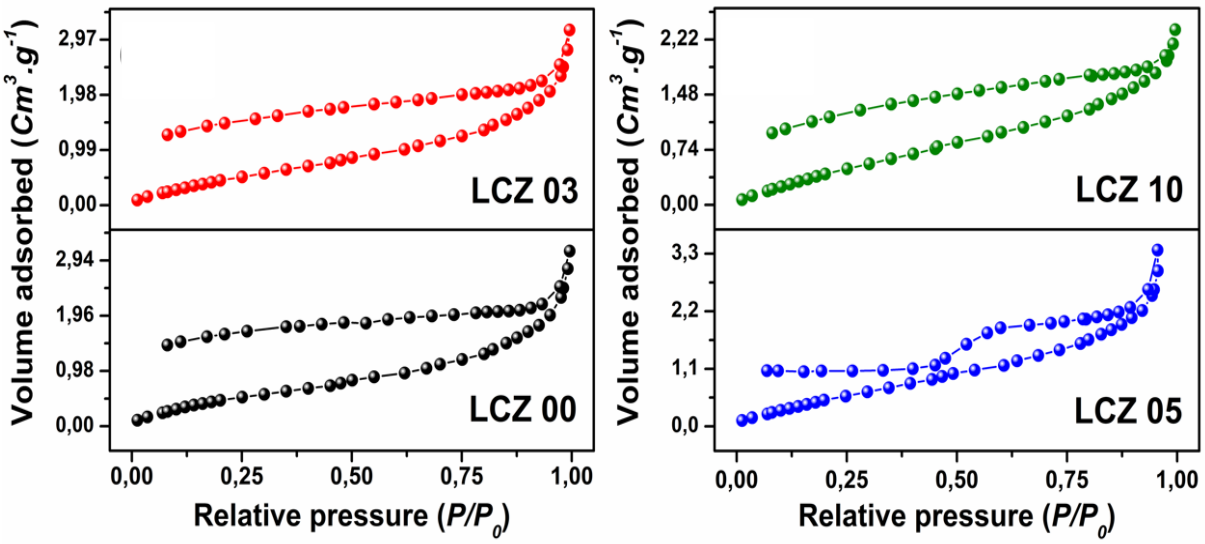

Fig. IV. 8. N_2 adsorption-desorption isotherms of LCZ powders.

IV.3.2. Electrochemical performance

Cyclic voltammetry (CV) was realized to assess the storage mechanism of the synthesized electrodes. Fig. IV. 9 displays the cyclic voltammograms of LCZ (00, 03, 05 and 10) electrodes recorded at a sweep rate of 10 $mV.s^{-1}$, across a potential working window of -0.05 to 0.45 V, in an aqueous solution of 1M KOH. The obtained CVs curves have a similar form and clearly reveal the existence of redox peaks, indicating that the LCZ electrodes have a battery-type behavior. Furthermore, the two pairs of the obvious redox peaks may be ascribed to the reversible Faradic reaction associated with the (Co^{3+}/Co^{2+}) and (Co^{4+}/Co^{3+}) couples **[12, 44].**

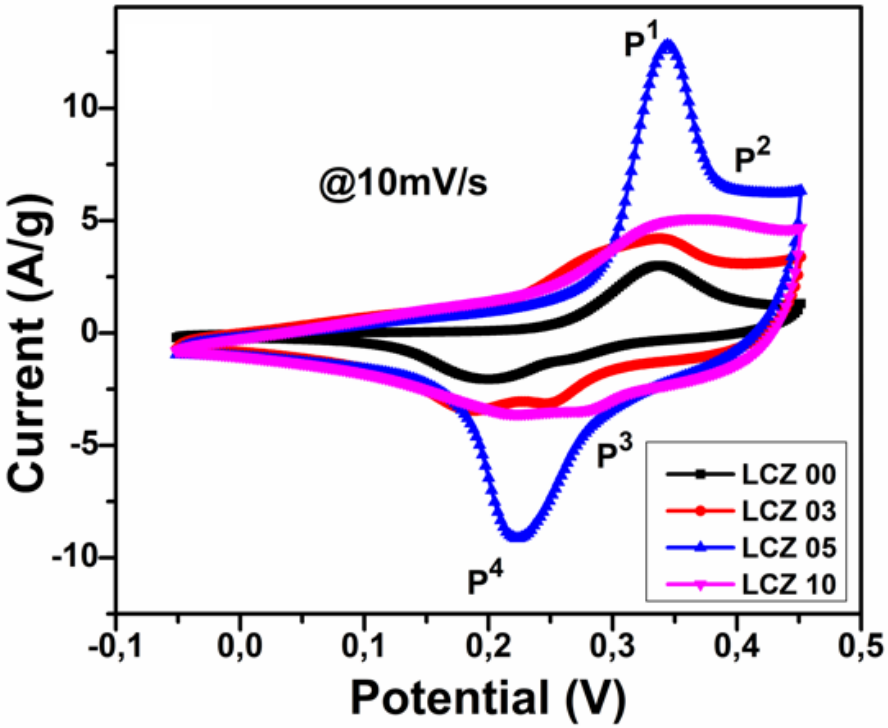

Fig. IV. 9. CV curves of LCZ electrodes performed at a constant sweep rate of 10 $mV.s^{-1}$.

Based on the CV and the XPS results above, and also previous literature **[12, 45, 46]**, we may infer that the electrochemical storage mechanism of LCZ perovskite in alkaline electrolyte could be regarded as an intercalation of oxygen ion mediated by the oxidation of cobalt atom, which can be expressed by Eqs. **IV.1** and **IV.2**, and illustrated in Fig. IV. 10.

$$La[Co^{2+}_{2\delta}, Co^{3+}_{1-2\delta}]O_{3-\delta} + 2\delta OH^- \rightleftharpoons LaCo^{3+}O_3 + 2\delta e^- + \delta H_2O \qquad (\mathbf{IV.1})$$

$$LaCo^{3+}O_3 + 2\delta OH^- \rightleftharpoons La[Co^{4+}_{2\delta}, Co^{3+}_{1-2\delta}]O_{3+\delta} + 2\delta e^- + \delta H_2O \qquad (\mathbf{IV.2})$$

As shown in Fig. IV. 10 and Eq. (IV.1), the OH^- ions adsorbed on the perovskite surface will intercalate to the oxygen vacancies by leaving a proton H^+, where it associates with another OH^- to produce H_2O. While the diffusion of O^{2-} ions along the octahedral edges of the unit cell fills the oxygen vacancies; this leads to the oxidation of two Co^{2+} to two Co^{3+} states per one oxygen ion intercalation. Then in the next reaction described in Eq. (IV.2), the excess of oxygen ions is intercalated to the surface thru the diffusion of cobalt center to the surface accompanied by the oxidation of two Co^{3+} atoms into two Co^{4+} states. These results suggest that the LCZ 05 electrode has more oxygen vacancies and support the XPS finding results. Moreover, the integrated areas of the CVs curves are 0.67, 1.68, 2.69 and 2.04 for LCZ 00, 03, 05 and 10 respectively. This proves that the LCZ 05 electrode possesses the highest specific capacitance **[13]**. These results indicate that the partial substitution of cobalt ions by zinc has a beneficial impact on enhancing the electrochemical performance via the creation of oxygen vacancies.

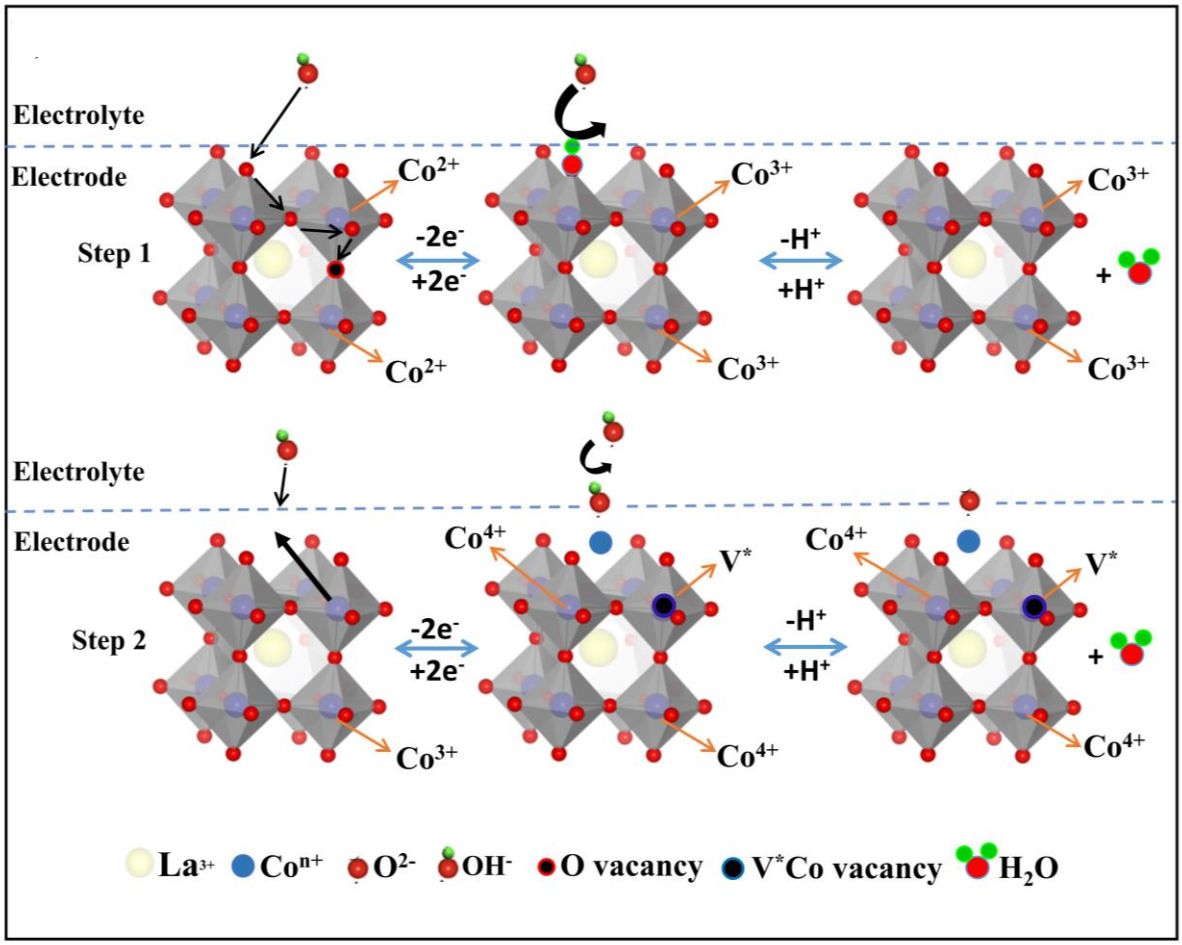

Fig. IV. 10. Mechanism of oxygen intercalation into LCZ electrode materials in alkaline electrolyte.

Fig. IV. 11 exhibits the cyclic voltammograms of the LCZ electrodes measured at several sweep rates ranging from 2 to 100 $mV.s^{-1}$ over a potential working window of -0.05 to 0.45V. A pair of redox peaks are seen in the first two sweep rates (2 and 5 $mV.s^{-1}$). Whereas, as the sweep rate hikes up to 100 $mV.s^{-1}$, the peaks of both anodic and cathodic branches have fused into one broad anodic and cathodic peak. Moreover, increasing scan rate leads the current density to increase, and the potential position of the redox peaks to shift without any noticeable change in the shape of the graph. The positions of the oxidation peaks are shifted to a higher potential, while the reduction peaks shift to a lower potential (the obtained values are

listed in Table. IV. 4). These results indicate that the LCZ electrodes have a good rate capability and low polarization **[47, 48]**.

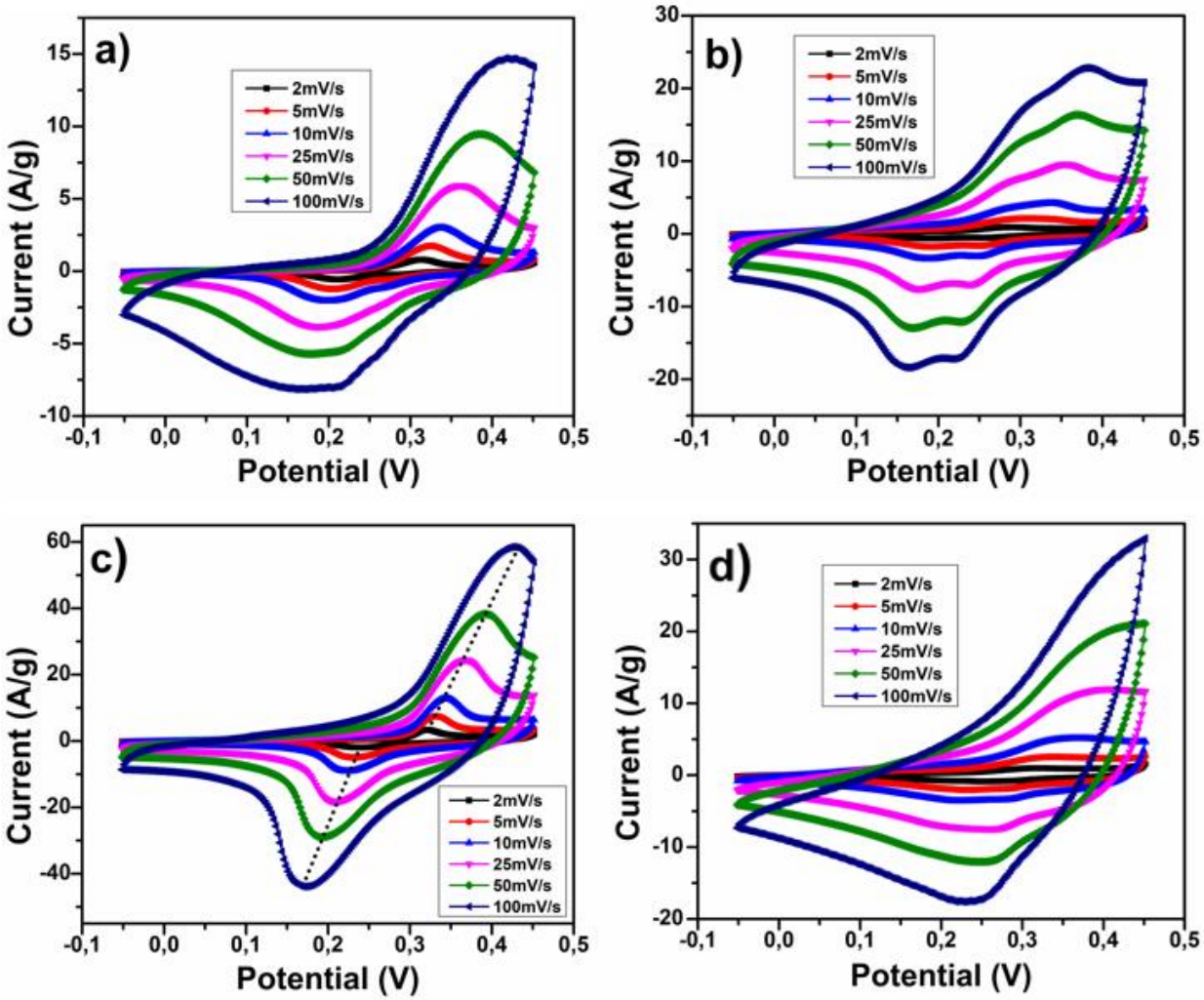

Fig. IV. 11. CV curves of LCZ electrodes measured at different sweep rates (2-100 $mV.s^{-1}$); a) LCZ 00, b) LCZ 03, d) LCZ 05 and d) LCZ 10.

To further understand the kinetics as well as the storage mechanism of the LCZ electrodes, the data of the CV were analyzed, at different scan rates, based on the power's law equation (**IV.3**) **[49, 50]**.

$$i_p(V) = a.v^b \qquad \textbf{(IV.3)}$$

where, i is the current density, (a) and (b) are adjustable parameters and v the sweep rate.

The value of b can be obtained from the slop of the (log i_p) - (log v) plot. When b = 0.5, it can be inferred that the electrode material storage mechanism is a completely diffusion-controlled one. Whereas, b = 1 corresponds to the complete capacitive-controlled processes. As illustrated in Fig. IV. 12 and Table. IV. 4, the obtained b values of the anodic and cathodic peaks demonstrate that the process of reaction of LCZ electrodes is a mixture of both diffusion and capacitive-controlled processes **[50]**.

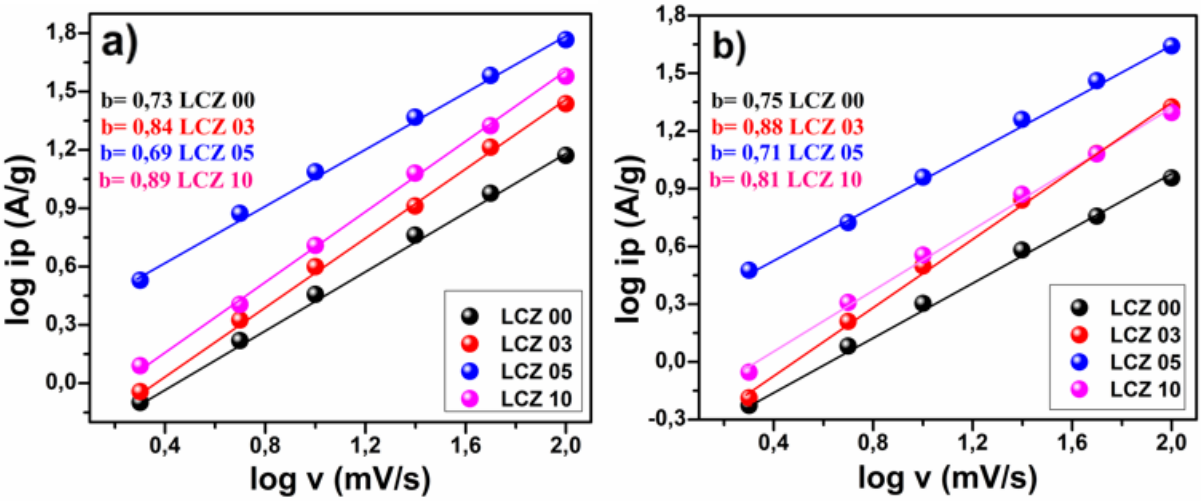

Fig. IV. 12. Relationship log (peak current) and log (sweep rate).

Table. IV. 4. The oxidation, reduction peaks shift and b values of the LCZ electrodes.

Electrode	Oxidation peaks shift (mV)	Reduction peaks shift (mV)	Anodic b value	Cathodic b value
LCZ 00	105	39	0.73	0.75
LCZ 03	92	95	0.84	0.88
LCZ 05	108	69	0.69	0.71
LCZ 10	134	24	0.89	0.81

The specific capacitance of the LCZ electrodes, determined from the CV profiles, as a function of the sweep rates (2-100 $mV.s^{-1}$) is illustrated in Fig. IV. 13. The highest specific capacitance values are achieved at a lower sweep rate and then start to decrease with increasing scanning rate up to 100 $mV.s^{-1}$. This is probably due to the fact that electrolyte species at faster scan rates have no optimum time to permeate into the active site and to complete the reaction process **[51]**. The values of the specific capacitance obtained at 2 and 100 $mV.s^{-1}$ are listed in Table. IV. 5. These results suggest that the LCZ 05 electrode has the highest specific capacitance and a moderate capacitance retention.

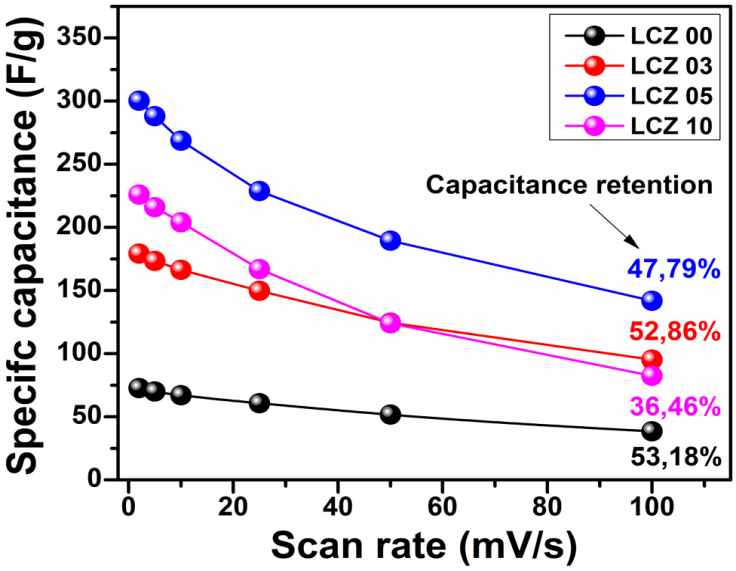

Fig. IV. 13. Specific capacitance vs. sweep rates determined from the CV curves.

Table. IV. 5. The specific capacitance and retention obtained from CV and GCD curves.

Electrode	C_s at (2 $mV.s^{-1}$) (F/g)	Cs retention (%) at (100 $mV.s^{-1}$)	C_s at (0.5A/g) (F/g)	Cs retention (%) at (5A/g)
LCZ 00	72.37	53.18	78.02	81.56
LCZ 03	179.12	52.86	194.87	81.11
LCZ 05	300.29	47.79	315.15	78.40
LCZ 10	226	36.46	238.01	71.48

Galvanostatic charge-discharge (GCD) was implemented to further explore the properties of energy storage of the synthesized electrodes. Fig. IV. 14 represents the comparative GCD curves of LCZ electrode materials measured at a constant current density of 1A/g within a potential working window, -0.05 to 0.45 V, in 1M KOH. The charge-discharge curves show a non-linear behavior, indicating a battery-type nature of the LCZ electrodes. In addition, the presence of a potential plateau on both charging and discharging curves inevitably signifies the existence of faradaic redox reactions **[52, 53]**. Moreover, the partial substitution of Co by Zn increases the charge-discharge time, where the highest is observed for LCZ 05 followed by LCZ 10, 03 and 00 respectively. This means that the partial incorporation of zinc into $LaCoO_3$ enhances the ionic conductivity and provides a higher specific capacitance. A similar tendency was found when Fe was incorporated into $La_{0,7}Sr_{0,3}Mn_{1-x}Fe_xO_3$ **[54]**. Furthermore, a potential drop (IR) at the beginning of the discharge curves has been observed, in which LCZ 05 shows the minimum value, suggesting that LCZ 05 has a low internal resistance **[55]**.

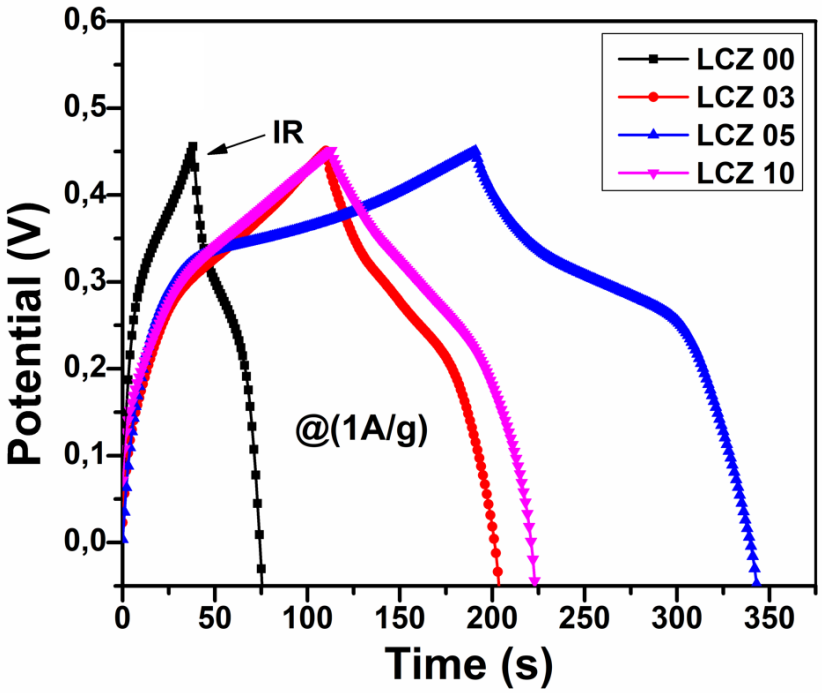

Fig. IV. 14. GCD curves of LCZ at a constant current density of 1 A/g.

GCD measurements were also carried out at various current densities (0.5 to 5 A/g), over a potential window of -0.05 to0.45V. As demonstrated in Fig. IV. 15, the LCZ electrodes clearly display battery-type behavior, which corresponds well to the CVs analysis. The charge-discharge curves kept in shape as the current density increased, suggesting that the LCZ electrodes are ideally suited for use as a supercapacitor electrode **[5]**. Besides, distinct potential plateaus are observed, proving the presence of oxidation-reduction reactions **[53]**.

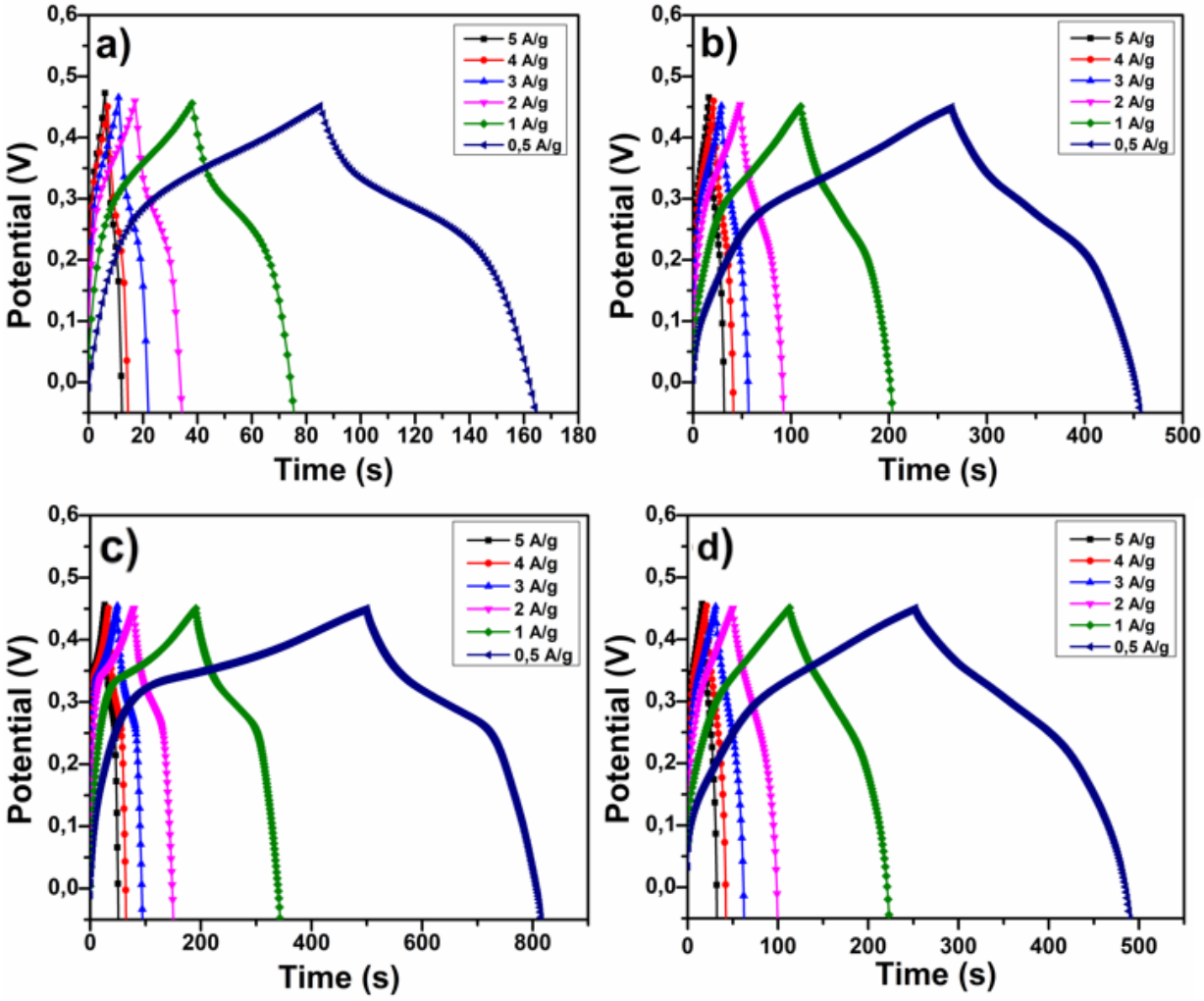

Fig. IV. 15. GCD curves recorded at different current densities; a) LCZ 00, b) LCZ 03, d) LCZ 05 and d) LCZ 10.

The increased current density leads to the reduction of both the charge and discharge time and to the increase of the potential drop (IR). This is possibly explained by the fact that, at weaker current density, the electrolyte species have optimum time to intercalate into the active surface of the electrode and complete the faradaic reaction **[11, 56]**. Specifically, the LCZ 05 electrode shows a longer discharge time, as well as lower IR values at all current densities, which implies the capability to provide more specific capacitance, a better conductance of the charge transport and a reduced internal resistance **[56]**.

The calculated specific capacitance from the GCD curves versus several current densities (0.5 to 5 A/g) is presented in Fig. IV. 16. As expected, the highest specific capacitance values are achieved at a lower current density and then gradually reduce with increasing current density up to 5 A/g. This behavior can be explained by the fact that at higher current densities, oxygen ion does not have adequate time to permeate into the active site of the electrode material and intercalate in the oxygen vacancies **[57]**. Particularly, the values of the specific capacitance obtained at 0.5 and 5A/g, are illustrated above in Table. IV. 5, thus revealing the good rate capability of the LCZ electrodes **[52]**. It is worth mentioning that the capacitance values obtained from GCD graphs at 1 A/g are compatible with the estimated values from the CV at 2 $mV.s^{-1}$. These results agree well with the above CV results and reconfirm that the LCZ 05 electrode has the largest specific capacitance and a moderate capacitance retention.

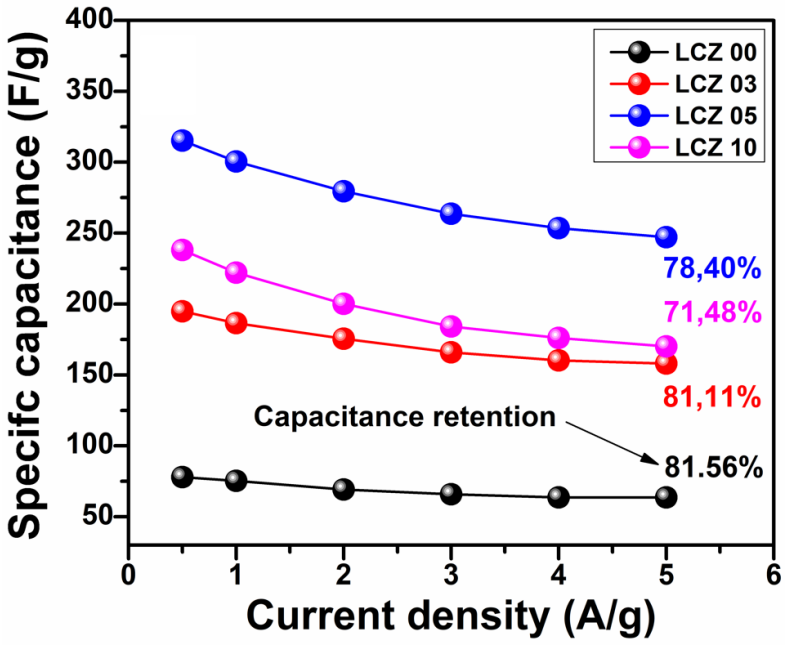

Fig. IV. 16. Specific capacitance vs. current density determined from the GCD curves.

Electrochemical Impedance Spectroscopy was implemented to obtain a better assessment of the conductivity, to deeper understand the charge transfer kinetics, and to describe the ions diffusion process at the interface (electrode-electrolyte) during the process of charge and discharge. Fig. IV. 17 illustrate the Nyquist impedance with the corresponding fitted spectra of the LCZ electrodes recorded at open circuit potential (OCP) with an amplitude of 10 mV, within a frequency range of 100 kHz to 10 mHz. The equivalent circuit for adjusting the impedance parameters is presented in inset of Fig. IV. 17 and the calculated values using EC-Lab software are summarized in Table. IV. 6, where R_S, R_{ct}, W_s, Q_{dl}, and Q_f represent respectively the internal resistance, the resistance of charge transfer, the Warburg element, the double-layer capacitance, and the faradaic capacitance (a constant phase element (CPE) was used due to the non-ideality of the two capacitances of real systems). The Nyquist plot could be divided into three parts; the high-frequency region where the curves begin, the interception between the spectrum and the real impedance axis (Z') involves the internal resistance (R_S),

which comprise the electrolyte's ionic resistance, the active material intrinsic resistance and the interfacial contact (electrode-electrolyte) resistance **[12]**. Obviously, the LCZ 05 electrode exhibits the lowest R_S value (0.907 $\Omega.cm^{-2}$) indicating a lower internal resistance, i.e., the improved electronic conductivity **[58]**, which is consistent with the lower IR drop found in the previous GCD analysis. In the mid-frequency region, the presence of a semicircle is produced by a double-layer capacitance (Q_{dl}) in parallel with an interfacial charge transfer resistance (R_{ct}). Clearly, the LCZ 05 electrode reveals the lowest R_{ct} value (2.106 $\Omega. cm^{-2}$) as well as the highest Q_{dl} value (0.005468 F. $s^{n-1}.cm^{-2}$) compared to the other electrodes. This elucidates both the excellent electrochemical activity (i.e., the interfacial charge transfer process becomes much easier) as well as the larger electrode-electrolyte interface area **[59]**, which is consistent with the specific surface results. The inclined part of the semicircle towards the low-frequency region reveals the Warburg impedance, which is an outcome of the diffusion of ions, where more important slope means a lower diffusion resistance **[60]**. Distinctly, the slope of the slant line of the LCZ 05 electrode is the largest, followed by that of LCZ 10, LCZ 03 and LCZ 00, indicating the improved electrochemical capacitive behavior and a reduced diffusion resistance (0.648 $\Omega. s^{(-1/2)}.cm^2$) **[58]**. This is probably due to a large amount of intercalated oxygen **[61]**, thus leading to the higher faradic capacitance (0.06896 $F.s^{n-1}.cm^{-2}$) **[59]**. This finding is well consistent with the previous CV and GCD results, which clearly confirm that the substitution of cobalt with an appropriate zinc amount significantly improves the electronic conductivity and the electrode-electrolyte interface area and reduces the interfacial charge transfer resistance as well as the ions diffusion resistance of $LaCoO_3$ perovskite.

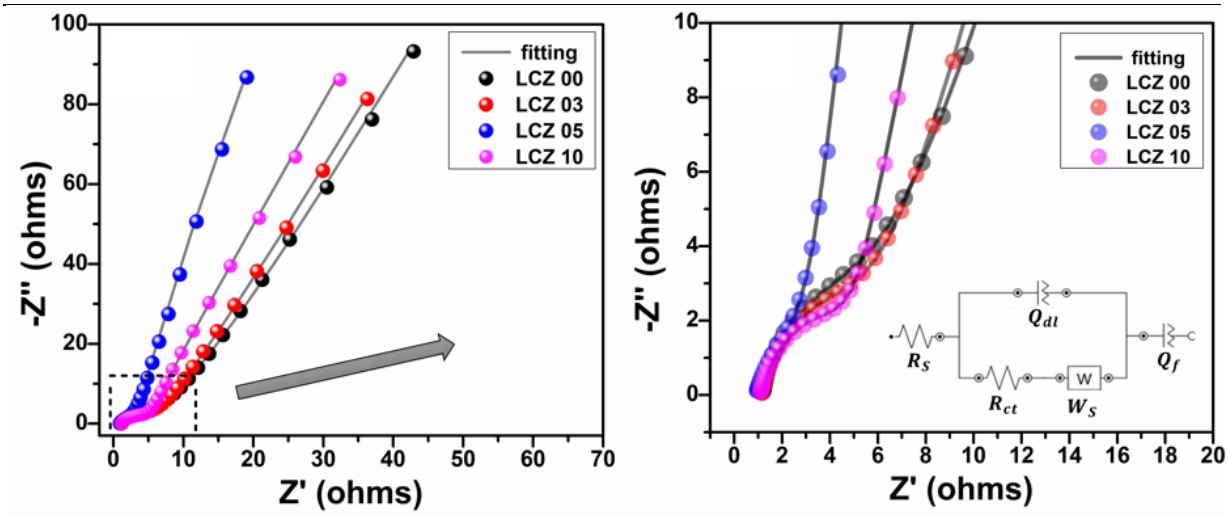

Fig. IV. 17. Comparative EIS spectra of LCZ electrode measured at open circuit potential in the frequency range from 10 mHz to 100 kHz.

Table. IV. 6. Electrochemical parameters from EIS-Nyquist plot of LCZ electrodes obtained by fitting EIS with an equivalent circuit model (X^2 =0.9 10^{-3}).

Electrode	R_s ($\Omega.cm^{-2}$)	R_{ct} ($\Omega.cm^{-2}$)	Q_{dl} ($F.s^{n-1}.cm^{-2}$)	n_{dl}	δ_{Ws} ($\Omega.s^{-1/2}$)	Q_f ($F.s^{n-1}.cm^{-2}$)	n_f
LCZ 00	1.184	4.557	0.001366	0.865	16.21	0.01862	0.811
LCZ 03	1.159	4.454	0.001511	0.836	9.461	0.02502	0.820
LCZ 05	0.907	2.106	0.005468	0.751	0.648	0.06896	0.879
LCZ 10	1.103	3.613	0.003193	0.803	3.558	0.03489	0.841
LCZ 05*	1.227	12.39	0.003448	0.857	8.504	0.02679	0.799

LCZ 05*; after 5000 cycles.

The long-term cycle stability and the coulombic efficiency are significant factors in determining the practical applicability of electrode materials for supercapacitors. We have conducted 5000 successive charge and discharge cycles between -0.05 and 0.45V at a constant current density (5 A/g) to evaluate the cycling stability and the coulombic efficiency of the LCZ 05 electrode material. The results are given in Fig. IV. 18. Obviously, the specific capacitance starts to increase quickly up to the 50th cycle, achieving 103.33% of the initial specific capacitance. This behavior could be imputed to the activation process of the electrode material (i.e. increased electroactive sites), thus resulting in the enhancements of the capacitance **[62]**. Beyond the 50th cycle, the specific capacitance begins to gradually decline, retaining approximately 85.73% of its original capacitance at the 5000th cycle. This phenomenon could be explained by the fact that filling vacancies with oxygen ions from the electrolyte during the charging process cannot be fully extracted during the discharging process; This means that the number of oxygen ions intercalated decreases with the increasing cycle number **[57]**. In addition, the initial charge capacitance is greater than the discharge capacitance, leading to a coulombic efficiency of 95.15%. This is consistent with the CV and GCD analyses above, where the oxidation current was higher than the reduction current and the charge time was longer than the discharge time. Afterward, the charging and discharging capacitances become almost identical, causing the coulombic efficiency to reach 98.81% at the 5000th cycle, suggesting that the Faradic reactions become more reversible (i.e., the ratio of intercalated/deintercalated oxygen ions is close to 1) **[62]**. This finding demonstrates the excellent cyclic durability as well as the good rate performance of the LCZ 05 electrode.

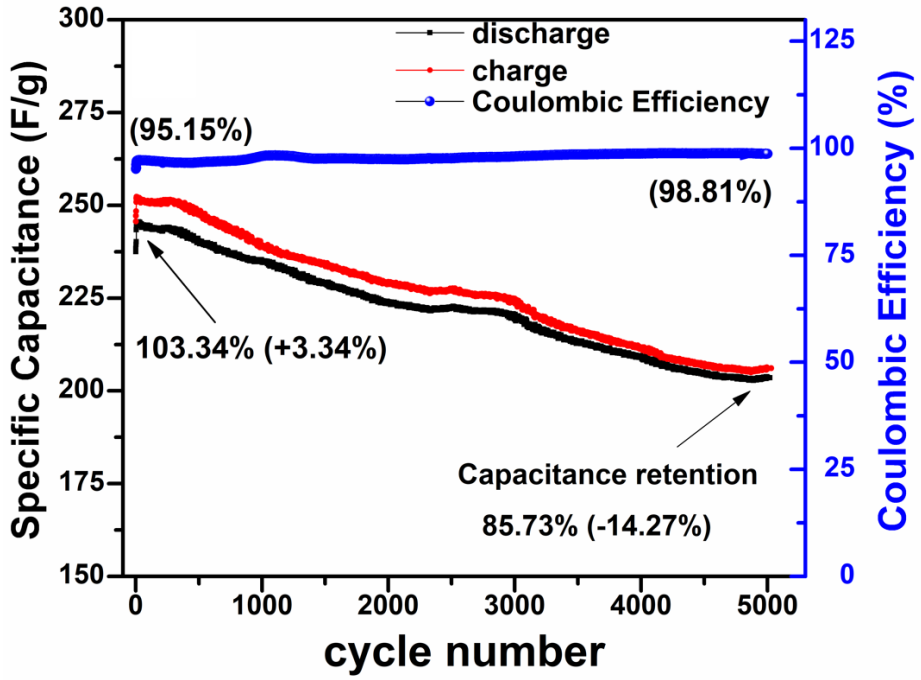

Fig. IV. 18. Cycling performance of LCZ 05 measured at a constant current density of 5 A/g.

To further investigate the reason for the specific capacitance loss during the stability test, EIS was implemented under the same conditions as mentioned above (OCP, amplitude and frequency). Fig. IV. 19 shows a comparison of the EIS curves before and after stability testing. The model of equivalent circuit used to fit the impedance parameters was the same as described in inset Fig. IV. 17, and the estimated values are summarized at the bottom of Table. IV. 6. The internal resistance, charge transfer resistance, and diffusion resistance increased after 5000 successive charge-discharge cycles, which means that the electrode conductivity decreased and the interfacial charge transfer process and ion diffusion become more difficult. In addition, the double-layer capacitance has decreased, indicating a decrease in the electroactive surface area. This could explain why the electrode loses its specific capacitance after the stability test.

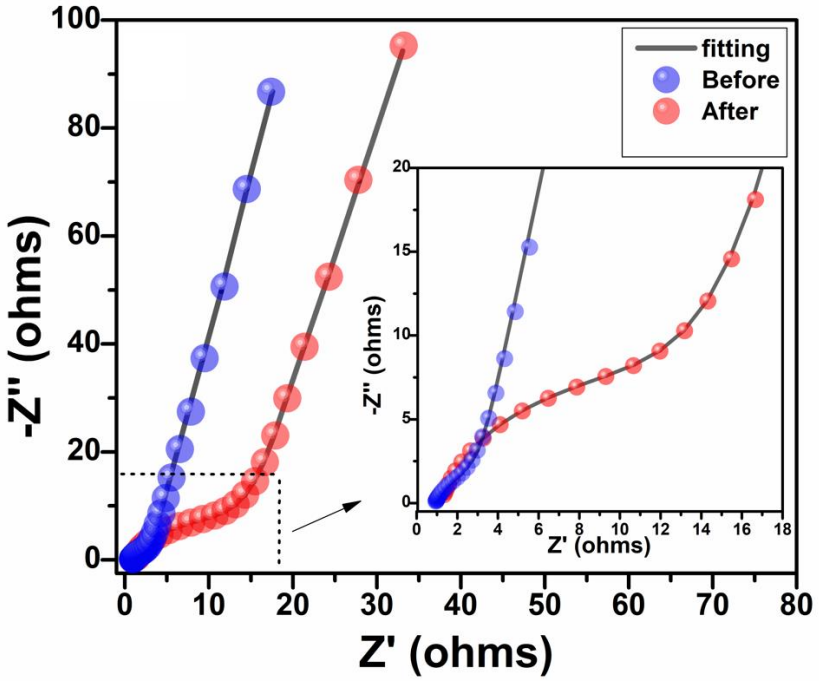

Fig. IV. 19. Comparative electrochemical impedance spectra before and after 5000 charge-discharge cycles.

IV.3.3. LCZ 05//AC Hybrid supercapacitor

Hybrid supercapacitors (HSCs) are the outcome of combining two dissimilar electrodes with different charge storage mechanisms, i.e., using one battery-type (faradaic) electrode and one capacitive (non-faradaic) electrode. This combination approach has been put forward to overcome the factor of energy density of both traditional EDLCs as well as pseudo-capacitors **[63]**. To demonstrate the viability of the LCZ 05 electrode in practical energy storage systems, a hybrid supercapacitor has been constructed using LCZ 05 (anode) and AC (cathode) in 1M KOH electrolyte solution.

To determine the potential working window and to ensure the balance of charge between the negative and positive electrodes of the hybrid device, the individual electrochemical performance of AC and LCZ 05 electrodes has been examined (three-electrode cell). As displays in Fig. IV. 20, the CV curve of the LCZ 05 electrode shows battery-type performance between −0.05 and 0.45 V, while the AC electrode reveals a typical EDLC feature within the range of −1.05 to 0.05 V, demonstrating the suitability of these two electrodes for the assembly of HSCs. Based on these assessments and the charge balance equation (**IV.4**) **[64]**, the mass loading ratio of positive and negative electrode materials was set to 1:2.

$$\frac{m^+}{m^-} = \frac{C_s^-.\Delta V^-}{C_s^+.\Delta V^+} \qquad (\mathbf{IV.4})$$

where Cs (F/g) is the specific capacitances, m (g) is the active material mass and ΔV (V) is the potential window; the (-) and (+) signs refer to negative and positive electrodes respectively.

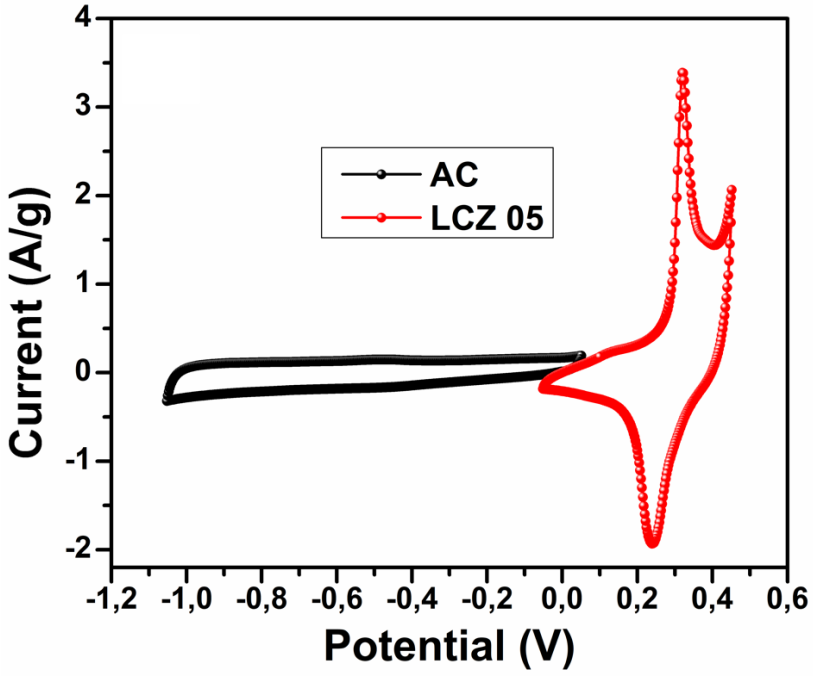

Fig. IV. 20. Individual CV curves of AC and LCZ 05 electrodes recorded at 2 $mV.s^{-1}$.

Fig. IV. 21 displays the CV graphs of the LCZ 05//AC device measured at several sweep rates within the optimal potential window. At low sweep rates, the obtained CV curves reveal a pseudo-rectangular shape, confirming the formation of fine EDLC and faradaic capacitance. This electrochemical signature is expected from hybrid devices that involve two dissimilar electrodes with different charge storage mechanisms (battery and capacitive type) **[54]**. Notably, the CV curves retained their shape as the scanning rate increased from 2 to 100 $mV.s^{-1}$, denoting the excellent rate capability of the LCZ 05//AC hybrid device.

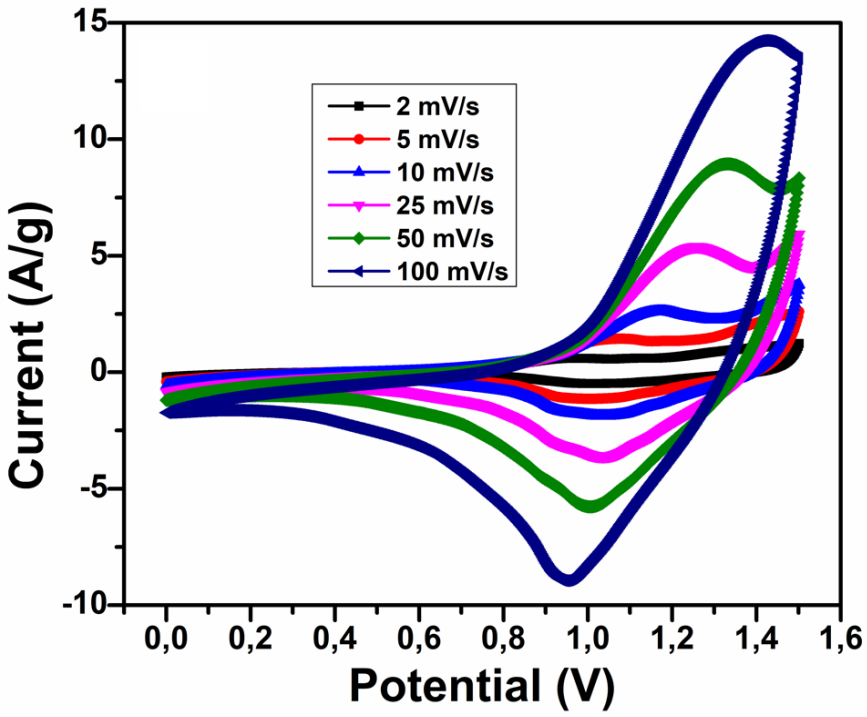

Fig. IV. 21. CV curves of LCZ 05//AC measured at various sweep rates (2-100 $mV.s^{-1}$).

The GCD measurements at several current densities are given in Fig. IV. 22, the discharging profiles can be split into two sections. The first non-linear section between 1.5 and 0.3V confirms the presence of a faradaic redox reaction, while the second section occurring from 0.3 to 0 V linearly bends towards higher discharge time values, indicating that

both redox reactions and electrochemical double-layer capacitance participate in the charge-discharge process **[44]**. Moreover, the charge-discharge curves exhibit a non-symmetrical behavior, reflecting the reduced reversibility of the device **[65]**. These results are compatible with the above cyclic voltammetry findings.

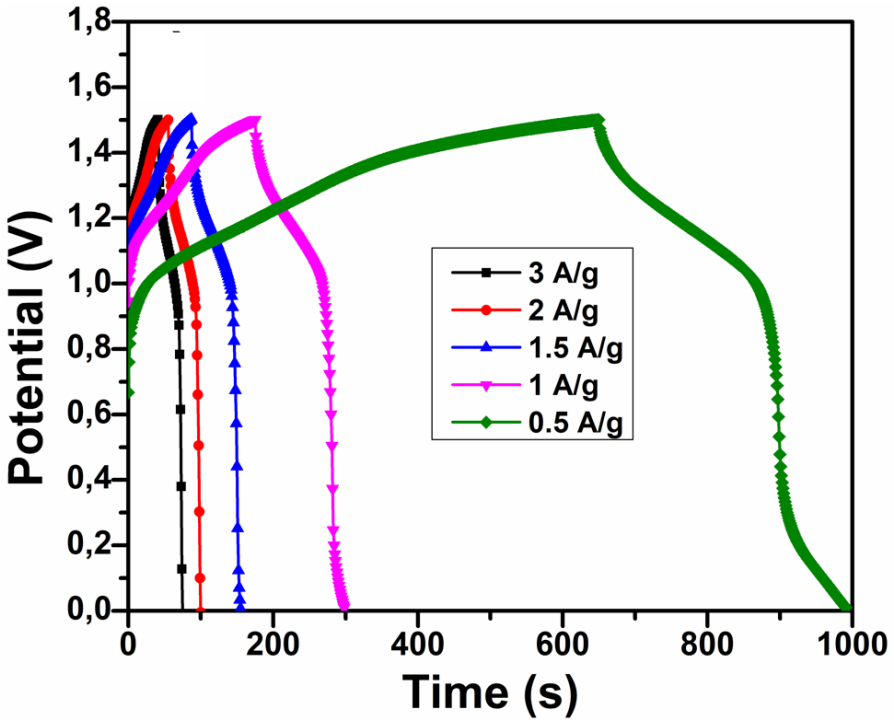

Fig. IV. 22. GCD curves measured at various current densities (0.5-3 A/g).

The calculated values of the specific capacitance from the previous GCD and CV analysis are shown in Fig. IV. 23. According to the CV findings, the LCZ 05//AC device lost ~75% of its original capacitance upon increasing the sweep rates from 2 to 100 $mV.s^{-1}$. Likewise, the hybrid device retained ~52% of its original capacitance upon increasing the density of current from 0.5 to 3 A/g. Furthermore, it is worth mentioning that the specific capacitance values obtained at 1.5 A/g are compatible with the estimated values at scan rate of 10 $mV.s^{-1}$.

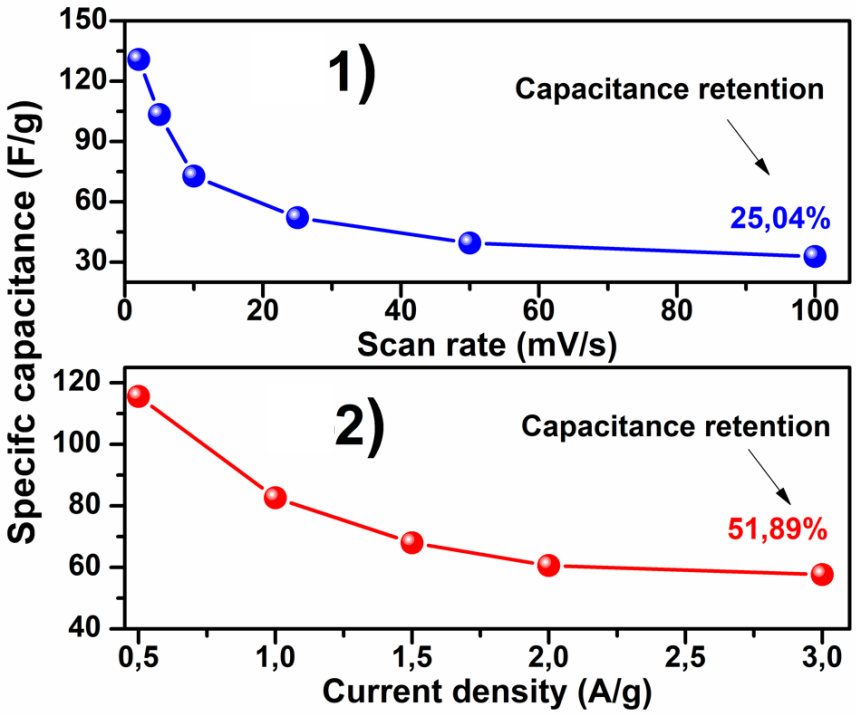

Fig. IV. 23. Capacitance versus: 1) sweep rates and 2) current densities determined from the CV and GCD curves.

The energy and power densities of LCZ 05//AC hybrid supercapacitor were determined based on the previous charge-discharge data using Eqs (**II.5**) and (**II.6**). The results are represented in the form of Ragone plot (Fig. IV. 24). The LCZ 05//AC device can provide a maximum energy density of 36.12 Wh/kg at a power density of 390.35 W/Kg, and still delivers a high energy density of 18.02 Wh/kg even at a high power density of 1900 W/Kg. These results demonstrate that the developed device is comparable and even superior to several previously reported devices [8, 9, 12, 13, 44, 66-68], as listed below in Table. IV. 7.

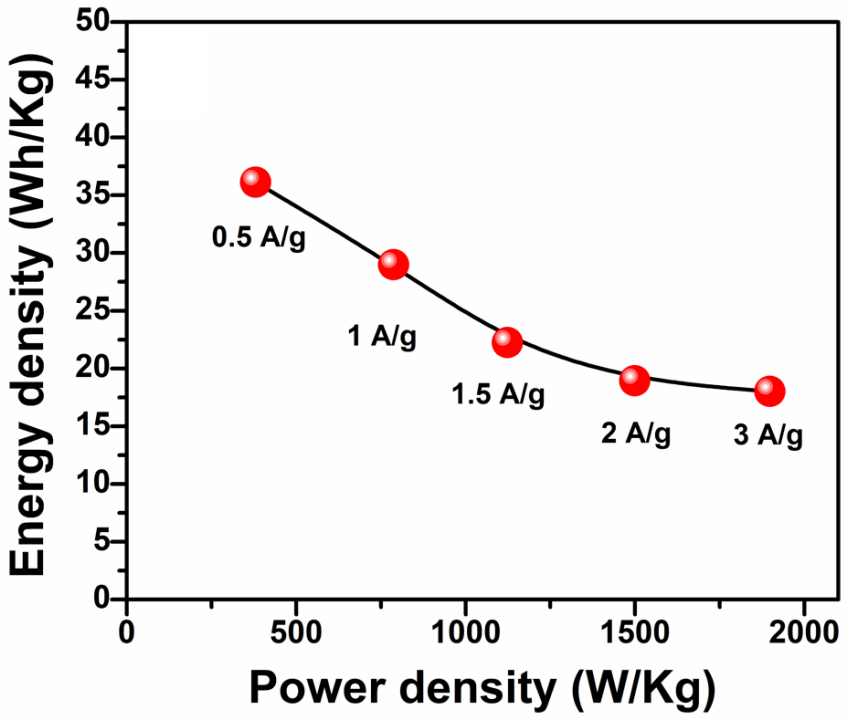

Fig. IV. 24. Ragone plot.

Table. IV. 7. Comparison of the energy and power densities of the constructed device with other supercapacitors

Supercapacitor	Electrolyte	Working Potential (V)	Energy density (Wh/kg)	Power density (W/kg)	Cyclic stability (Cycles)	Ref
$LaCoO_3$@rGO//AC	3M KOH	1	5.4	1250	76% (5000)	[44]
$LaCoO_3$@rGO//rGO	6M KOH	1.7	17.62	170	94% (10000)	[9]
$LaCoO_3$//GO	6M KOH	1.6	47.64	804.4	100% (4000)	[12]

$La_XSr_{1-X}CoO_3$//AC	1M Na_2SO_4	2	27.7	500	80% (2000)	[13]
$La_XSr_{1-X}CoO_3$// $La_XSr_{1-X}CoO_3$	1M Na_2SO_4	1.5	34.8	400	97% (2000)	[13]
$LaAlO_3$/rGO//AC	1M KOH	1.5	15	500	85% (3000)	[66]
$LaFeO_3$//$LaFeO_3$	1M Na_2SO_4	2	34	900	92% (5000)	[67]
$La_XSr_{1-X}MnO_3$//AC	1M KOH	1.2	3.9	120	47% (5000)	[68]
$La_{1-X}Ca_XMnO_3$// $La_{1-X}Ca_XMnO_3$	1M KOH	1.2	7.6	160	7.7% (2000)	[8]
$LaCo_{0.95}Zn_{0.05}O_3$// AC	1M KOH	1.5	36.12	390.35	81% (5000)	Our Work

Fig. IV. 25 depicts the Nyquist plot of LCZ05//AC hybrid supercapacitor recorded under the same conditions as mentioned above (OCP, amplitude, and frequency), where the impedance spectrum was fitted to the same equivalent circuit as described above in inset Fig. IV. 17. Compared to the individual electrode, the internal resistance value (4.82 $\Omega.cm^{-2}$) increases once the cell is assembled, thus causing the increased IR drop in the preceding GCD curves. On the other hand, the charge transfer resistance and the diffusion resistance values have been estimated to be around 7.51 and 11.61 $\Omega.cm^{-2}$, respectively. Such low resistances indicate the exceptional conductivity of the assembled device.

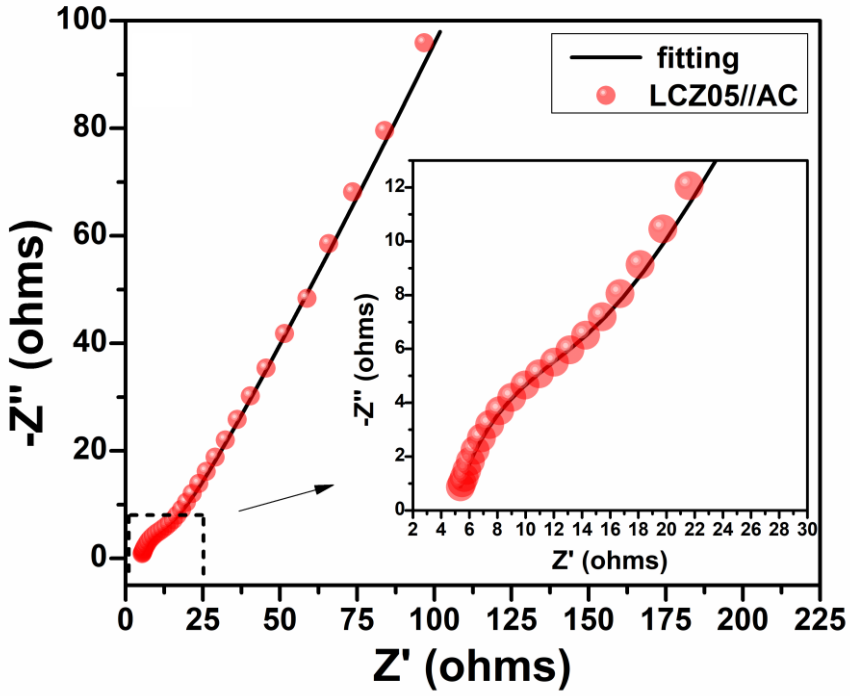

Fig. IV. 25. EIS spectrum performed at open circuit potential in the frequency range from 0.01 Hz to 100 kHz.

In order to assess the sustainability, the as-manufactured hybrid supercapacitor was subjected to 5000 successive charge and discharge cycles at 3 A/g current density with 1.5 V operating voltage. As shown in Fig. IV. 26 , it can be noticed that the value of the specific capacitance of the first 2500 cycles looks like hills, this behavior could be related to the activation and deactivation processes of the electrode materials. Thereafter, the specific capacitance starts to progressively decrease, retaining around 81% of its primary specific capacitance at the 5000th cycle, indicating a good cycle stability. In addition, the corresponding coulombic efficiency is about 68.78% revealing the poor charge-discharge reversibility, which is consistent with the GCD and CV analyses.

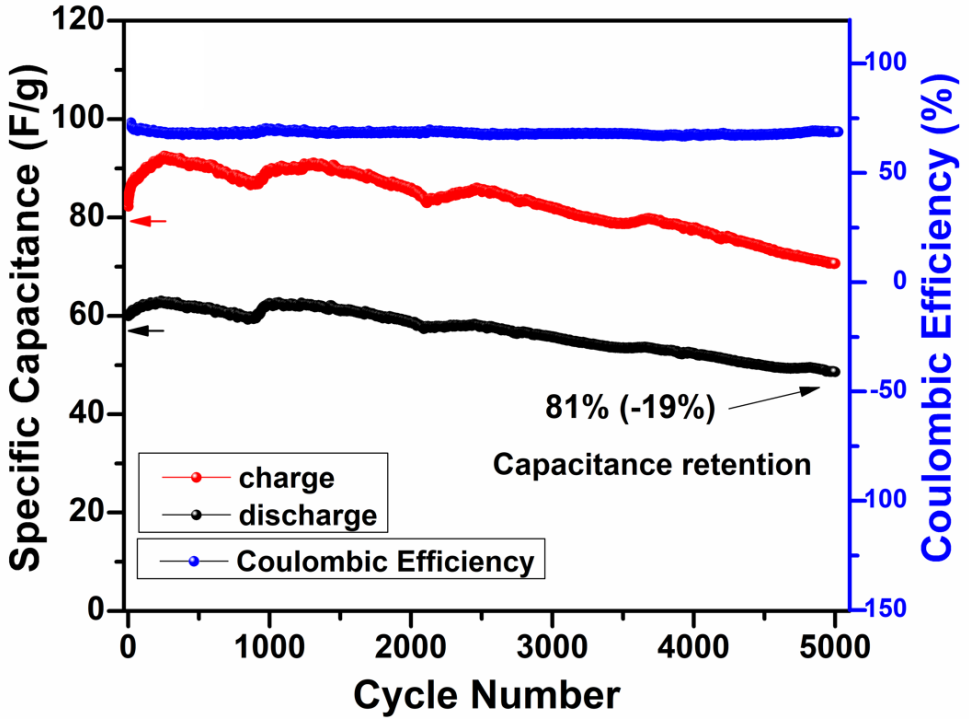

Fig. IV. 26. Stability test of the constructed device recorded at 3 A/g for 5,000 cycles.

To exemplify the practical application of the LCZ05//AC, two devices serially connected were used to illuminate a red LED as depicted in Fig. IV. 27 and Fig. IV. 28. These results demonstrate the considerable performance of the LCZ 05//AC hybrid supercapacitor and the promising prospects for energy storage applications.

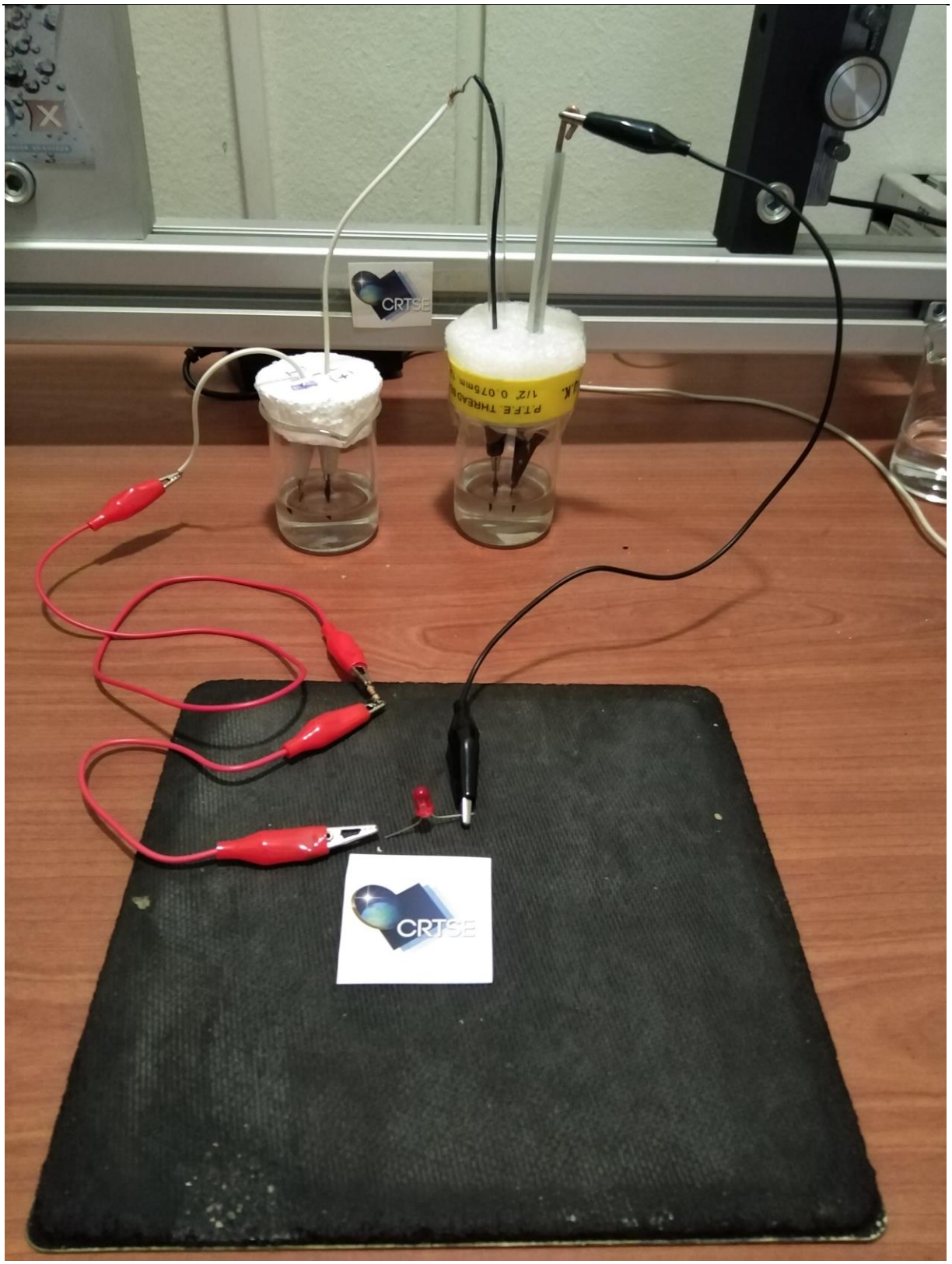

Fig. IV. 27. Photograph of a red LED connected with two cells serially connected.

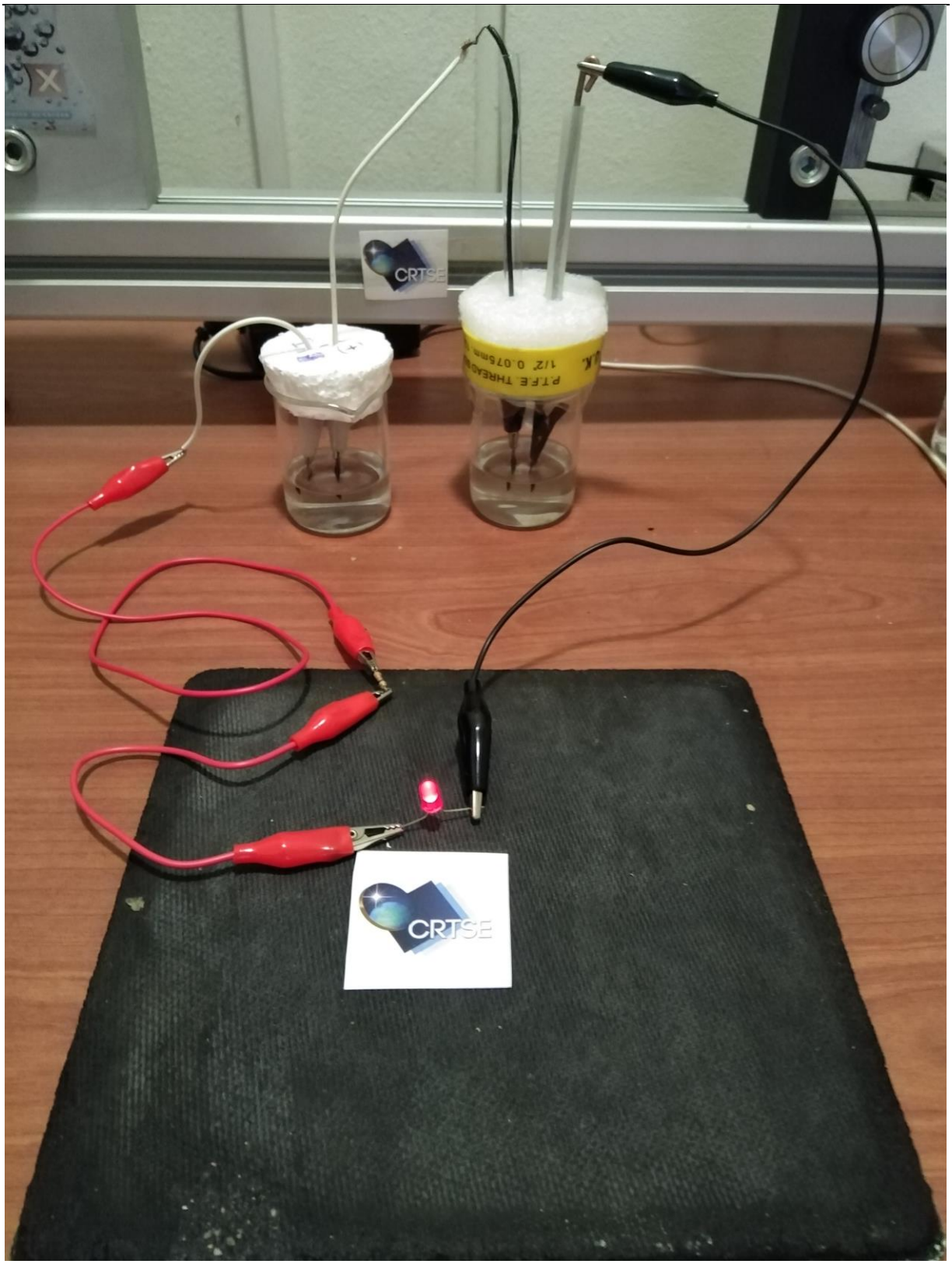

Fig. IV. 28. Photograph of a red LED eliminated with two cells serially connected.

Conclusions

In summary, zinc doped lanthanum cobaltite perovskite was successfully synthesized via the sol-gel process, using nitrate salts of zinc, lanthanum, and cobalt as cations source and citric acid as a complexing agent. XRD, FT-IR, and XPS analysis confirm the formation of highly pure perovskite without secondary phases at 1100 °C. SEM and specific surface analysis show that the surface morphology consists of polycrystalline with different shapes and sizes as well as the mesoporous structure. Electrochemical measurements exhibit that zinc doping improves the performance of $LaCoO_3$ by enhancing the conductivity, the electrochemical activity, as well as the electrode-electrolyte interface area. Among the synthesized electrode materials, the LCZ 05 electrode provides the highest specific capacitance value (300.47 F/g) which is approximately four times greater than pristine electrode LCZ 00 (75.36 F/g), and also demonstrates excellent retention of capacitance of 85.73% after 5000 cycles. Additionally, the practical performance of the LCZ 05 electrode was further investigated by assembling a hybrid supercapacitor (LCZ 05//AC). The assembled device can achieve 60 F/g at 3 A/g and retain 81% of its primary capacitance after 5000 successive cycles. Moreover, the device can supply a maximum energy density of 36.12 $Wh.kg^{-1}$ with a power density of 390.35 $W.kg^{-1}$, and still provides a high energy density of 18.02 Wh/kg even at a power density of 1900 W/Kg. The magnificent electrochemical properties of this new hybrid supercapacitor based on a novel zinc-doped lanthanum cobaltite electrode confirm the promising applicability of this novel electrode material in the next-generation supercapacitor electrodes.

References

[1] N. Lei, P. Ma, B. Yu, S. Li, J. Dai, G. Jiang, Anion-intercalated supercapacitor electrode based on perovskite-type $SrB_{0.875}Nb_{0.125}O_3$ (B= Mn, Co), Chem Eng J 421 (2021) 127790.

[2] B. Pandit, E.S. Goda, M.H.A. Elella, A. ur Rehman, S.E. Hong, S.R. Rondiya, P. Barkataki, S.F. Shaikh, A.M. Al-Enizi, S.M. El-Bahy, One-pot hydrothermal preparation of hierarchical manganese oxide nanorods for high-performance symmetric supercapacitors, Journal of Energy Chemistry 65 (2022) 116-126.

[3] H. Ren, L. Zhang, J. Zhang, T. Miao, R. Yuan, W. Chen, Z. Wang, J. Yang, B. Zhao, Na^+ pre-intercalated $Na_{0.11}MnO_2$ on three-dimensional graphene as cathode for aqueous zinc ion hybrid supercapacitor with high energy density, Carbon 198 (2022) 46-56.

[4] Y. Huang, C. Luo, Q. Zhang, H. Zhang, M.-S. Wang, Rational design of three-dimensional branched NiCo-P@CoNiMo-P core/shell nanowire heterostructures for high-performance hybrid supercapacitor, Journal of Energy Chemistry 61 (2021) 489-496.

[5] A. Mahieddine, L. Adnane-Amara, N. Gabouze, The effect of alkaline electrolytes and silver nanoparticles on the electrochemical performance of the dilithium nickel bis (tungstate) as electrode materials for high-performance asymmetric supercapacitor, Journal of Alloys and Compounds 882 (2021) 160754.

[6] J. Wu, Y. Guo, W. Raza, H. Gul, G. Luo, Y. Ding, Y. Li, Y. Lv, J. Yu, L.N.U. Rehman, Fast assembling MnO_2-network electrode materials to achieve high performance asymmetric aqueous supercapacitors, J Alloys Compd 931 (2023) 167568.

[7] S.H. Nagarajarao, A. Nandagudi, R. Viswanatha, B.M. Basavaraja, M.S. Santosh, B.M.

Praveen, A. Pandith, Recent developments in supercapacitor electrodes: A mini review, ChemEngineering 6 (2022) 5.

[8] H. Mo, H. Nan, X. Lang, S. Liu, L. Qiao, X. Hu, H. Tian, Influence of calcium doping on performance of $LaMnO_3$ supercapacitors, Ceram Int 44 (2018) 9733-9741.

[9] B. Zhang, C. Yu, Z. Li, Enhancing the Electrochemical Properties of $LaCoO_3$ by Sr-Doping, rGO-Compounding with Rational Design for Energy Storage Device, Nanoscale Research Letters 15 (2020) 1-13.

[10] Y. Cao, J. Liang, X. Li, L. Yue, Q. Liu, S. Lu, A.M. Asiri, J. Hu, Y. Luo, X. Sun, Recent advances of perovskite oxides as electrode materials for supercapacitor, Chem Commun 57 (2021) 2343-2355.

[11] M. Rafique, S. Hajra, M.Z. Iqbal, G. Nabi, S.S.A. Gillani, M. Bilal Tahir, Fabrication of novel perovskite oxide $BaxMn_{1-x}O_3$ electrode for supercapacitors, International Journal of Energy Research 45 (2021) 4145-4154.

[12] G. Guo, K. Ouyang, J. Yu, Y. Liu, S. Feng, M. Wei, Facile synthesis of $LaCoO_3$ with a high oxygen vacancy concentration by the plasma etching technique for high-performance oxygen ion intercalation pseudocapacitors, ACS Applied Energy Materials 3 (2019) 300-308.

[13] Y. Cao, B. Lin, Y. Sun, H. Yang, X. Zhang, Symmetric/Asymmetric Supercapacitor Based on the Perovskite-type Lanthanum Cobaltate Nanofibers with Sr-substitution, Electrochim Acta 178 (2015) 398-406.

[14] R. Mondal, N.K. Mishra, M. Singh, A. Gupta, P. Singh, Perovskite $La_{1-x}K_xCoO_{3-\delta}$ ($0 \leqslant x \leqslant 0.5$): a novel bifunctional OER/ORR electrocatalyst and supercapacitive charge storage

electrode in a neutral Na_2SO_4 electrolyte, PCCP 24 (2022) 28584-28598.

[15] B. Zhang, P. Liu, Z. Li, X. Song, Synthesis of two-dimensional Sr-doped $LaNiO_3$ nanosheets with improved electrochemical performance for energy storage, Nanomaterials 11 (2021) 155.

[16] H.S. Tripathi, A. Dutta, T. Sinha, Tailoring structural and electrochemical properties in Sr2+ incorporated nanostructured $BiFeO_3$ for enhanced asymmetric solidstate supercapacitor, Electrochim Acta 421 (2022) 140505.

[17] E. Abdel-Khalek, E. Mohamed, D. Rayan, S.G. Mohamed, The enhancement of supercapacitors performances of $LaMnO_{3\pm\delta}$ perovskite by Ag-doping, Physica B: Condensed Matter 615 (2021) 413065.

[18] A.N. Singh, K.G. Nigam, R. Mondal, V. Kushwaha, A. Gupta, C. Rath, P. Singh, Effect of strontium doping on the electrochemical pseudocapacitance of $Y_{1-x}Sr_xMnO_{3-\delta}$ perovskites, PCCP 25 (2023) 326-340.

[19] M.S. Waheed, K. Jabbour, S. Houda, F.M.A. Alzahrani, K.M. Katubi, S. Riaz, M.N. Ashiq, S. Manzoor, S. Aman, M. Al-Buriahi, Fabrication of mesoporous Er doped $ZnMnO_3$ nanoflake via sol gel approach for energy storage application, Ceram Int (2022).

[20] Y. Cao, H. He, S. Li, P. Ruan, J. Yi, W. Qiu, The Preparation and Modification of Strontium Titanate Ceramic Films for High - Performance Flexible Supercapacitor, ChemElectroChem (2023) e202200947.

[21] M. Guo, Y. Liu, F. Zhang, F. Cheng, C. Cheng, Y. Miao, F. Gao, J. Yu, Inactive Al^{3+}-doped La $(CoCrFeMnNiAlx)_{1/(5+x)}O_3$ high-entropy perovskite oxides as high

performance supercapacitor electrodes, J. Adv. Ceram. 11 (2022) 742-753.

[22] R. Andoulsi-Fezei, K. Horchani-Naifer, M. Ferid, Influence of zinc incorporation on the structure and conductivity of lanthanum ferrite, Ceram Int 42 (2016) 1373-1378.

[23] X. Qian, Y. Yin, Y. Lu, J. Xia, B. Huang, J. Sun, G. He, H. Chen, Construction of sulfur vacancies enriched hollow zinc cobalt bimetallic sulfides for high-performance supercapacitors, J Alloys Compd 913 (2022) 165191.

[24] S.J. Uke, S.P. Mardikar, D.R. Bambole, Y. Kumar, G.N. Chaudhari, Sol-gel citrate synthesized Zn doped $MgFe_2O_4$ nanocrystals: a promising supercapacitor electrode material, Materials Science for Energy Technologies 3 (2020) 446-455.

[25] J. Wu, W. Raza, P. Wang, A. Hussain, Y. Ding, J. Yu, Y. Wu, J. Zhao, Zn-doped MnO_2 ultrathin nanosheets with rich defects for high performance aqueous supercapacitors, Electrochim Acta 418 (2022) 140339.

[26] F. Yuan, G. Gao, X. Jiang, W. Bi, Y. Su, J. Guo, Z. Bao, J. Shen, G. Wu, Suppressing the metal-metal interaction by $CoZn_{0.5}V_{1.5}O_4$ derived from two-dimensional metal-organic frameworks for supercapacitors, Sci. China Mater. 65 (2022) 105-114.

[27] Y. Qiao, G. Liu, R. Xu, R. Hu, L. Liu, G. Jiang, M. Demir, P. Ma, $SrFe_{1-x}ZrxO_{3-\delta}$ perovskite oxides as negative electrodes for supercapacitors, Electrochim Acta 437 (2023) 141527.

[28] K. Xiang, D. Wu, Y. Fan, W. You, D. Zhang, J.-L. Luo, X.-Z. Fu, Enhancing bifunctional electrodes of oxygen vacancy abundant $ZnCo_2O_4$ nanosheets for supercapacitor and oxygen evolution, Chem Eng J 425 (2021) 130583.

[29] K. Zheng, L. Liao, Y. Zhang, H. Tan, J. Liu, C. Li, D. Jia, Hierarchical NiCo-LDH core/shell homostructural electrodes with MOF-derived shell for electrochemical energy storage, J Colloid Interface Sci 619 (2022) 75-83.

[30] Y. Li, H. Wang, T. Shu, J. Yuan, G. Lu, B. Lin, Z. Gao, F. Wei, C. Ma, J. Qi, Two-dimensional hierarchical MoS2 lamella inserted in CoS_2 flake as an advanced supercapacitor electrode, J. Energy Storage. 51 (2022) 104299.

[31] C.-S. Liu, C.-L. Huang, H.-C. Fang, K.-Y. Hung, C.-A. Su, Y.-Y. Li, MnO_2-based carbon nanofiber cable for supercapacitor applications, J. Energy Storage. 33 (2021) 102130.

[32] M. Sandhiya, M.P. Nadira, M. Sathish, Fabrication of flexible supercapacitor using N-doped porous activated carbon derived from poultry waste, Energy Fuels 35 (2021) 15094-15100.

[33] J. Shao, G. Zeng, Y. Li, Effect of Zn substitution to a $LaNiO_{3-\delta}$ perovskite structured catalyst in ethanol steam reforming, Int J Hydrogen Energy 42 (2017) 17362-17375.

[34] I. Chadli, M. Omari, M. Abu Dalo, B.A. Albiss, Preparation by sol–gel method and characterization of Zn-doped $LaCrO_3$ perovskite, J Sol-Gel Sci Technol 80 (2016) 598-605.

[35] R. Andoulsi, K. Horchani-Naifer, M. Férid, Effect of the preparation route on the structure and microstructure of $LaCoO_3$, Chemical Papers 68 (2014) 608-613.

[36] M. Surendar, T. Sagar, G. Raveendra, M.A. Kumar, N. Lingaiah, K.R. Rao, P.S. Prasad, Pt doped $LaCoO_3$ perovskite: A precursor for a highly efficient catalyst for hydrogen production from glycerol, Int J Hydrogen Energy 41 (2016) 2285-2297.

[37] I. Safo, M. Werheid, C. Dosche, M. Oezaslan, The role of polyvinylpyrrolidone (PVP) as

a capping and structure-directing agent in the formation of Pt nanocubes, Nanoscale Advances 1 (2019) 3095-3106.

[38] A.K. Tomar, G. Singh, R.K. Sharma, Fabrication of a Mo‐doped strontium cobaltite perovskite hybrid supercapacitor cell with high energy density and excellent cycling life, ChemSusChem 11 (2018) 4123-4130.

[39] W. Liu, J. Xu, R. Lv, Y. Wang, H. Xu, J. Yang, Effects of sintering behavior on piezoelectric properties of porous PZT ceramics, Ceram Int 40 (2014) 2005-2010.

[40] F. Li, J.-F. Li, Effect of Ni substitution on electrical and thermoelectric properties of $LaCoO_3$ ceramics, Ceram Int 37 (2011) 105-110.

[41] F. Zheng, J. Wang, W. Liu, J. Zhou, H. Li, Y. Yu, P. Hu, W. Yan, Y. Liu, R. Li, Novel diverse-structured h-WO_3 nanoflake arrays as electrode materials for high performance supercapacitors, Electrochim Acta 334 (2020) 135641.

[42] K.S. Sing, Reporting physisorption data for gas/solid systems with special reference to the determination of surface area and porosity (Recommendations 1984), Pure and Applied Chemistry 57 (1985) 603-619.

[43] G.M. Tomboc, H.S. Jadhav, H. Kim, PVP assisted morphology-controlled synthesis of hierarchical mesoporous $ZnCo_2O_4$ nanoparticles for high-performance pseudocapacitor, Chem Eng J 308 (2017) 202-213.

[44] A.K. Vats, A. Kumar, P. Rajput, A. Kumar, Engineered perovskite $LaCoO_3$/rGO nanocomposites for asymmetrical electrochemical supercapacitor application, Journal of Materials Science: Materials in Electronics 33 (2022) 2590–2606.

[45] X. Chen, Q. Su, J. Yu, M. Wei, G. Guo, Y. Wang, Experimental study on the degradation mechanism of $LaCoO_3$-based symmetric supercapacitors, RSC Advances 11 (2021) 25170-25178.

[46] J.T. Mefford, W.G. Hardin, S. Dai, K.P. Johnston, K.J. Stevenson, Anion charge storage through oxygen intercalation in $LaMnO_3$ perovskite pseudocapacitor electrodes, Nature materials 13 (2014) 726-732.

[47] X. Wang, J. Hao, Y. Su, F. Liu, J. An, J. Lian, A $Ni_{1-x}Zn_xS$/Ni foam composite electrode with multi-layers: one-step synthesis and high supercapacitor performance, J. Mater. Chem. A 4 (2016) 12929-12939.

[48] C. Yuan, J. Li, L. Hou, X. Zhang, L. Shen, X.W. Lou, Ultrathin mesoporous $NiCo_2O_4$ nanosheets supported on Ni foam as advanced electrodes for supercapacitors, Adv Funct Mater 22 (2012) 4592-4597.

[49] W. Xu, Z. Jiang, Q. Yang, W. Huo, M.S. Javed, Y. Li, L. Huang, X. Gu, C. Hu, Approaching the lithium-manganese oxides' energy storage limit with Li_2MnO_3 nanorods for high-performance supercapacitor, Nano Energy 43 (2018) 168-176.

[50] X. Wang, H. Mei, P. Chang, M. Zhang, T. Hu, L. Cheng, L. Zhang, Layered $(NH_4)_2V_{10}O_{25}\cdot 8H_2O$ Coupled with Two-Electron Iodide Redox Achieving Exponential Energy Density Enhancement of NH^{4+} Supercapacitors, Applied Surface Science 605 (2022) 154688.

[51] S. Nagamuthu, S. Vijayakumar, K.-S. Ryu, Cerium oxide mixed $LaMnO_3$ nanoparticles as the negative electrode for aqueous asymmetric supercapacitor devices, Materials Chemistry and Physics 199 (2017) 543-551.

[52] A. Mahieddine, L. Adnane-Amara, N. Gabouze, A. Addad, A. Swaidan, R. Boukherroub, Self-combustion synthesis of dilithium cobalt bis (tungstate) decorated with silver nanoparticles for high performance hybrid supercapacitors, Chem Eng J 426 (2021) 131252.

[53] Z. Zhang, H. Huo, Z. Yu, L. Xiang, B. Xie, C. Du, J. Wang, G. Yin, Unraveling the reaction mechanism of low dose Mn dopant in $Ni(OH)_2$ supercapacitor electrode, Journal of Energy Chemistry 61 (2021) 497-506.

[54] P.M. Shafi, D. Mohapatra, V.P. Reddy, G. Dhakal, D.R. Kumar, D. Tuma, T. Brousse, J.-J. Shim, Sr-and Fe-substituted $LaMnO_3$ Perovskite: Fundamental insight and possible use in asymmetric hybrid supercapacitor, Energy Storage Materials 45 (2022) 119-129.

[55] X. Song, X. Ma, Y. Li, L. Ding, R. Jiang, Tea waste derived microporous active carbon with enhanced double-layer supercapacitor behaviors, Appl Surf Sci 487 (2019) 189-197.

[56] P.M. Shafi, A.C. Bose, A. Vinu, Electrochemical Material Processing via Continuous Charge‐Discharge Cycling: Enhanced Performance upon Cycling for Porous $LaMnO_3$ Perovskite Supercapacitor Electrodes, ChemElectroChem 5 (2018) 3723-3730.

[57] Z.A. Elsiddig, H. Xu, D. Wang, W. Zhang, X. Guo, Y. Zhang, Z. Sun, J. Chen, Modulating Mn^{4+} ions and oxygen vacancies in nonstoichiometric $LaMnO_3$ perovskite by a facile sol-gel method as high-performance supercapacitor electrodes, Electrochim Acta 253 (2017) 422-429.

[58] Y. Jing, W. Li, D. Wang, X. Chang, M. He, Z. Ren, B-site regulated bimetallic perovskite fluoride $NaCo_{1-x}Ni_xF_3$/reduced graphene oxide as the enhanced performance electrode material for supercapacitors, J Alloys Compd 905 (2022) 164188.

[59] A.L. Soares, M.L. Zamora, L.F. Marchesi, M. Vidotti, Adsorption of catechol onto PEDOT films doped with gold nanoparticles: Electrochemical and spectroscopic studies, Electrochim Acta 322 (2019) 134773.

[60] Z. Li, W. Zhang, H. Wang, B. Yang, Two-dimensional perovskite $LaNiO_3$ nanosheets with hierarchical porous structure for high-rate capacitive energy storage, Electrochim Acta 258 (2017) 561-570.

[61] P.P. Ma, Q.L. Lu, N. Lei, Y.K. Liu, B. Yu, J.M. Dai, S.H. Li, G.H. Jiang, Effect of A-site substitution by Ca or Sr on the structure and electrochemical performance of $LaMnO_3$ perovskite, Electrochim Acta 332 (2020) 135489.

[62] H. Chen, G. Jiang, W. Yu, D. Liu, Y. Liu, L. Li, Q. Huang, Z. Tong, Electrospun carbon nanofibers coated with urchin-like $ZnCo_2O_4$ nanosheets as a flexible electrode material, J. Mater. Chem. A 4 (2016) 5958-5964.

[63] N.R. Chodankar, H.D. Pham, A.K. Nanjundan, J.F. Fernando, K. Jayaramulu, D. Golberg, Y.K. Han, D.P. Dubal, True meaning of pseudocapacitors and their performance metrics: asymmetric versus hybrid supercapacitors, Small 16 (2020) 2002806.

[64] D.M. Sayed, M.M. Taha, L.G. Ghanem, M.S. El-Deab, N.K. Allam, Hybrid supercapacitors: A simple electrochemical approach to determine optimum potential window and charge balance, J Power Sources 480 (2020) 229152.

[65] Y. Zhao, X. He, R. Chen, Q. Liu, J. Liu, D. Song, H. Zhang, H. Dong, R. Li, M. Zhang, Hierarchical $NiCo_2S_4$@$CoMoO_4$ core-shell heterostructures nanowire arrays as advanced electrodes for flexible all-solid-state asymmetric supercapacitors, Appl Surf Sci 453 (2018)

73-82.

[66] T.V. Raj, P.A. Hoskeri, H. Muralidhara, C. Manjunatha, K.Y. Kumar, M. Raghu, Facile synthesis of perovskite lanthanum aluminate and its green reduced graphene oxide composite for high performance supercapacitors, J Electroanal Chem 858 (2020) 113830.

[67] Y. Zhang, J. Ding, W. Xu, M. Wang, R. Shao, Y. Sun, B. Lin, Mesoporous $LaFeO_3$ perovskite derived from MOF gel for all-solid-state symmetric supercapacitors, Chem Eng J 386 (2020) 124030.

[68] X. Lang, H. Mo, X. Hu, H. Tian, Supercapacitor performance of perovskite $La_{1-x}Sr_xMnO_3$, Dalton transactions 46 (2017) 13720-13730.

General Conclusion and Perspectives

1. General Conclusion

Our thesis, which consists of two parts, has enabled us to develop new efficient electrode materials for energy storage and conversion.

In the first part of the work, a series of $LaCo_{1-x}Zn_xO_3$ perovskites with high concentrations of zinc dopant (x = 0, 01, 01, 03 and 0.4) were successfully synthesized via the facile sol-gel route and investigated for their structural, morphological and electrochemical properties for possible use as electrocatalysts for the oxygen evolution reaction. Thus, the main conclusions drawn are as follows:

The structural analysis confirms that the solubility limit of zinc in $LaCoO_3$ is reached up to $x \leq 0.3$. Furthermore, the introduction of zinc at high contents provokes swelling of the unit cell volume, the generation of oxygen deficiencies, allows the growth of the grain size and augments the pore volume as well as the specific surface. The electrocatalytic investigations demonstrate that Zn-doping with an appropriate amount (x = 0.1) boosts the electrocatalytic performance of $LaCoO_3$ toward the OER by reducing; the overpotential, Tafel slop, resistance of charge-transfer, and enhancing the electronic conductivity compared to the pristine electrocatalyst.

In the second part of the work, a series of $LaCo_{1-x}Zn_xO_3$ perovskite-type oxides with low concentrations of zinc dopant (x = 0, 0,3, 0,5 and 0.1) were elaborated via the same process and investigated for their structure, morphology, porosity, as well as the electrochemical performances for potential use as a material for hybrid supercapacitor electrodes. Therefore, the main conclusions drawn are as follows:

The XRD and XPS analysis demonstrate that the incorporation of zinc leads to a swelling of the unit cell volume and the generation of oxygen vacancies. SEM analysis reveals that the surface consists of distinct polycrystalline particles with well-defined boundaries of different shapes and sizes and also demonstrates the substitution of cobalt with low amounts of zinc is effective in repressing grain growth. Furthermore, N_2 physisorption analysis shows the mesoporous structure and that the specific surface area increases slightly with increasing incorporated zinc amount. The electrochemical measurements exhibit that zinc doping improves the performance of $LaCoO_3$ by enhancing the specific capacitance, the conductivity and the electrochemical activity (reducing the charge transfer resistance), as well as the electrode-electrolyte interface area.

2. Perspectives and future work

In this thesis, we set out to synthesize electrode materials for supercapacitors and oxygen evolution reaction. However, many issues need to be addressed from material synthesis to prototype construction.

Several suggestions for future research are offered:

- Understanding the reaction mechanisms of the developed materials is not sufficient. They can be further studied by applying some in situ techniques, such as XRD and SEM. More interesting information about the changes in the materials during the electrochemical process would be obtained, which could be useful to improve their performance.
- Based on the current results, it can be seen that the stability of the materials is not too perfect. Further efforts must be made to improve their stability, for example by increasing

the conductivity by making hybrid materials with graphene and CNT, and by redesigning the electrode structures.

- The electrolysis of water in this work was carried out in fresh water. So we look forward to the future use of sea water or waste water.
- The supercapacitor in this work was constructed in a beaker and the cell structure is also a very preponderant factor influencing the performance of the supercapacitor. More sophisticated designs, such as coin cells and cylindrical cells, can be applied.
- In addition to experimental exploration, computational simulation at the molecular level can be a powerful tool to better understand the properties of a material, which could be useful for designing high-performance electrodes and solving current problems.